CHAPTER 4

Synthesis of New Square planar Cu(II) complexes derived from acylpyrazolone ligand: Molecular structure Computational, Hirshfeld analysis and antiproliferative properties

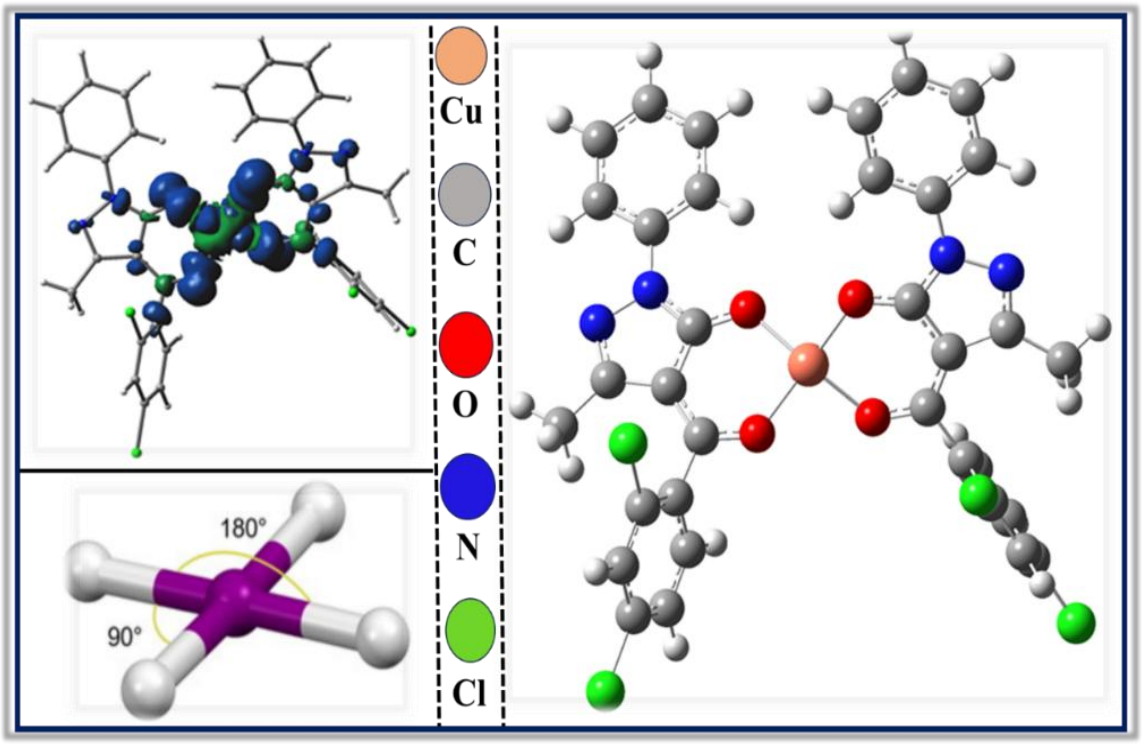

Chapter 4: Part (a)

Cytotoxicity assay and gene expression studies of acylpyrazolone-based square planar Cu(II) complexes: synthesis, characterization and computations

4a.1 Introduction

Iron, copper and zinc are the most common metals in a biological system among all the transition metals. Copper has a significant role in biological systems as an important trace metal [1]. Transition metals have many distinctive qualities such as different coordination modes and oxidation states. Their interactions with negatively charged molecules and reactivity towards organic substrates increase their importance. Due to their special characteristics, transition metals encouraged the emergence of metal-based drugs with potential pharmacological applications. Several clinical conditions, including cancer, are associated with abnormal metal ion concentrations [2]. Copper is a vital micronutrient that is also an important cofactor for various metalloenzymes involved in mitochondrial metabolism (cytochrome c oxidase) or cellular radical detoxification against reactive oxygen species (ROS) (superoxide dismutase). Increased copper promotes metastasis and tumour development. It is found in several brain, breast, colon, lung and liver cancers and acts as a prognostic marker for the illness [3]. Neuroblastoma (NB), a unique form of cancer and one of the most common solid tumours in early infancy, accounts for around 8% of paediatric malignancies. Although the genetic and epigenetic underpinnings of this prevalence are unknown, NB is more common in boys than in girls. NB is often a more sluggish but deadly illness [4]. Chemotherapy is the most effective cure for a variety of cancers. Chemotherapy is characterized by its limited efficacy, significant side effects, and multidrug resistance. Therefore, it is necessary to create new active substances that would diminish the side effects of chemotherapy.

These days, coordination chemistry is in high demand because of its variety of bioactive qualities. Consequently, it is feasible to produce complex molecules that exhibit the necessary features [5]. Numerous molecules with great potential for breakthroughs in medicinal chemistry, coordination chemistry, and functional materials are produced using the well-known synthon pyrazolone.

At the end of the **19th** century, an acylpyrazolone was first synthesized. As effective metal extractants or chelating agents, acylpyrazolone ligands have also been used in the spectroscopic analysis of metals in traces [6]. The synthesis of chelating ligands that may be adjusted to produce an effective coordination to a particular metal ion is made possible by substituting one hydrogen on the C_4 carbon atom with an acyl moiety. There are pyrazolone scaffolds in a variety of bioactive natural alkaloids and pharmaceuticals that have antipyretic analgesic, neuroprotective, anticancer, antioxidant, antibacterial, and anti-infective effects, as well as inhibitors of several biological enzymes [7].

Ligand selection during synthesis and designing drug molecules has always become an important tool. In pharmaceutics and biology, pyrazolones are a common class of heterocyclic chemicals. 4-Acyl pyrazolones are heterocyclic β-diketones that can form mono- and multinuclear complexes [8]. By 1959, Jensen had developed a useful technique to synthesise 1-phenyl-3-methyl-4-acylpyrazol-5-ones. Largely used in analytical chemistry for the determination and isolation of almost all metal ions due to the high ability of acylpyrazolonates to extract, lower pKa values than those of conventional -dicarbonyl compounds, great separation power, intense colour of the complex extracts and low solubility of the complexes in some solvents [9].

We selected the biocompatible metal ion Cu from the group of metal ions because of its significance in biological living systems. Cancer chemotherapeutics used alone or in conjunction with other medications include organometallics like copper compounds [3]. Using gene expression profiles of the complexes, Jadeja and coworkers examined the ability of the copper(II) complexes derived from 4-acyl pyrazolones to induce apoptosis in human lung cancer cells in vitro. They discovered a modest downregulation of the targeted genes [10]. Density functional theory (DFT), in addition to experimental characterization is a unique and innovative method for gaining a deeper understanding of the various chemical characteristics that arise in metal-ligand complexes [11]. This study aims to look into the spectroscopic, ESR, redox behaviour, X-ray single crystal and some characteristics of the square planar Cu^{+2} complex. Cell death analysis of synthesized complexes was performed, *in vitro* anti-cancer activity was done using hepatocellular carcinoma cell line (HepG2), lung carcinoma cell line (NCI-H23) and neuroblastoma cell line (SH-SY5Y) and comparison against cis-platin. A gene expression study on SH-SY5Y neuroblastoma cells.

4a.2 Experimental work

4a.2.1 Materials and Methods

All copper salts, AR-grade solvents, acyl chloride and pyrazolone material were obtained from the same sources described in Chapters **2** and **3**. Lung adenocarcinoma (NCI-H23), hepatocellular carcinoma (HepG2) and neuroblastoma (SH-SY5Y) cancer cell lines were procured from the National Centre for Cell Science (NCCS), Pune. MTT and FBS were purchased from Himedia, India and Gibco, USA. The cytotoxicity kit was obtained from Invitrogen, USA. Cisplatin was acquired from Sigma-Aldrich. High-Capacity cDNA Reverse Transcription Kit for gene expression study, all the dyes (SYBR green, Calcein dye and Ethidium homodimer dye EthD-1) were purchased from Thermo Fisher Scientific (Applied Biosystems). These materials were vital to the successful execution of the

experiments and were obtained in strict alignment with the established procurement protocols. All the chemicals used in this study were purified using standard methods [12]**.** The synthesis and characterization of the ligands HL^{I} and HL^{V} were carried out according to the procedures described in Chapter **2.** The HL^{V} ligand was synthesized, characterized and documented in a previous publication from our laboratory [13].

4a.2.2 Synthetic route of complex-5 and complex-6

The Cu(II) complexes were synthesized following the same procedure outlined in Chapter **3**. Hot methanolic solution of HL^{I} ligand (0.0694g, 0.002 mol) and HL^{V} ligand (0.0694g, 0.002 mol) were taken in two different round bottom flasks (RBF) attached to the water condenser. After getting clear solutions in both the RBFs, the $CuSO_4.5H_2O$ (copper sulphate pentahydrate) metal salt (0.249g, 0.001mol) dissolved in CH_3OH (10ml) solvent, was added dropwise to the hot methanolic solution of respective ligands. The resultant mixture was refluxed for 3-4 hours at a temperature of 70-80°C. The products were then filtered, washed with methanol, and dried. Green and yellowish-green precipitates of the Cu(II) complexes were obtained. A small portion of both products was taken for crystallization. After dissolving in hot DMF, the solid products were left to crystallize at room temperature. X-ray-quality dark green single crystals of both synthesized copper(II) complexes were produced in a short period.

Complex-5: Green colour, yield: 85%, M.P:> 200°C, Molecular formula: $C_{34}H_{22}Cl_4CuN_4O_4$, M.W: 755.921, Elemental analysis: C (Exp. 53.92%, Calc. 54.02%); H (Exp. 2.90%, Calc. 2.93%); N (Exp. 6.96%, Calc. 7.41%); Cu (Exp. 8.10%, Calc. 8.08%), **FTIR (KBr, cm^{-1}):** ν(C=O) of pyrazolone: (1602), ν(C=O) of 2,4-dichloro benzoyl chloride: (1577), cyclic ν(C=N): (1435).

Complex-6: Greenish yellow colour, yield: 86%, M.P:> 200°C, Molecular formula: $C_{34}H_{22}Cl_4CuN_4O_4$, M.W: 755.89, gravimetrically and volumetrically, Elemental analysis: C (Exp. 49.20%, Calc. 49.49%); H (Exp. 3.03%, Calc. 3.03%); N (Exp. 7.50%, Calc. 7.80%); Cu (Exp. 8.07%, Calc. 8.05%), (Metal estimation- gravimetrically and volumetrically), ν(C=O) of pyrazolone: (1601), ν(C=O) of 4-chloro benzoyl chloride: (1586), cyclic ν(C=N): (1475).

The Mass spectrum of complex-**5** is shown in **Fig.4a.1.** The synthetic route of complexes-**5** and complex-**6** are demonstrated in **Fig.4a.2**. The physical appearance of complex-**5** and complex-**6** is pictured in **Fig.4a.3.**

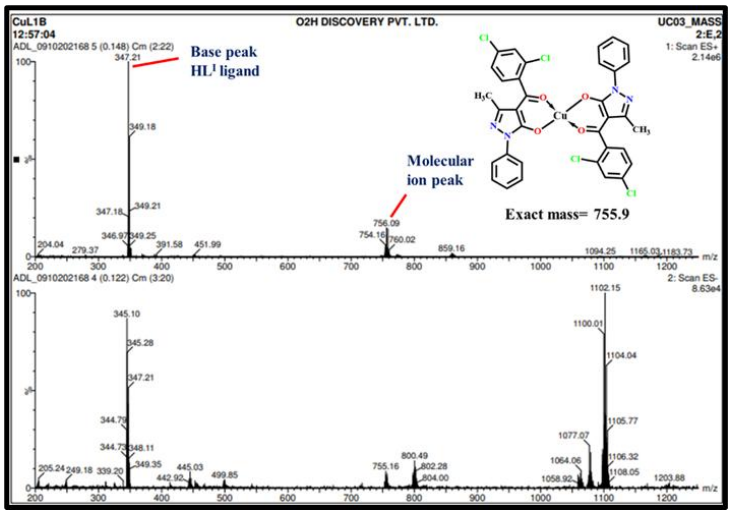

Fig.4a.1. Mass spectrum of complex-5

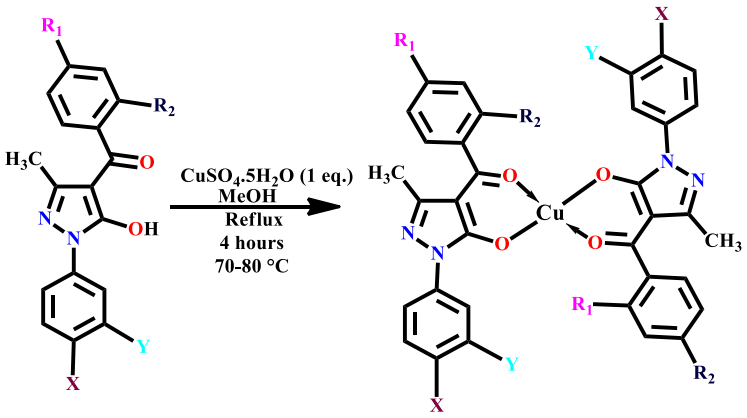

Complex-5: R_1= Cl, R_2= Cl, X= H, Y= H

Complex-6: R_1= Cl, R_2= H, X = H, Y= Cl

Fig.4a.2. Synthetic route of complex-5 and complex-6

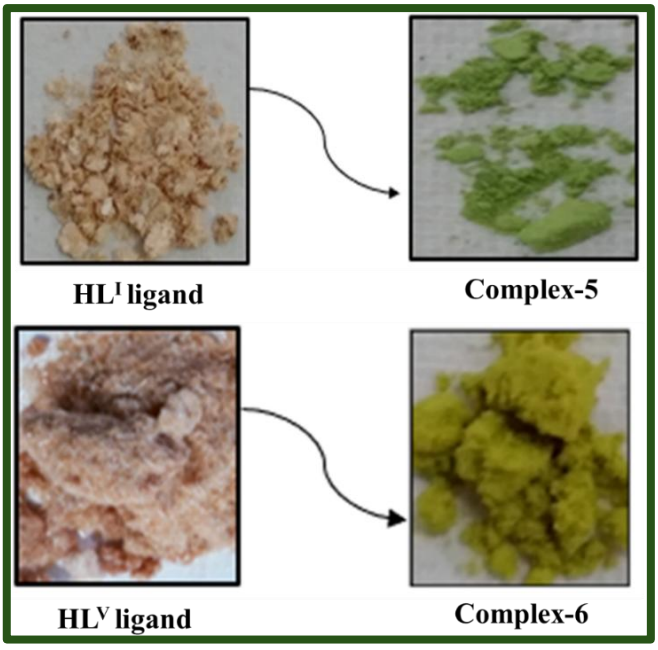

Fig.4a.3. Physical appearance of respective ligands complex-5 and complex-6

4a.2.3 X-ray crystallographic study

Both Cu(II) complexes were recrystallized from hot DMF solvent, resulting in bluish-green, plate-like single crystals of complex-**5** and complex-**6.** The X-ray crystal structures of both copper complexes were determined using graphite monochromatized Mo—Kα radiation (λ = 0.71073 Å). Data were collected using a Bruker APEX-II CCD diffractometer at 100(2) K. The structures were solved with SHELXT software and refined using the SHELXL-2018/3 program [14][15].

4a.2.4 Physical measurements and Characterization

The two synthesized copper complexes were examined using various spectroscopic and analytical techniques, including FTIR, mass spectrometry, UV-Vis, TG-DTA, cyclic voltammetry (CV), and electron spin resonance (ESR). The infrared spectra (4000–400 cm^{-1}, KBr discs) of the complexes were recorded using a Bruker Alpha instrument. The mass spectra were obtained using an XEVO G2-XS QTOF at IIT Ropar. The electronic spectra of both copper complexes were recorded in DMSO solvent over the 250–900 nm range using a V-730 UV-visible spectrophotometer. The magnetic properties of the complexes were examined using ESR analysis in the powder state at room temperature (RT) and in solution at liquid nitrogen temperature (LNT), with tetracyanoethylene (TCNE) as a marker (g = 2.00277), at SAIF IIT Mumbai. Cyclic voltammetry (CV) measurements were carried out using a CHI608E model at CSIR-CSMCRI, Bhavnagar. (TG-DTA) were simultaneously carried out using a SII-EXSTAR6000 TG-DTA 6300 apparatus. The experiments were conducted at a heating rate of 10 °C/min in a nitrogen atmosphere, covering a temperature range of 30–550 °C. The molar conductivity was measured in a 10^{-3} M DMF solution at room temperature using an EQ-664A conductivity meter. Powder X-ray diffraction (XRD) analysis was performed using a Rigaku SmartLab SE (3kW) instrument from Japan, with data collected via a D/teX Ultra 250 1D detector and processed using SmartLab Studio II software. The copper content in both complexes was determined gravimetrically and volumetrically after decomposing the samples with HNO_3.

4a.2.5 Computational analysis

Density functional theory (DFT) was used for the full geometry optimization of two complexes, **5** and **6**. B3LYP/6-31G level basis set was utlillized for the geometry optimization. All the calculations, HOMO-LUMO energy gap, NBO analysis, MESP and spin density of the molecule were carried out in Gauss View 6.0 software [16][17].

4a.2.6 *In vitro* anti-cancer activity

The antiproliferative properties of complex-**5** and complex-**6** were studied *in vitro* using the MTT assay. Complex-**6** showed greater effectiveness against cancer cells; therefore, an in-depth study was conducted on complex-**6**, such as a Live-dead assay and gene expression study. Apoptotic cell death was assessed using SH-SY5Y cells via the live-dead assay, which allowed for the identification of both apoptotic dead cells and live cells. This assay provided insights into the extent of cell death induced by the copper compound. Gene expression analysis was conducted to understand further the molecular mechanisms underlying their effects. The expression levels of the BCL2L1 and BAD genes were quantified, offering valuable markers for evaluating the complex's impact on apoptosis-related pathways.

4a.2.6.1 Cell culture conditions

Lung adenocarcinoma (NCI-H23), hepatocellular carcinoma (HepG2) and neuroblastoma (SH-SY5Y) cells were procured from the National Centre for Cell Science (NCCS), Pune. NCI-H23 Cells were cultured in RPMI-1640 medium (Himedia), SHSY-5Y and HepG2 cells were cultured in MEM medium supplemented with 10% fetal bovine serum and 1% penicillin-streptomycin solution (Gibco) at 37 °C in 5% CO_2 condition.

4a.2.6.2 MTT- Cell viability assay

Cell viability was evaluated using the MTT assay. Cells were cultured in 96-well plates (ThermoFisher Scientific) for 24 hr in cell culture medium at a density of 7,000 cells per well to allow for adhesion. The seeded cells were then treated with various concentrations of synthesized complex-**5** and complex-**6** for 24 hr at 37 °C in a 5% CO_2 incubator. The SH-SY5Y cells were also treated with different concentrations of cisplatin for 24 hr. After incubation, the media were removed, and the cells were washed with PBS. MTT (5 mg/ml) was then added to each well, and the plates were incubated for 4 hr at 37 °C in a 5% CO_2 atmosphere. Formazan crystals were dissolved in 100 µl of DMSO [18][19]. Absorbance was measured at 570 nm using a Synergy H1 Multi-Mode Microplate Reader to determine the optical density. IC_{50} values were calculated using GraphPad Prism software. The percentage of cell viability was calculated using the formula (1):

$$\% \text{ Cell viability} = (\text{OD of treatment} / \text{OD of control}) \times 100 \quad (1)$$

4a.2.6.3 Live/Dead assay

This is a cell staining procedure where cells are stained using specific dyes. The analysis was performed using the SH-SY5Y cell line. A total of 25×10^3 cells were seeded

per well in 8-well chamber slides (ThermoFisher Scientific) for 24 hr. The cells were treated with copper complex-**6**. After incubation, the cells were stained using a cytotoxicity kit (Invitrogen) with 2 µM calcein dye and 4 µM Ethidium homodimer (EthD-1) for 30 minutes, according to the manufacturer's protocol. Photographs were captured using a fluorescence microscope (Nikon-Ti2E). The percentage of dead cells was calculated using ImageJ software.

4a.2.6.4 Gene expression study

Real-time PCR has proven to be a reliable method for measuring gene expression levels. The use of real-time PCR for genetic analysis and RNA quantification is increasing [20]. In this method, SH-SY5Y neuroblastoma cells were cultured in a 6-well sterile culture plate. After 24 hr, the cells were treated with synthesized complex-**6** for another 24 hr. Cells were then collected in TRIzol reagent and RNA was isolated. The quality and quantity of the RNA were assessed using a Nanodrop. RNA was converted into cDNA using the High-Capacity cDNA Reverse Transcription Kit (Applied Biosystems). SYBR Green dye was used to detect fluorescence in a 12k Flex Real-Time PCR machine (Applied Biosystems). GAPDH served as the internal control, and the expression levels of the BAD and BCL2L1 genes were analyzed using the $2^{-\Delta\Delta CT}$ method.

4a.3 Results and Discussion

Two Copper(II) complexes were synthesized using a general method. Both complexes are stable at room temperature and have been characterized by FT-IR, UV–Vis, CV, ESR, TGA, and X-ray crystallography. Density functional theory (DFT) was employed for geometry optimization. Hirshfeld surface analysis was conducted to explore intermolecular interactions and crystal packing in the solid-state structures. The *in vitro* anticancer activity of both complexes was evaluated using cytotoxicity assays against three different cancer cell lines: NCI-H23, HepG2, and SH-SY5Y. The IC_{50} values of the synthesized complexes were determined. Due to the superior effectiveness of complex-**6** compared to complex-**5**, further studies, including live-dead assays and gene expression analysis, were performed on SH-SY5Y cancer cells using complex-**6**. The crystal structure and other characteristics of complex-**5** and complex-**6** are shown below

4a.3.1 FTIR spectral studies

FTIR spectral analysis is a valuable technique for identifying functional groups in a compound by measuring their distinct vibrational frequencies. The IR frequencies of the ν(C=O) group in benzoyl chloride and pyrazolone appear at 1577 cm^{-1} and 1602 cm^{-1},

respectively, for complex-**5**. For complex-**6**, the ν(C=O) frequencies of benzoyl chloride and pyrazolone are observed at 1586 cm^{-1} and 1601 cm^{-1}, respectively. A significant shift in IR frequencies occurs during the formation of the metal complex due to the formation of the M-O bond. During complexation, the charge from the O-atom of the C=O group in pyrazolone is transferred to the metal ion, which strengthens the M-O bond and weakens the C=O bond, leading to an increase in the bond length of the pyrazolone C=O bond [21]. Other FTIR frequencies are shown in the table below. The FTIR frequencies for complexes **5** and **6** are provided in **Table 4a.1** and the FTIR spectra of complex-**5** and complex-**6** are shown in **Figs.4a.4-4a.5.**

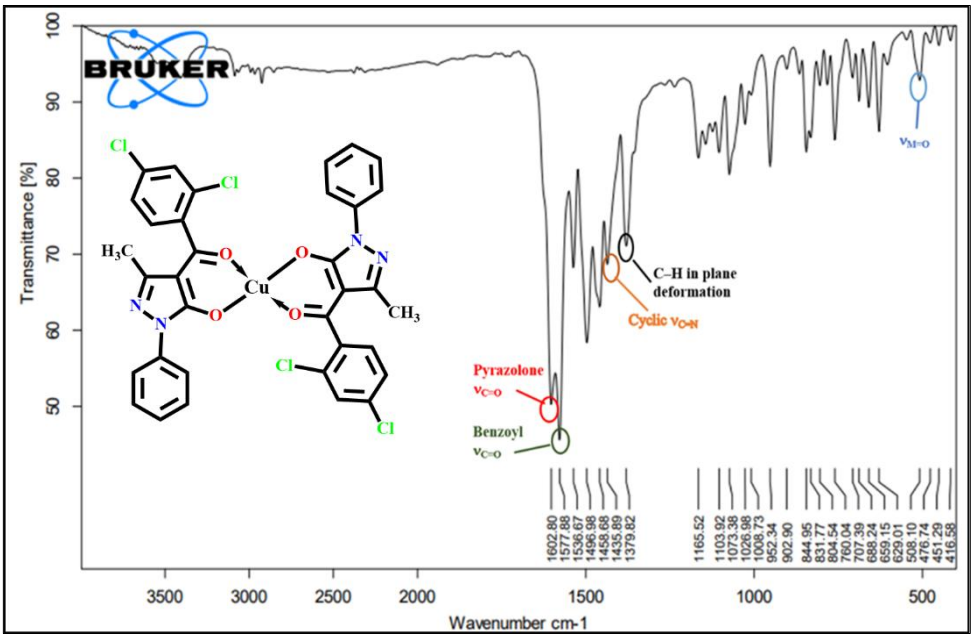

Fig.4a.4. FTIR spectrum of complex-5

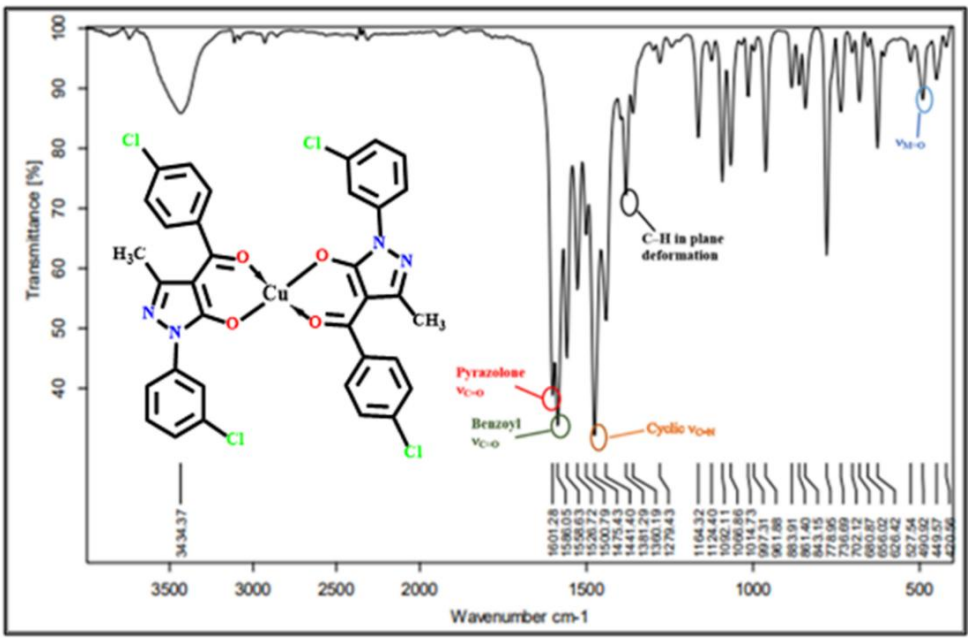

Fig.4a.5. FTIR spectrum of complex-6

Table 4a.1. FTIR spectral data of ligands, complexes 5 and 6

Code	HL^{I} ligand	Complex-5	HL^{V} ligand	Complex-6
ν(C=O) of benzoyl chloride	1587	1577	1590	1586
ν(C=O) of Pyrazolone	1627	1602	1625	1601
Cyclic ν(C=N)	1515	1435	1551	1475
C–H in-plane deformation	1394	1379	1385	1360
ν_{M-O}	-	508	-	490

4a.3.2 Molar conductivity measurements

The molar conductance of complexes **5** and **6** was measured in a 10^{-3} M DMF solution. The molar conductivity ($\Lambda_o M$) values were found to be 3.27 and 2.18 ohm^{-1} cm^2mol^{-1} complex-**5** and complex-**6,** respectively. These lower molar conductivity values suggest the non-electrolytic behaviour of the complexes and the absence of counter ions in the coordination sphere [22].

4a.3.3 Thermogravimetric analysis

Thermogravimetric analysis (TGA) provides insight into the mass change of a material as a function of temperature. The two-step decomposition of two square-planar copper complexes can be examined using this technique. Both complexes thermally decompose between 100 and 550°C, demonstrating their remarkable thermal stability. The spectra include three differently coloured graphs: blue (TGA), green (DTA), and red (DTG). No solvent degradation is observed up to 250°C, indicating the absence of solvent molecules at the fifth position in both complexes. Degradation of one molecule HL^{I} ligand occurs in the range of 280-320°C in a single step. The second step involves pyrolysis of the second moiety of HL^{I} ligand up to 480°C in complex-**5.** A 76.5% degradation of both ligands is observed in the TG graph, with copper oxide (CuO) remaining as the final product, stable up to 550°C. At 316.8°C, a shift of 1.173 mg/min is observed in the DTG curve. The TGA curve of complex-**6** shows a similar pattern, with complete pyrolysis of both HL^{V} ligands up to 480°C, resulting in a 63.5% degradation of the ligands. The TG-DTA curves for both complexes **5** and **6** are shown in **Figs.4a.6 and 4a.7.**

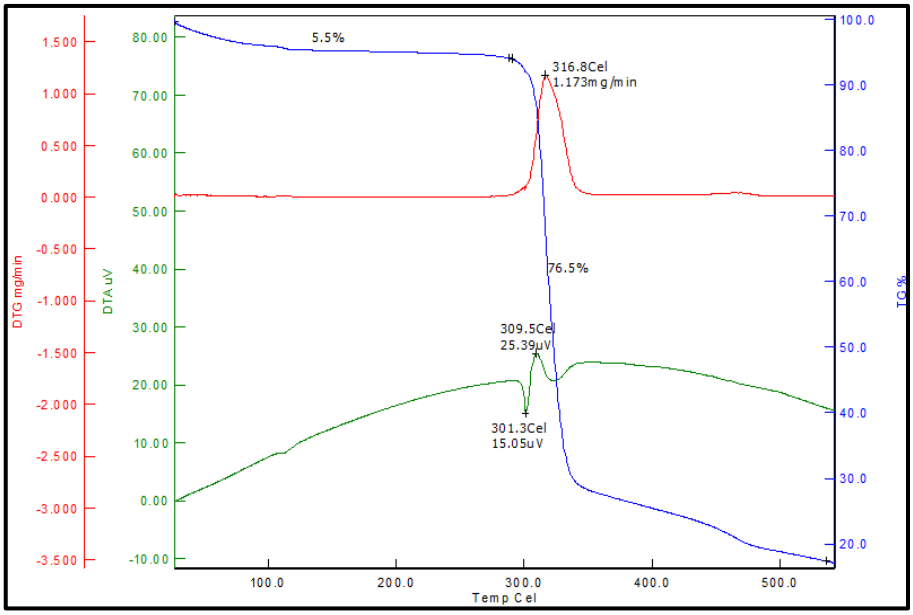

Fig.4a.6. TG-DTA plot of complex-5

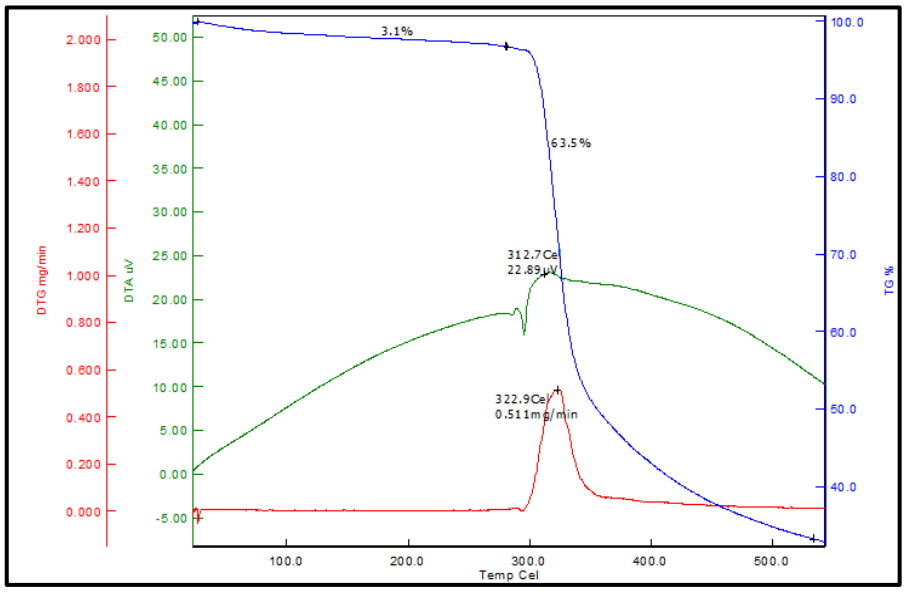

Fig.4a.7. TG-DTA plot of complex-6

4a.3.4 Electronic spectral analysis

The UV-visible absorption spectroscopy is widely used to provide structural information about compounds. The electronic spectra of both square-planar complexes were recorded in DMSO solvent. The d-d bands for both complexes were measured at 10^{-3} M DMSO solvent. For complex-**5**, the sharp absorption bands occur at 277 nm (36101 cm^{-1}) and 333 nm (30030 cm^{-1}). For complex-**6,** these transitions are observed at different wavelengths: 283 nm (35335 cm^{-1}) and 352 nm (28409 cm^{-1}). The transitions observed at **277 nm** and **283 nm** are assigned to **ligand-to-metal charge transfer (LMCT),** where the electron density is transferred from the oxygen donor atoms of the pyrazolone ligand to the Cu(II) centre. The absorptions at **333 nm** and **352 nm** could be interpreted as **intra-ligand**

charge transfer (ILCT); however, they are more likely **ligand-based transitions**, such as **π→π*** or **n→π*** excitations within the pyrazolone ligand's π-electron system. Furthermore, both complexes exhibit a broad d-d transition band at 742 nm (13477 cm^{-1}) for complex-**5** and 739 nm (13531 cm^{-1}) for complex-**6** in the visible region. The absorbance values at 742 nm are 0.31 and 0.46 at 739 nm for complex- **5** and complex **6.** respectively. The broad d-d transitions correspond to the $\mathbf{d_{xy} \rightarrow d_{x^2-y^2}}$ which mainly occurs in square planar Cu(II) complexes [23][24][25]. **Figs.4a.8-4a.9** represent the electronic transition of both complexes.

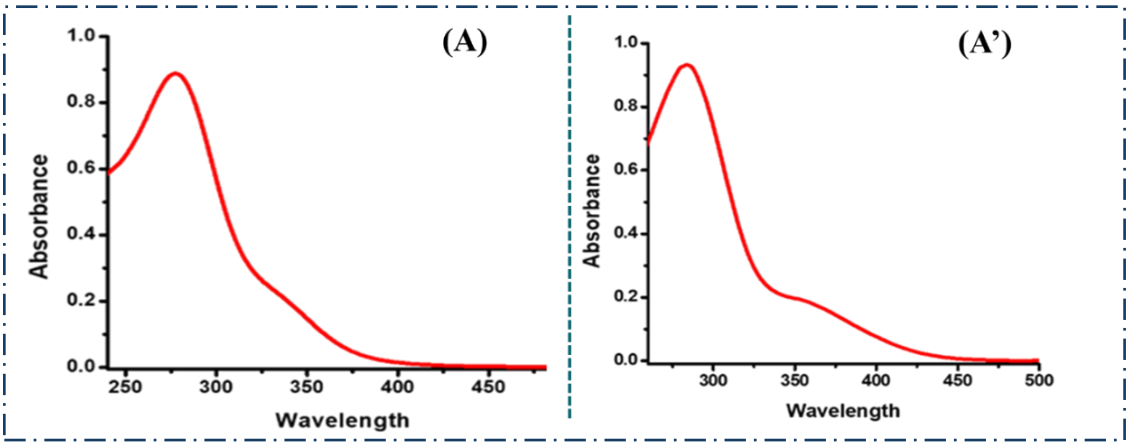

Fig.4a.8. LMCT & ligand-based transitions in (A) complex-5 and (A') complex-6 in a diluted solution of DMSO

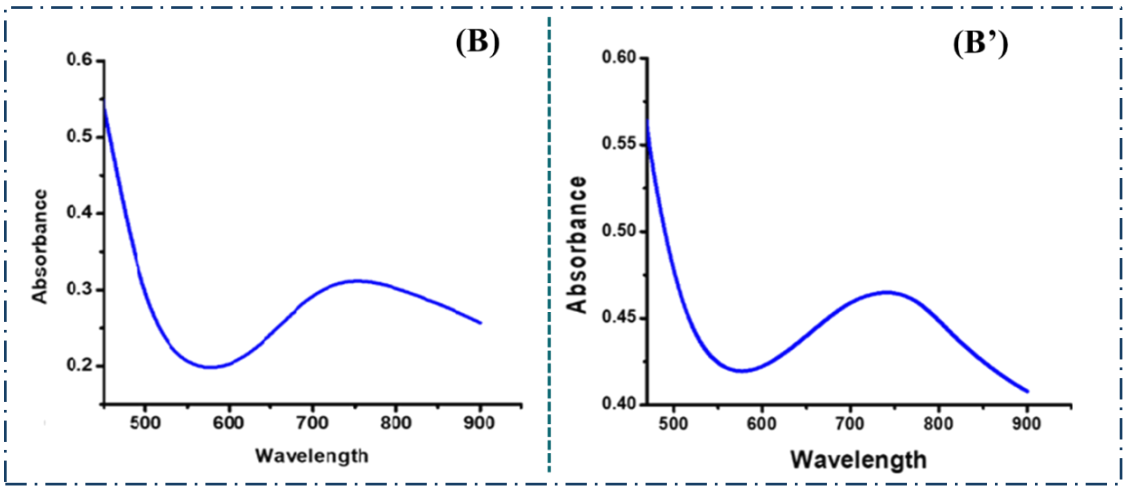

Fig.4a.9. d-d transition of (B) complex-5 and (B') complex-6 in a $1x10^{-3}$ M solution of DMSO

4a.3.5 Single crystal X-ray diffraction analysis

The synthesized two copper complexes are green in colour and were obtained after the complexation reaction with acypyrazolone ligand and recrystallized in DMF solvent. The structural analysis evidenced that the Cu metal centre is surrounded by four oxygen atoms

from ligands in both complexes. The geometry of both complexes **5** and **6** appear in the form of a square planar. Complex-**5** and complex-**6** crystallize in '**Triclinic space group *P*-1'** while complex-**6** crystallizes in '**Monoclinic space group *P*2$_1$/c'**. It includes a two-fold screw axis and a glide plane. Its lattice angles are generally non-orthogonal, with one angle being exactly 90°. The symmetry elements of complex-**6** are depicted below in **Fig.4a.12.** The Cu-O bond lengths are closely comparable in the two complexes, varying in the range 1.268(5)- 1.929(3) for complex-**5** and 1.269(4)-1.928(2) for complex-**6.** In complex-5, a HL^{I} ligand and in complex-**6**, a HL^{V} ligand coordinates the Cu(II) metal with chelating angles of 93.52(10)° and 93.53(10)°, with pyrazolone oxygens of ligands. Thermal ellipsoid plots (ORTAP diagrams) of complex-**5** and complex-**6** are pictured in **Fig.4a.10.** The perspective view of the packing configuration of complex-**5** and complex-**6** are shown in **Fig.4a.11.** Bond lengths and bond angles parameters, hydrogen bonds parameters and symmetry transformations of complex-**5** are listed in **Table 4a.2-4a.4**, respectively. Similar data for complex-**6** are provided in **Table 4a.5-4a.7**, respectively. All the refinement parameters and crystal data of complexes **5** and **6** are shown in **Table 4a.8**. **Fig.4a.13** pictured the 2D representation of the single crystal structures of complex-**5** and complex-**6.**

(A)

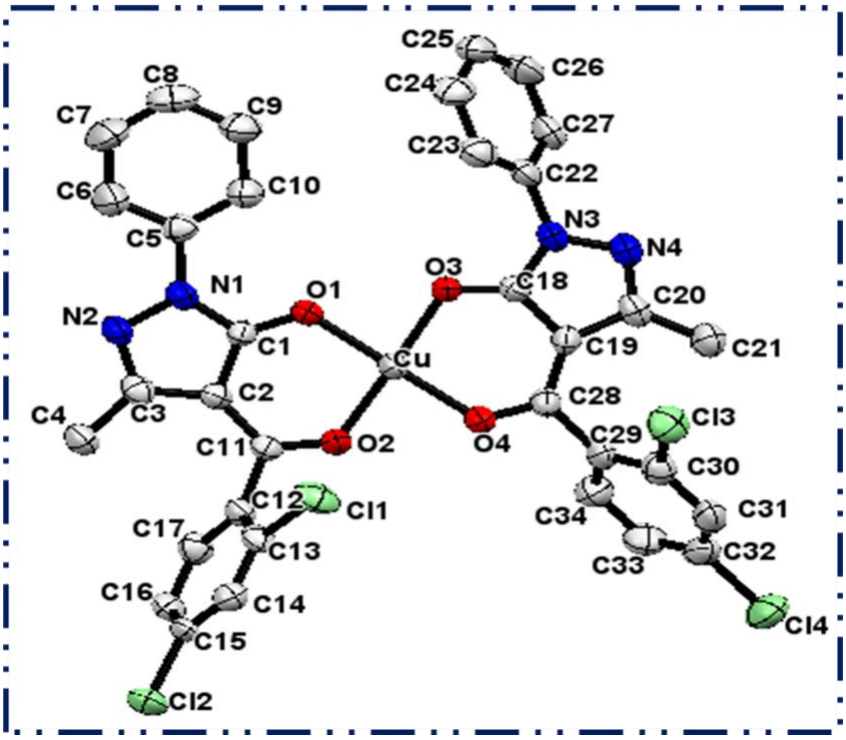

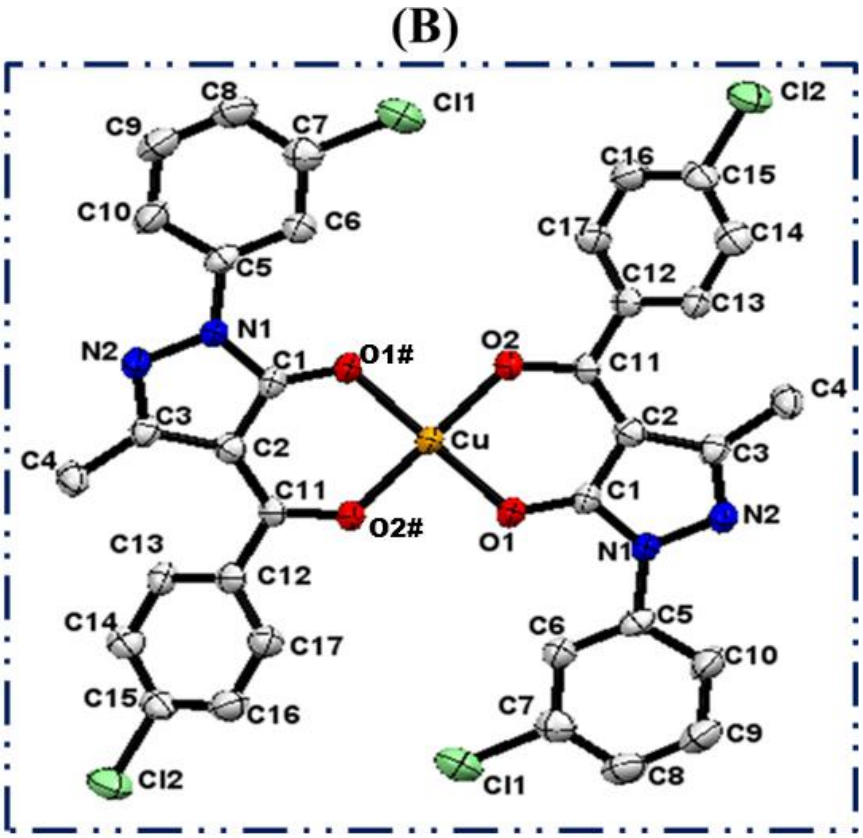

Fig.4a.10. Thermal ellipsoid plots (without H-atoms for clarity) With 55% probability of (A) complex-5 and (B) complex-6

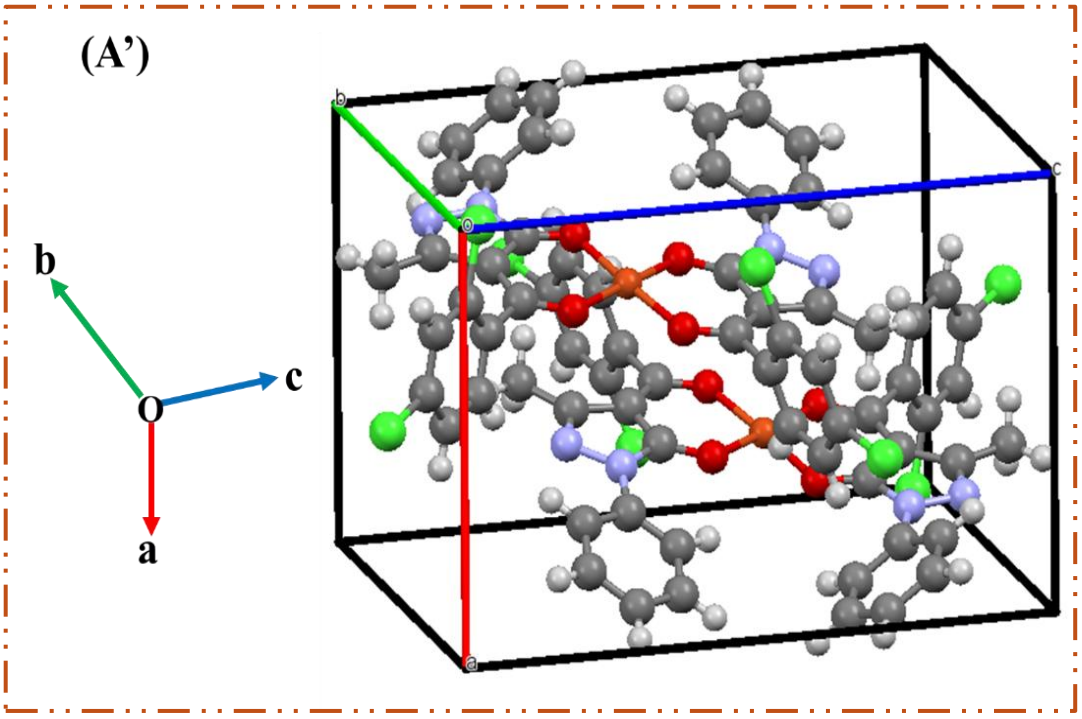

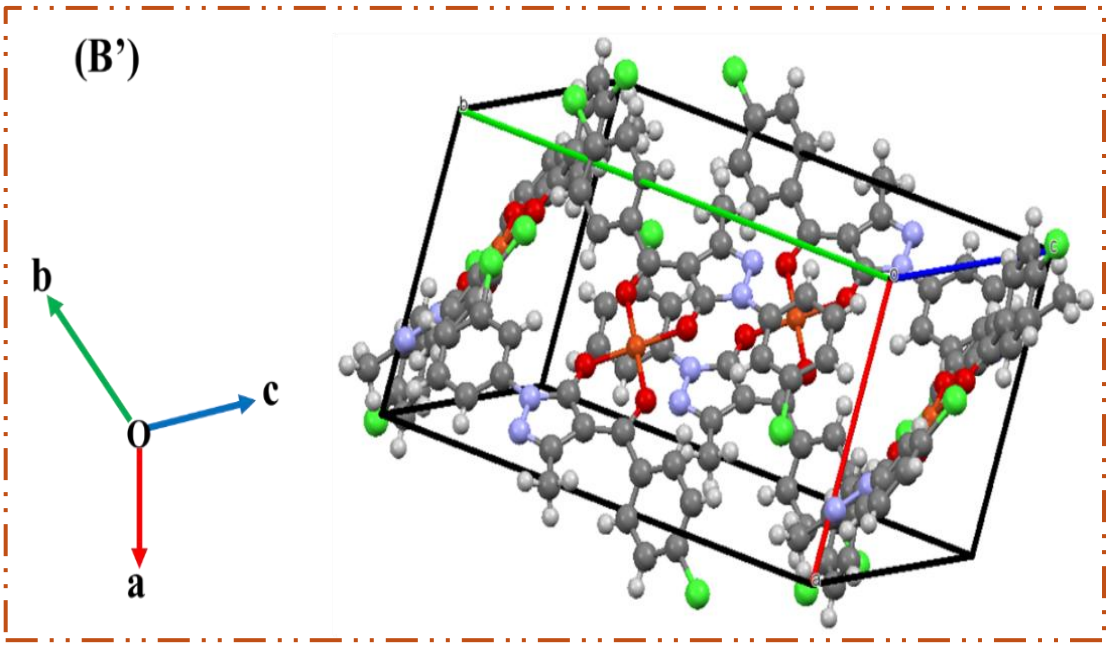

Fig.4a.11 The perspective view of the packing configuration of (A') complex-5 and (B') complex-6 along with b-axis

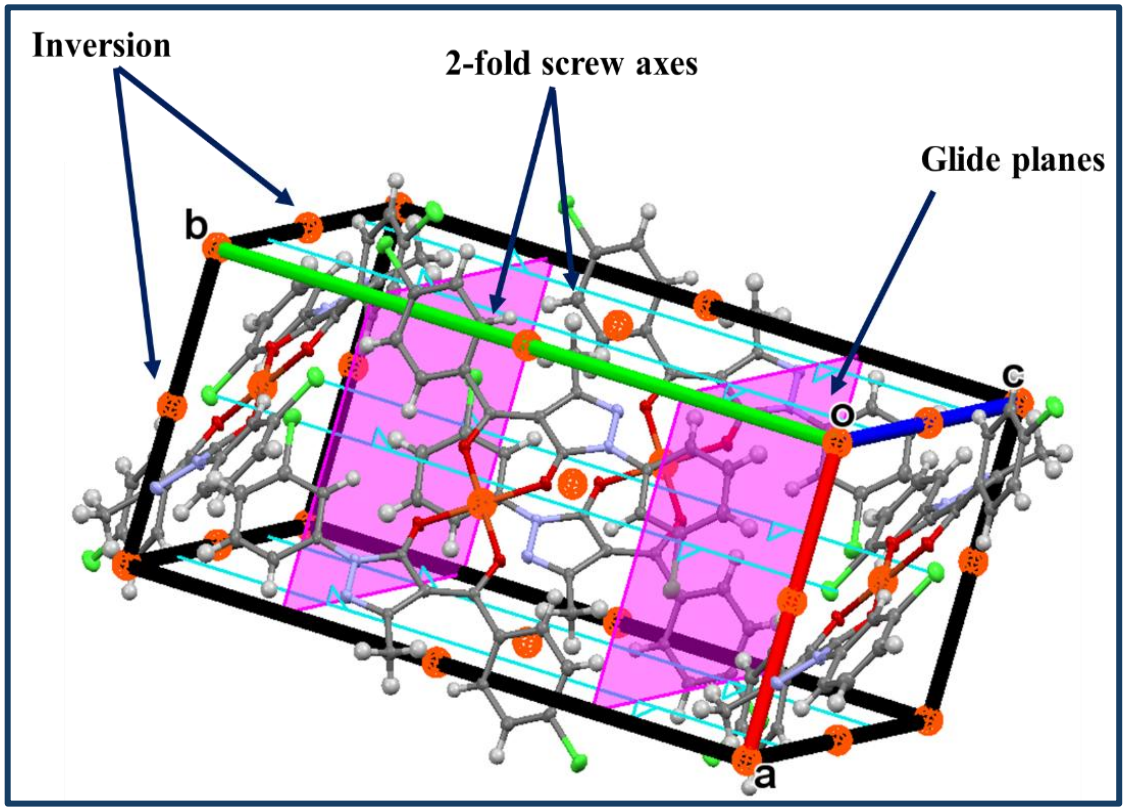

Fig.4a.12. Symmetry elements present in complex-6

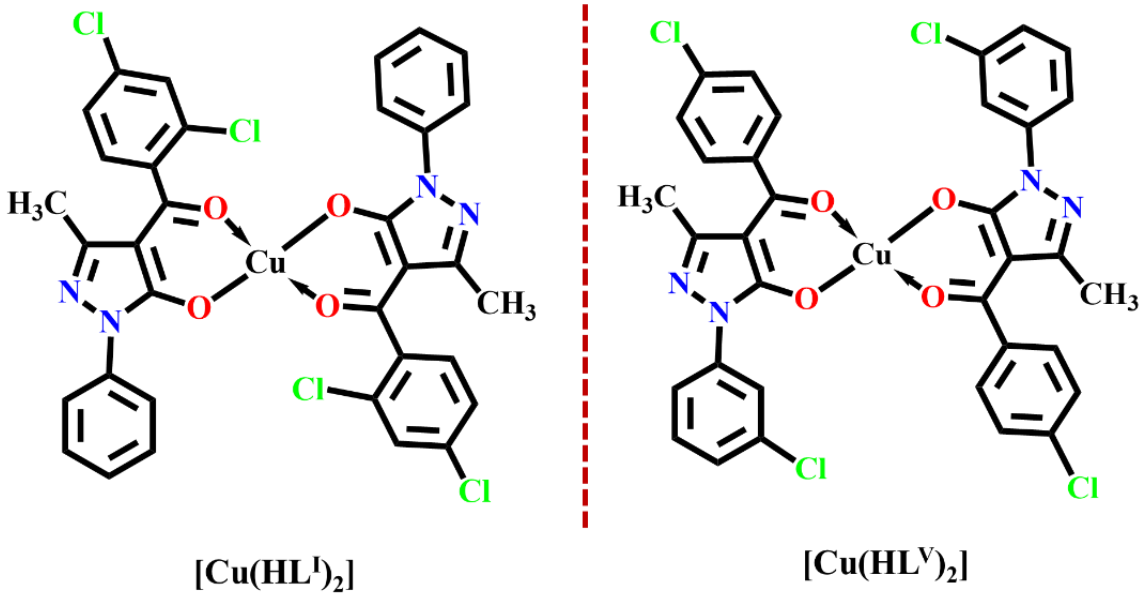

Fig.4a.13. 2D representation of the single crystal structures of complex-5 and complex-6

Table 4a.2 Bond lengths & Bond angles parameters of complex-5

Atoms	Bond lengths (Å)	Atoms	Bond lengths (Å)	Atoms	Bond angles (°)	Atoms	Bond angles (°)
Cu(1)-O(1)	1.902(3)	N(3)-N(4)	1.401(5)	O(1)-Cu-O(3)	84.03(11)	C(3)-N(2)-N(1)	106.2(3)
Cu(1)-O(2)	1.924(3)	N(1)-C(1)	1.353(5)	O(1)-Cu-O(2)	93.83(11)	C(18)-N(3)-N(4)	112.3(3)
Cu(1)-O(3)	1.906(3)	N(1)-C(5)	1.433(5)	O(3)-Cu-O(2)	177.55(12)	N(4)-N(3)-C(22)	120.1(3)
Cu(1)-O(4)	1.929(3)	N(2)-C(3)	1.310(5)	O(1)-Cu-O(4)	176.65(12)	O(2)-C(11)-C(9)	123.0(3)
Cl(1)-C(13)	1.740(4)	N(3)-C(18)	1.356(5)	O(3)-Cu-O(4)	94.92(11)	C(14)-C(13)-Cl(1)	117.9(3)
Cl(2)-C(15)	1.734(4)	N(3)-C(22)	1.430(5)	O(2)-Cu-O(4)	87.28(11)	C(12)-C(13)-Cl(1)	119.8(3)
Cl(3)-C(30)	1.730(5)	N(4)-C(20)	1.299(6)	C(1)-Cu-O(1)	122.8(2)	C(14)-C(15)-Cl(2)	118.9(3)
Cl(4)-C(32)	1.747(4)	C(1)-C(2)	1.426(5)	C(11)-Cu-O(2)	122.8(2)	C(16)-C(15)-Cl(2)	119.8(3)
O(1)-C(1)	1.277(4)	C(2)-C(11)	1.405(5)	C(18)-Cu-O(3)	121.2(2)	C(29)-C(30)-Cl(3)	119.8(3)
O(2)-C(11)	1.268(5)	C(12)-C(13)	1.393(6)	C(28)-O(4)-Cu	126.9(3)	C(31)-C(30)-Cl(3)	118.8(3)
O(3)-C(18)	1.271(5)	C(30)-C(31)	1.382(6)	C(1)-N(1)-N(2)	111.4(3)	C(31)-C(32)-Cl(4)	118.6(4)
O(4)-C(28)	1.267(5)	C(6)-H(6)	0.9500	C(1)-N(1)-C(5)	129.3(3)	C(33)-C(32)-Cl(4)	119.6(4)
N(1)-N(2)	1.405(4)	C(4)-H(4)	0.9800	N(2)-N(1)-C(5)	118.8(3)	O(4)-C(28)-C(19)	124.2(4)

Table 4a.3. Hydrogen bonds of complex-5

D-H...A	d(D-H)	d(H...A)	d(D...A)	<(DHA)
C(10)-H(10A)...O(1)	0.95	2.23	2.865(5)	123.5
C(21)-H(21C)...Cl(3)	0.98	2.98	3.728(5)	134.1
C(31)-H(31A)...Cl(3)#1	0.95	2.99	3.826(5)	147.8

Table 4a.4. Complex-5: Symmetry transformations used to generate equivalent atoms

	Symmetry transformations
1	-x+2,-y+2,-z+2

Table 4a.5. Bond lengths & Bond angles parameters of complex-6

Atoms	Bond lengths (Å)	Atoms	Bond lengths (Å)	Atoms	Bond angles (°)	Atoms	Bond angles (°)
Cu(1)-O(1)	1.913(2)	C(1)-C(3)	1.442(4)	O(1)-Cu-O(1)#1	180.0	N(2)-N(1)-C(5)	119.5(3)
Cu(1)-O(1)#	1.913(2)	C(5)-C(10)	1.396(5)	O(1)-Cu-O(2)	93.52(10)	C(3)-N(2)-N(1)	106.0(3)
Cu(1)-O(2)	1.928(2)	C(8)-C(9)	1.389(6)	O(1)#-Cu-O(2)	86.48(10)	O(1)-C(1)-N(1)	123.9(3)
Cu(1)-O(2)#	1.928(2)	C(4)-H(4)	0.9800	O(1)-Cu-O(2)#	86.47(10)	O(1)-C(1)-C(2)	130.2(3)
Cl(1)-C(7)	1.750(4)	C(6)-H(6)	0.9500	O(1)#-Cu-O(2)#	93.53(10)	N(2)-C(3)-C(2)	111.3(3)
Cl(2)-C(15)	1.736(4)	N(1)-C(1)	1.361(4)	O(2)-Cu-O(2)#	180.0	N(2)-C(3)-C(4)	118.8(3)
O(1)-C(1)	1.280(4)	N(1)-C(5)	1.424(4)	C(1)-O(1)-Cu	119.6(2)	C(6)-C(5)-C(10)	121.2(3)
O(2)-C(11)	1.269(4)	N(2)-C(3)	1.316(4)	C(11)-O(2)-Cu	128.8(2)	C(8)-C(7)-Cl(1)	119.5(3)
C(2)-C(11)	1.416(5)	N(1)-N(2)	1.396(4)	C(1)-N(1)-N(2)	112.1(3)	C(14)-C(15)-Cl(2)	118.8(3)

Table 4a.6. Hydrogen bonds of complex-6

D-H...A	d(D-H)	d(H...A)	d(D...A)	<(DHA)
C(4)-H(4A)...O(2)#2	0.98	2.41	3.267(4)	145.9
C(4)-H(4B)...N(2)#3	0.98	2.64	3.496(5)	145.9
C(6)-H(6A)...O(1)	0.95	2.27	2.862(4)	119.3
C(8)-H(8A)...Cl(1)#4	0.95	2.92	3.830(4)	160.9

Table 4a.7. Complex-6: Symmetry transformations used to generate equivalent atoms

	Symmetry transformations
1	-x+1,-y+1,-z
2	x,y,z+1
3	-x,-y+1,-z+1
4	x,-y+1/2, z+1/2

Table 4a.8. Refinement parameters of complex-5 and complex-6

CODE	$[Cu(HL^{I})_2]$ Complex-5	$[Cu(HL^{V})_2]$ Complex-6
CCDC number	2263830	2263831
Chemical formula	$C_{34}H_{22}Cl_4CuN_4O_4$	$C_{34}H_{22}Cl_4CuN_4O_4$
Formula weight	755.89	755.89
Crystal system	Triclinic	Monoclinic
Space group	*P*-1	$P2_1/c$
Temperature	100(2) K	100(2) K
Wavelength	0.71073 Å	0.71073 Å
Z	2	2
Density	1.619 Mg/m^3	1.588 Mg/m^3
Unit cell dimension	a= 9.6075(12) Å b= 11.7452(15) Å c= 14.3696(17) Å α = 90.834(4)° β= 95.017(4)° γ = 106.124(4)°	a = 9.0930(11) Å b = 27.412(3) Å c = 6.8238(8) Å α,γ= 90° β= 111.660(4)°
F (0 0 0)	766	766
Theta range	2.217 to 26.463°	2.522 to 29.730°
R(int)	0.0738	0.0813
Absorption Correction	None	Semi-empirical from equivalents
Index ranges	-12<=h<=12, -14<=k<=14, -17<=l<=17	-12<=h<=12, -38<=k<=37, -7<=l<=9
Reflections collected	32881	27152
Goodness-of-fit on F^2	1.089	1.152
R indices	R1 = 0.0763, wR2 = 0.1596	R1 = 0.0766, wR2 = 0.1619
Data/restraints/parameters	6326 / 0 / 426	4458 / 0 / 215
Largest diff. Peak and hole	1.153 and -0.551 $e.Å^{-3}$	1.268 and -0.876 $e.Å^{-3}$

4a.3.6 Powder XRD study

Using a slow evaporation method, green, plate-like, X-ray-quality crystals of both copper complexes were produced. Powder XRD is a widely recognized technique for bulk characterization. X-ray powder diffraction (XRD) is a rapid analytical method used for phase identification in crystalline materials and can also provide information about unit cell dimensions. The material is homogenized and coarsely ground to analyze its average composition. A simulated pattern for both complexes was derived from the single crystal data and compared with the experimental pattern from the powder XRD experiment. The

simulated diffraction patterns for both complexes closely matched the experimental results, as shown in **Figs.4a.14-4a.15.** This confirms that the bulk products are essentially the same as those present in the single-crystal form. It also demonstrates that the geometry and structure of each complex are identical. Additionally, this indicates that the structure obtained from a single crystal accurately represents the majority of the complexes. A sharp band with maxima in the 2θ = 20 to 25° range for complex-**5** and in the 2θ = 5 to 10° range for complex-**6** was observed in the XRD graph [26].

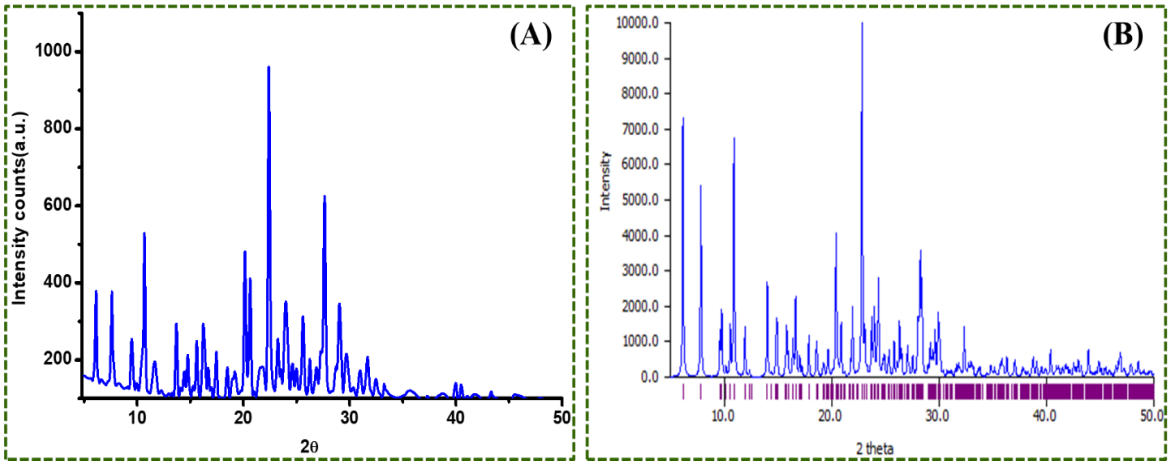

Fig.4a.14. Comparison of the powder XRD patterns for complex-5 in (A) the experimental and (B) the simulated

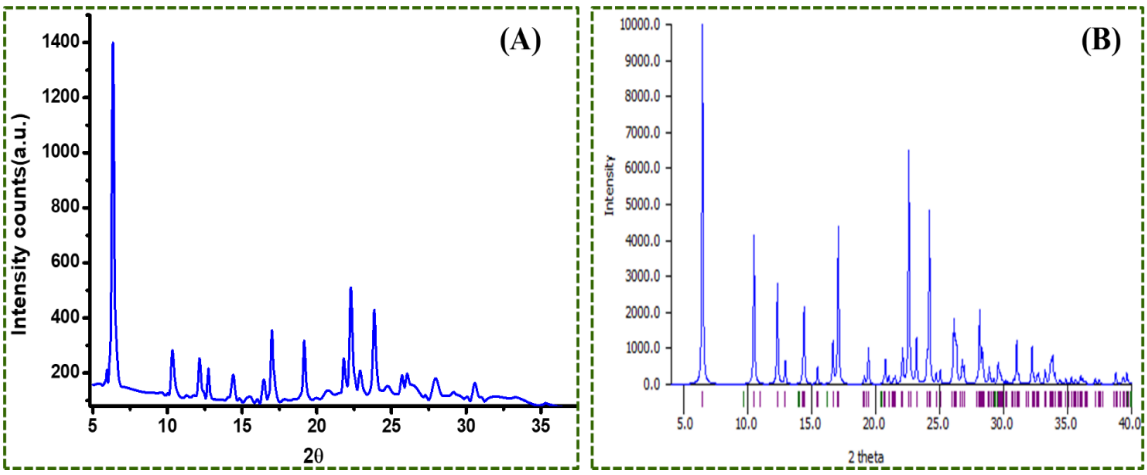

Fig.4a.15. Comparison of the powder XRD patterns for complex-6 in (A) the experimental and (B) the simulated

4a.3.7 DFT based computational analysis

DFT aids in determining the most stable molecular structures by optimizing geometries to minimize their energy. The optimized geometry computed for both complexes was calculated by the B3LYP/6-31G level basis set [16][17]. Gaussview 6.0 software was used to process the input files of both complexes [27]. The optimization energy values for complex-**5** and complex-**6** are -144.475 keV and -144.475 keV, respectively. The DFT

calculations ultimately support the square planar geometry of both synthesized copper acylpyrazolone complexes. **Fig.4a.16** represents the optimized structure of complex-**5** and complex-**6**. The optimization energy value of both copper complexes is highly negative than ligand (**HL^I ligand= -49.934 keV**), which shows the stability of the synthesized complexes. DFT analysis of ligands has already been stated in Chapter **2**.

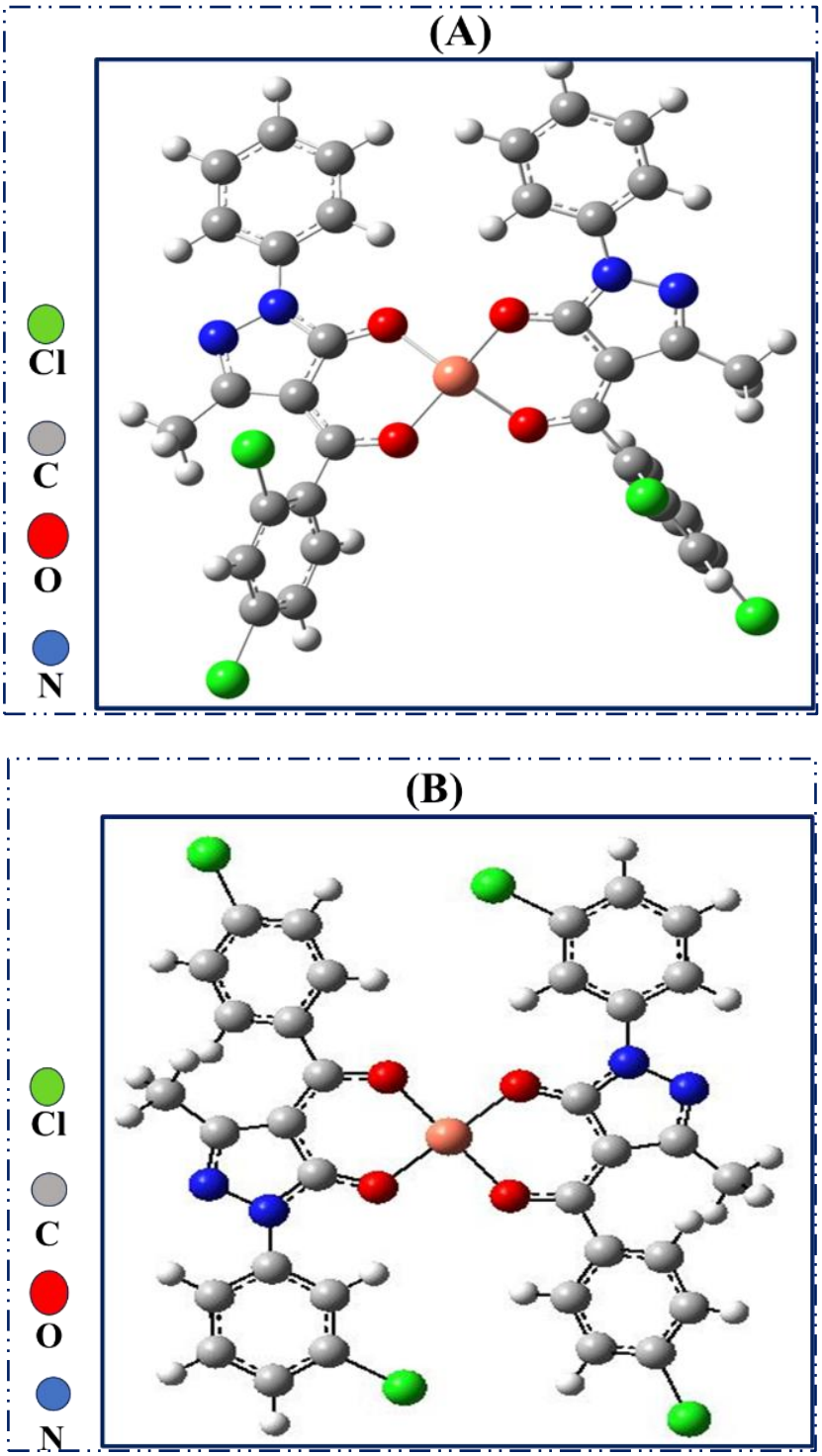

Fig.4a.16. DFT optimized Structures of (A) complex-5 and (B) complex-6

HOMO-LUMO energies play a crucial role in determining various chemical interactions. Given the importance of frontier orbitals in chemical stability, energy values,

and chemical behaviour, initial results were obtained by analyzing these orbitals. The distribution of frontier orbitals can be used to identify active sites and assess the reactivity of the complexes. HOMO-LUMO analysis provides insights into the nature of a molecule, such as its hardness, softness, and reactivity. The six frontier molecular orbitals (FMOs) of complexes **5** and **6** are shown in **Fig.4a.17.** The negative energy values indicate the stability of the complexes. The highest occupied molecular orbitals (HOMOs) are primarily located around the acylpyrazolone ligand [28]. Global parameters such as ionization potential, chemical potential, electron affinity, electronegativity, global hardness, softness, and electrophilicity index for complexes **5** and **6** can be inferred from the energy gap (ΔE). The stability and reactivity of the molecules can be deduced from global factors like electronegativity, chemical hardness, and softness in DFT simulations. These parameters not only aid in understanding and designing chemical systems but also help predict a molecule's behaviour in reactions, including its electron affinity and chemical properties. The global parameters for complex-**5** and complex-**6** are presented in **Table 4a.9-4a.10**, respectively. **Table 4a.11** shows a comparison of the practical and theoretical bond parameters**.** The band gap (ΔE) values for complex-**5** are 4.007 eV, 4.033 eV, and 5.375 eV for HOMO to LUMO, HOMO-1 to LUMO+1, and HOMO-2 to LUMO+2, respectively. For complex-**6**, these values are 3.884 eV, 4.275 eV, and 5.765 eV, respectively. The HOMO-LUMO energy gap is critical in determining the electrical transport characteristics of molecules. A high HOMO-LUMO gap typically indicates a stable molecule with low chemical reactivity [29][30]. The energy gap (ΔE) for complex-**5** is 4.007 eV, and for complex-**6**, it is 3.884 eV. Therefore, complex-**5** is more stable due to its higher ΔE value, while complex-**6** is more reactive because of its lower ΔE value. The stability order is,

complex-5 > complex-6

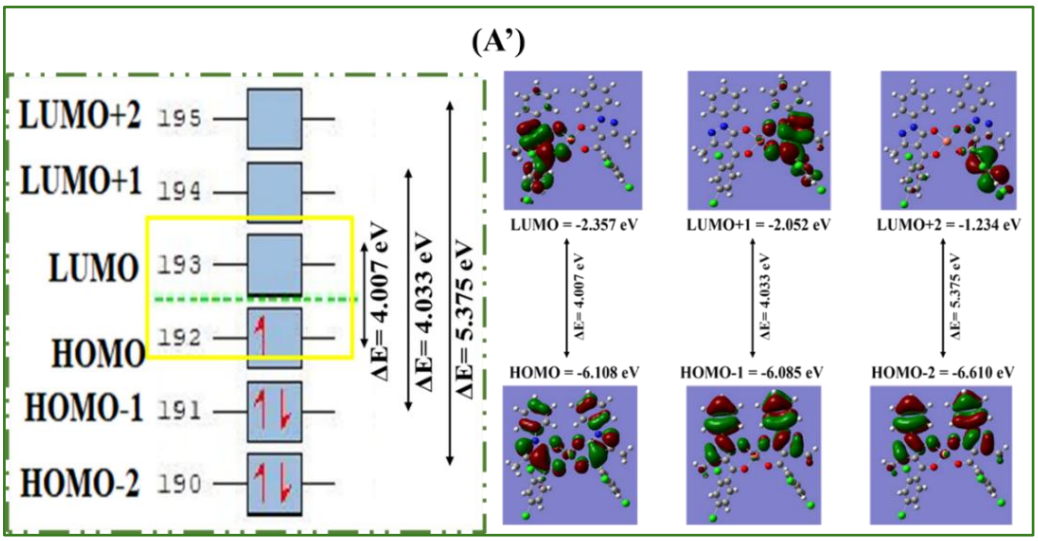

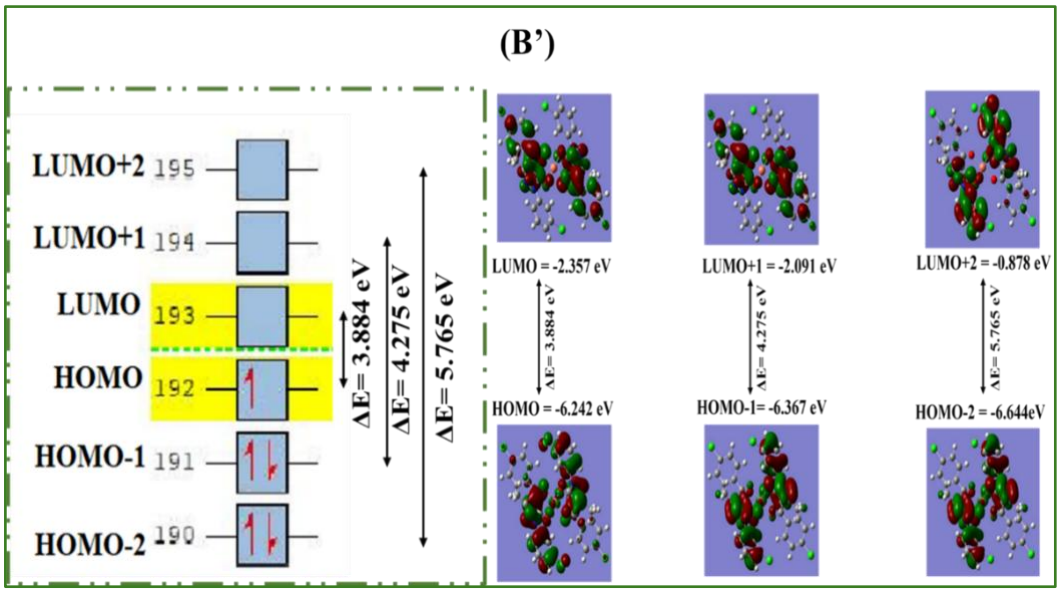

Fig.4a.17. HOMO–LUMO frontier orbital analysis energy diagram of (B) complex-5 and (B') complex-6

Table 4a.9. Global parameters of complex-5

Properties	Mathematical Formula	Complex-5
E_{HOMO}	E_{HOMO}	- 6.108
E_{LUMO}	E_{LUMO}	-2.101
ΔE	$\Delta E = E_{LUMO} - E_{HOMO}$	4.007
Ionization potential (IP)	$IP = -E_{HOMO}$	6.108
Chemical Potential (μ)	$\mu = 1/2 (E_{HOMO} + E_{LUMO})$	-4.104
Electron affinity (EA)	$EA = -E_{LUMO}$	2.101
Electronegativity (EN)	$EN = -1/2 (E_{HOMO} + E_{LUMO})$	4.104
Global Hardness (Ƞ)	$\eta = -1/2 (E_{HOMO} - E_{LUMO})$	2.003
Softness (S)	$S = 1/2\eta$	0.249
Electrophilicity index (ω)	$\omega = \mu^2/2\eta$	4.204

Table 4a.10. Global parameters of complex-6

Properties	Mathematical Formula	Complex-6
E_{HOMO}	E_{HOMO}	-6.242
E_{LUMO}	E_{LUMO}	-2.357
ΔE	$\Delta E = E_{LUMO} - E_{HOMO}$	3.885
Ionization potential (IP)	$IP = -E_{HOMO}$	6.242
Chemical Potential (μ)	$\mu = 1/2 (E_{HOMO} + E_{LUMO})$	-4.299
Electron affinity (EA)	$EA = -E_{LUMO}$	2.357
Electronegativity (EN)	$EN = -1/2 (E_{HOMO} + E_{LUMO})$	4.299
Global Hardness (Ƞ)	$\eta = -1/2 (E_{HOMO} - E_{LUMO})$	1.942
Softness (S)	$S = 1/2\eta$	0.257
Electrophilicity index (ω)	$\omega = \mu^2/2\eta$	4.758

Table 4a.11. A comparison of the practical and theoretical bond parameters

Atoms	Practical bond length (Å)	Theoretical bond length (Å)	Atoms	Practical bond angles (°)	Theoretical bond angles (°)
Complex-5					
Cu(1)-O(1)	1.902(3)	1.913	O(1)-Cu(1)-O(3)	84.03(11)	93.46
Cu(1)-O(2)	1.924(3)	1.926	O(1)-Cu(1)-O(2)	93.83(11)	93.84
Cu(1)-O(3)	1.906(3)	1.914	O(3)-Cu(1)-O(4)	94.92(11)	93.88
Cu(1)-O(4)	1.929(3)	1.919	O(2)-Cu(1)-O(4)	87.28(11)	93.28
Cl(1)-C(13)	1.740(4)	1.822	N(2)-N(1)-C(5)	118.8(3)	118.80
Cl(2)-C(15)	1.734(4)	1.819	C(3)-N(2)-N(1)	106.2(3)	106.70
Cl(3)-C(30)	1.730(5)	1.823	C(1)-O(1)-Cu(1)	122.8(2)	123.20
Cl(4)-C(32)	1.747(4)	1.819	C(11)-O(2)-Cu(1)	128.4(2)	128.82
O(1)-C(1)	1.277(4)	1.299	C(18)-O(3)-Cu(1)	121.2(2)	122.97
O(2)-C(11)	1.268(5)	1.301	C(28)-O(4)-Cu(1)	126.9(3)	129.03
N(1)-N(2)	1.405(4)	1.424	O(1)-C(1)-N(1)	123.7(3)	124.71
N(1)-C(1)	1.353(5)	1.369	N(2)-C(3)-C(4)	118.9(3)	119.14
Complex-6					
Cu(1)–O(1)	1.913(2)	1.911	O(1)–Cu–O(1)#1	180	180.0
Cu(1)–O(2)	1.928(2)	1.926	O(1)#1–Cu–O(2)	86.48(0)	88.40
Cl(1)–C(7)	1.750(4)	1.833	O(1)–Cu–O(2)#1	86.47(1)	88.40
Cl(2)–C(15)	1.736(4)	1.822	C(1)–O(1)–Cu	119.6(2)	123.52
O(1)–C(1)	1.280(4)	1.992	C(11)–O(2)–Cu	128.8(2)	131.42
N(1)–N(2)	1.391(4)	1.419	C(1)–N(1)–C(5)	128.3(3)	130.1
N(1)–C(1)	1.361(4)	1.373	C(3)–N(2)–N(1)	106.0(3)	106.60
N(1)–C(5)	1.424(4)	1.423	N(1)–C(1)–C(2)	105.9(3)	106.52
N(2)–C(3)	1.316(4)	1.327	C(6)–C(5)–N(1)	120.6(3)	120.82

The optimized geometries of complex-**5** and complex-**6** were utilized for vibrational frequency analysis. Theoretical vibrations can be used to investigate the changes which occur during complexation. Following convergence, harmonic vibrational frequencies were calculated at the same theoretical level to ensure no imaginary frequencies were present at the stationary points. The comparison between theoretical values and experimental spectra is particularly significant, as highlighted in the FTIR spectroscopic analysis section. Theoretical IR frequencies were obtained using DFT calculations. Key theoretical vibrational frequencies, alongside the corresponding experimental FTIR values, are provided in **Table 4a.12.** The DFT-optimized IR spectra are illustrated in **Figs.4a.18–4a.19.** Theoretical IR frequencies are always larger than practical IR frequencies because theoretical FTIR calculations generally model molecules in an isolated gas-phase state, neglecting the effects of external forces such as hydrogen bonding and intermolecular

interactions which common in practical experiments. These real-world factors and anharmonic vibrational behaviour lower the frequencies observed in experimental FTIR measurements. Additionally, computational methods often simplify molecular vibrations using harmonic assumptions, leading to higher predicted frequencies compared to practical data. The discrepancies arise due to these approximations and environmental effects not accounted for in theoretical models [31].

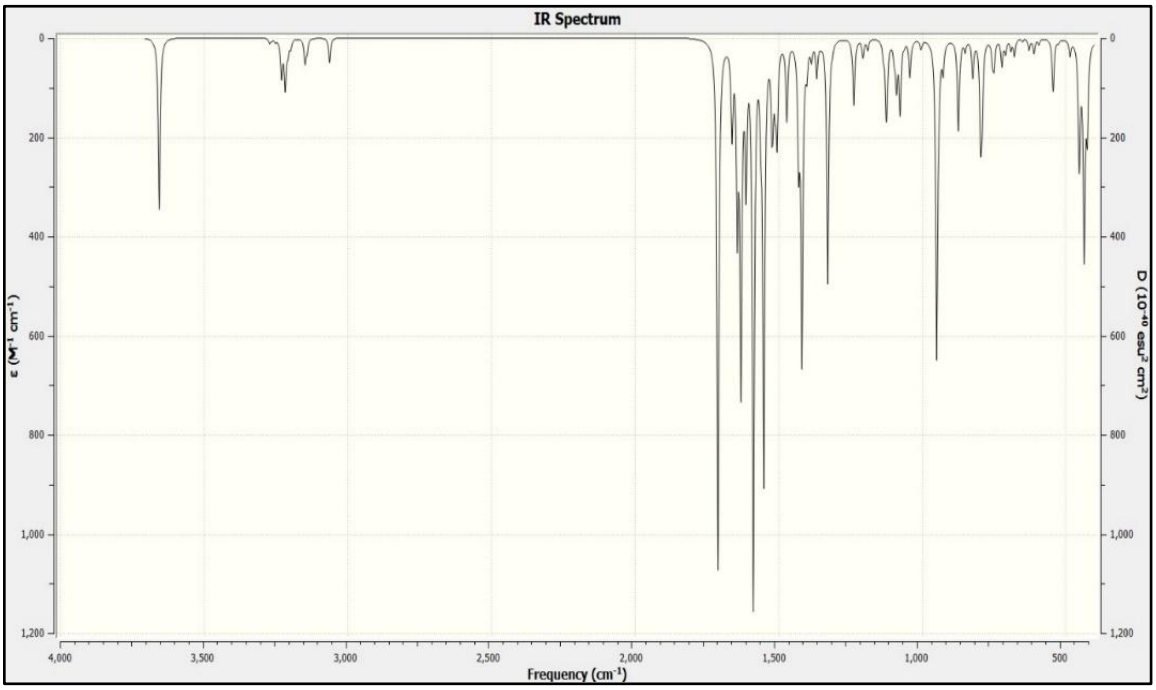

Fig.4a.18. FTIR spectrum of complex-5 through DFT computational analysis

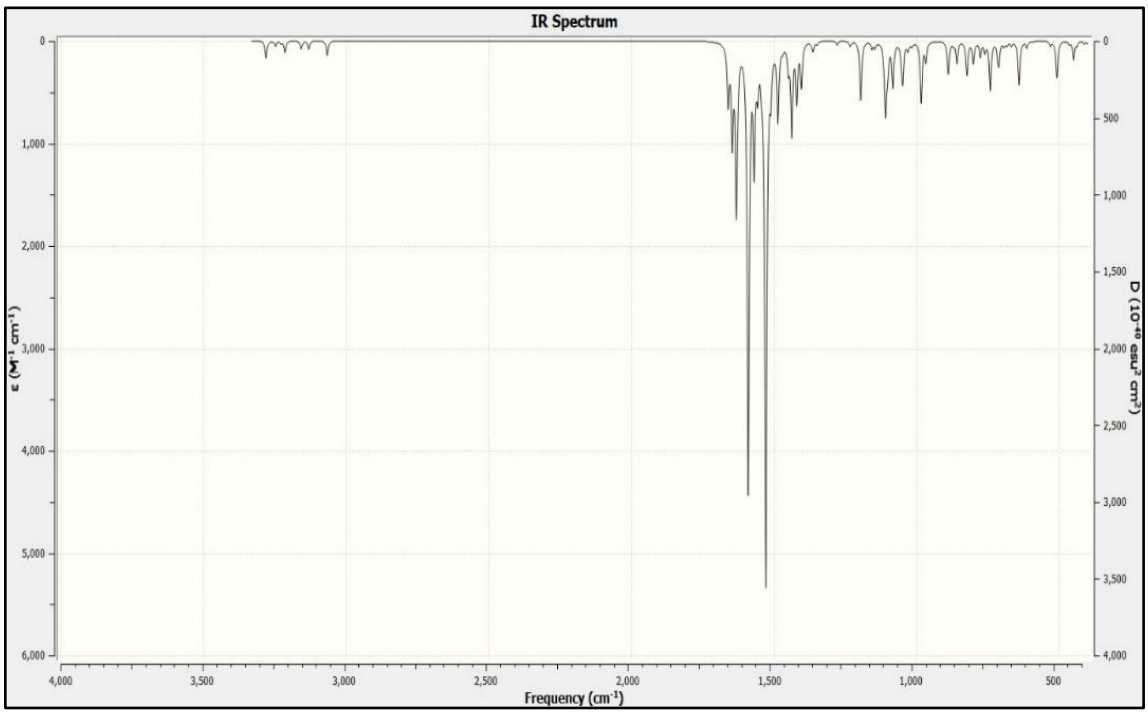

Fig.4a.19. FTIR spectrum of complex-6 through DFT computational analysis

Table 4a.12. Comparison of theoretical and practical FTIR vibrational data of complex-5 and complex-6

IR Frequencies (cm^{-1})	Complex-5		Complex-6	
	TH	PR	TH	PR
ν(C=O) of benzoyl chloride	1580	1577	1589	1586
ν(C=O) of Pyrazolone	1627	1602	1609	1601
Cyclic ν(C=N)	1442	1435	1480	1475
C–H in-plane deformation	1380	1379	1370	1360
ν_{M-O}	510	508	500	490

4a.3.7.1 Molecular electrostatic potential (MESP) & Spin density

The electron density, particularly corresponding to the molecular electrostatic potential (MESP), is a crucial aspect when studying interactions such as hydrogen bonding, as well as electrophilic and nucleophilic sites and their reactivity. Using the B3LYP/6-31G level basis set, we derived the MESP of the complex to predict the reactivity of specific sites for potential attacks. The regions with the highest negative, positive, and neutral electrostatic potential (ESP) values are represented by red, blue, and green shades, respectively. The most positive region is located around the hydrogen atom attached to a carbon atom (C-H), indicating this area acts as an electron-attracting site, while the red (negative) region marks the electron-donating site in both complexes [27]. The spin density distributions are primarily delocalized on the copper atom, and the atoms are directly bonded to it. The coordinated donor atoms exhibit negative spin densities, whereas the metal centre shows positive spin densities [32][33]. The HOMO-LUMO geometries are consistent with this spin density pattern in both copper complexes. **Fig. 4a.20** shows the MESP diagram and spin density plot for complex-**5**, while **Fig.4a.21** depicts the same for complex-**6.**

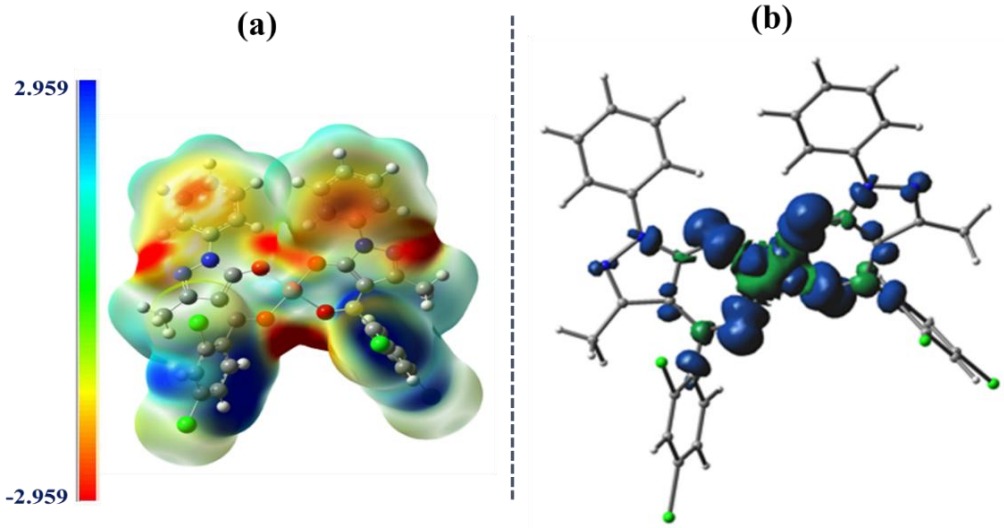

Fig.4a.20. Complex-5 : (a) MESP plot and (b) Spin density plot

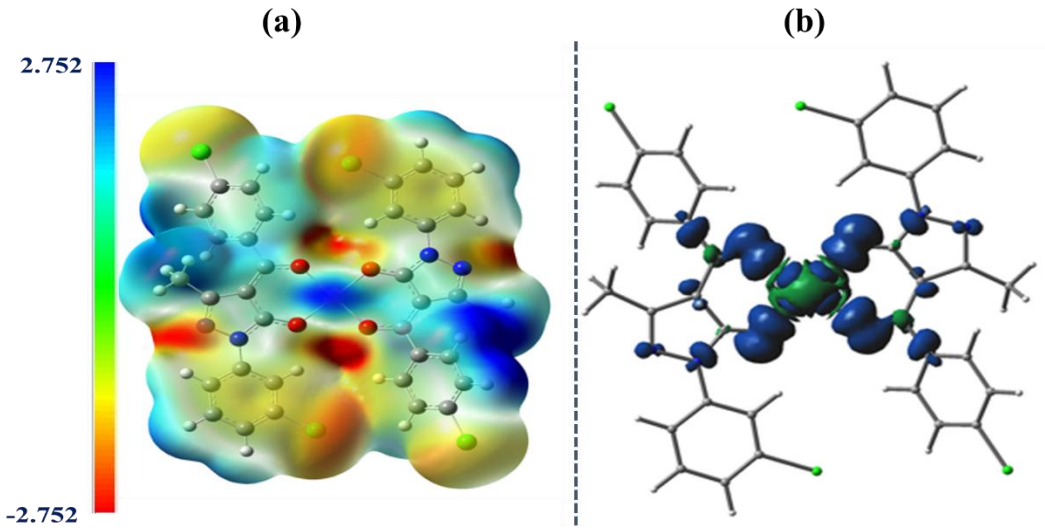

Fig.4a.21. Complex-6 : (a) MESP plot and (b) Spin density plot

4a.3.7.2 Natural bond orbital (NBO) analysis

Through NBO analysis, it is possible to measure the delocalization of electron density between occupied Lewis-type NBOs (donors) and unoccupied non-Lewis-type NBOs (acceptors/Rydberg), which is related to stabilizing donor-acceptor interactions. The B3LYP/6-31G level basis set was used to perform the corresponding complexes' natural bond orbital (NBO) analysis [11]. The interactions between the Cu(II) ion and donor atoms are considered coordination bonds between the Cu(II) ion and the oxygen atoms. This interaction involves the donation of electron density from the lone pair orbital of the donor atom (LP(O)) of the acylpyrazolone ligand to the antibonding orbital of LP*(Cu). In complexes **5** and **6**, the natural atomic charges on Cu^{2+} are +1.1676 and +1.1731, respectively. The charges on the oxygen atoms are as follows: O5 = -0.706, O6 = -0.660, O7 = -0.704, and O8 = -0.660 in complex-**5**; and O4 = -0.710, O5 = -0.671, O38 = -0.710 and O39 = -0.671 in complex-**6**. Copper has the following natural electronic configurations: [core] 3d(9.13) 4s(0.34) 4p(0.35) for complex-**5**, and [core] 3d(9.13) 4s(0.37) 4p(0.32) for complex-**6**. The core electrons number is 17.9971, with 9.8232 valence electrons (in 4s, 3d, and 4p atomic orbitals) and 0.0120 Rydberg electrons (in 4p, 4d, and 5p orbitals), totalling 27.8323 electrons and the natural atomic charge of copper is +1.1676 for complex-**5**, reflecting the difference between the total of 27.8323 electrons and the 29 electrons of an isolated copper atom. For complex-**6**, the values are 17.9970 core electrons, 9.8190 valence electrons, and 0.0108 Rydberg electrons, totalling 27.8268 electrons, with a natural atomic charge of +1.1731, showing the difference from the 29 electrons of an isolated copper atom. Although the copper ion has a +2 charge before complexation [34], ligand-to-metal charge

transfer (LMCT) leads to an electronic cloud in the antibonding orbitals of the Cu^{2+} ion in both complexes. **Fig.4a.22** illustrates the DFT-optimized geometry based on NBO analysis

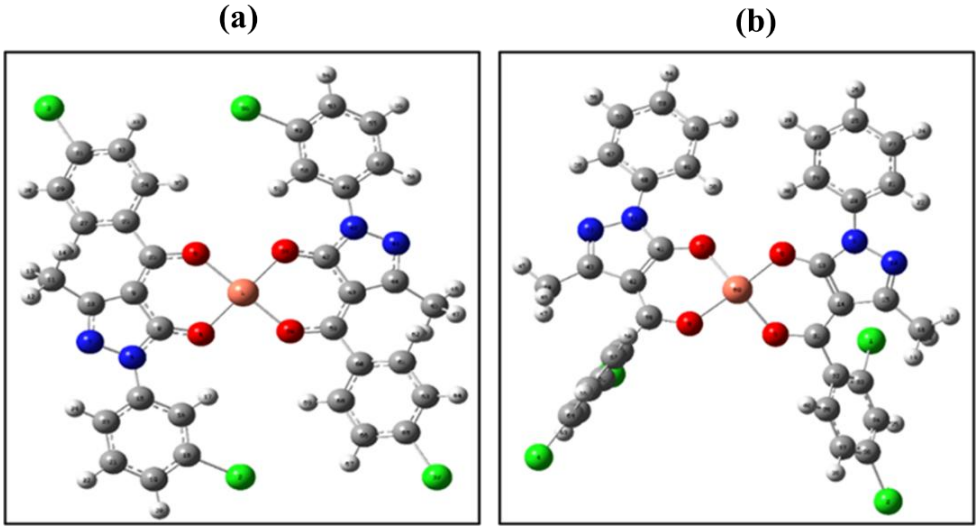

Fig.4a.22. DFT optimized geometry of (a) complex-5 (b) complex-6 based on NBO analysis

4a.3.8 Hirshfeld surface area analysis

To better understand how molecules interact in crystal structures, we employed Hirshfeld surface area analysis for complex-**5** and complex-**6**. This analysis provides a detailed description of the molecule's immediate surroundings. Using the CrystalExplorer 17.5 program, donor-acceptor interaction sites and intermolecular contacts were visualized [35]. The 3D Hirshfeld surfaces were mapped over dnorm, de, di, shape index, curvedness, and fragment patches for both complexes **5** and **6**. In the copper complexes, coordination with the Cu(II) ion is favoured through interactions with four oxygen atoms from two acylpyrazolone ligands. The molecular moieties around which these surfaces were computed can be visualized through transparent surfaces. The red intense spots on the dnorm hirshfeld surface indicate close-contact interactions, representing strong hydrogen bonding [36]. More intramolecular interactions or closeness to the nearby neighbouring molecule are indicated by the red portion. The red and blue patches on the surface show the π … π stacking interaction. Such regions plotted over the shape index suggested that not only intramolecular interactions but also stacking interactions played a crucial role in stabilising crystal packing. The absence of red spots indicates that the compound doesn't contain many significant longer hydrogen bonds. The concave areas of the yellowish-orange triangles in the shape index correspond to the atoms in the π···π stacked molecule. It is particularly sensitive to even the smallest variations in surface form. The stacking and shorter non-covalent interaction than Vander-Waals indicated by the red-blue triangles help to stabilise the crystal framework. In

HS analysis curvedness is a function of rms (root mean square) curvature which suggests that the surface has a flat area and sharp surfaces denoting low and high curvedness, respectively. The interaction is further supported by the di (distance internal to the surface) and de (distance external to the surface) plots. With the help of 2D fingerprint plots, non-covalent interactions contributing to the stabilisation of crystal packing may be quantitatively investigated. In a fingerprint plot, the colour gradient typically reflects the density of interaction points. Cooler colours, such as blue and grey, indicate regions with weaker or less frequent interactions. The packing probability of molecules is also demonstrated by the interaction of one atom inside a molecule with all the atoms of its neighbours in the compound [28]. The molecular Hirshfeld diagrams of both complexes **5** and **6** are depicted in **Fig.4a.23.** Two-dimension fingerprint plots of all such interactions of complex-**5** and complex-**6** are shown in **Fig.4a.24.**

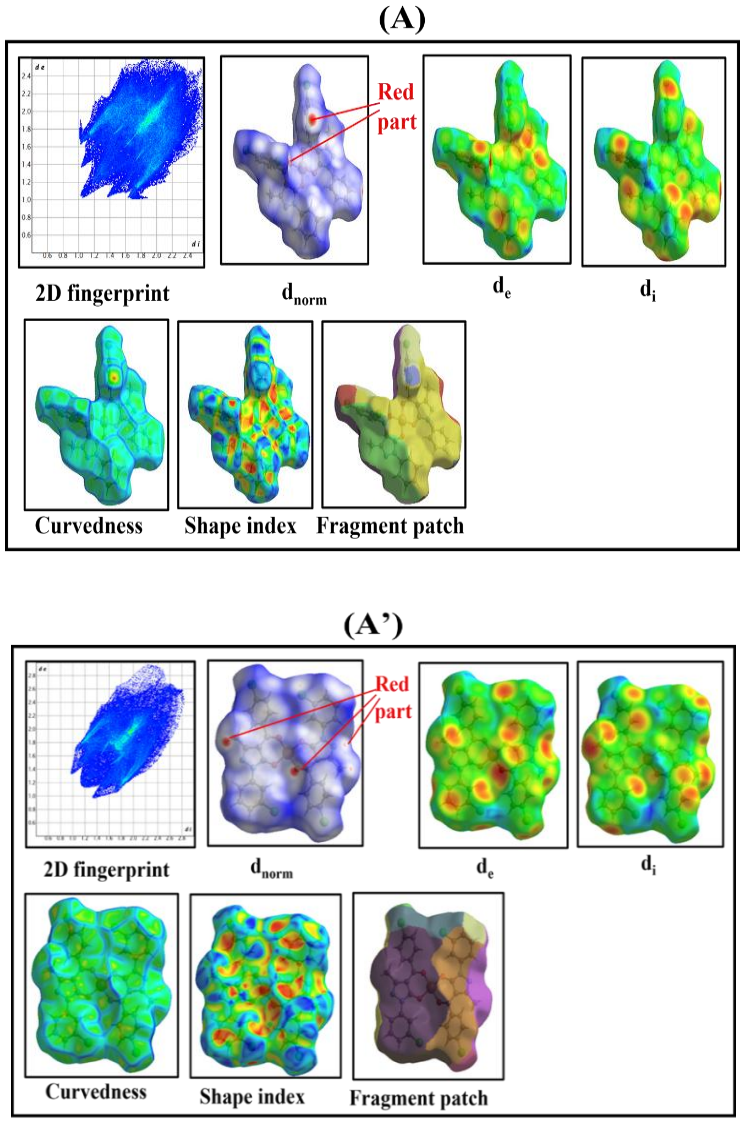

Fig.4a.23. The molecular Hirshfield (full FP diagram, dnorm, di, de, Curvedness, Shape index, and fragment patch) (A) complex-5 and (A') complex-6

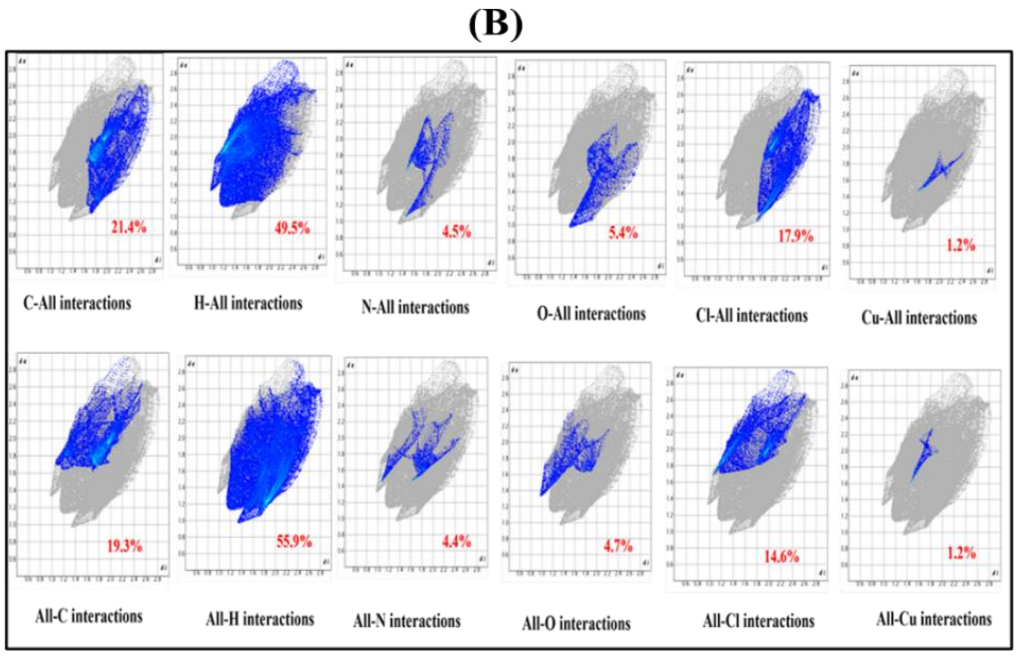

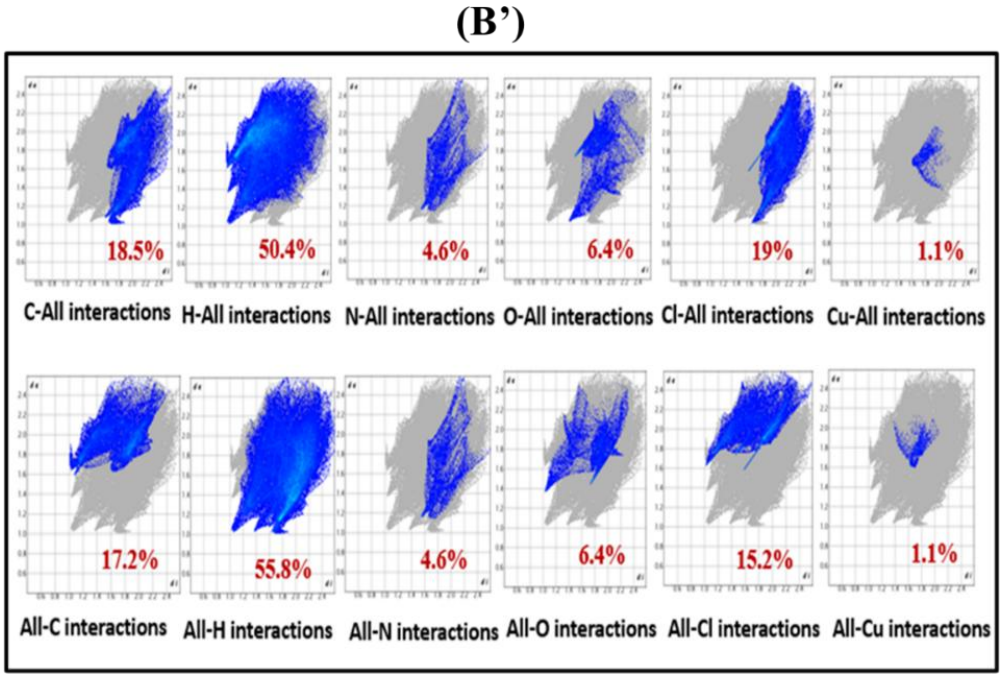

Fig.4a.24. Two-dimensional fingerprint plots of (B) complex-5 and (B') complex-6

The packing efficiency of the compound can be evaluated by calculating the interaction percentages between both all atoms and specific atom types. By studying these surfaces, one can gain crucial information about the strength and nature of interactions within the crystal structure. There is an absence or very few secondary interactions between copper metal and neighbouring atoms of surrounded molecules due to the 1% or less than 1% interactions in all-Cu/Cu-all in both complexes. Significant interaction is present among the H atom(inside) and all other atoms in complex-**5** and complex-**6;** for example, H-all interaction is 50% in both complexes [37]. Other interactions of O, N, Cl, etc, with all atoms

and vice versa for complex-**5** and complex-**6** are shown in **Fig.4a.25** and **Fig.4a.26,** respectively.

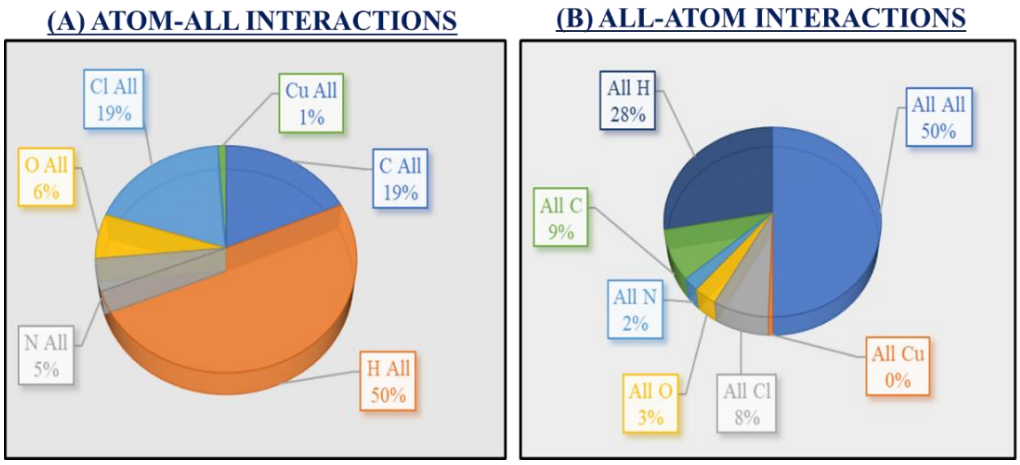

Fig.4a.25. Graphical presentation of percentage interactions between each inside and outside atom of complex-5

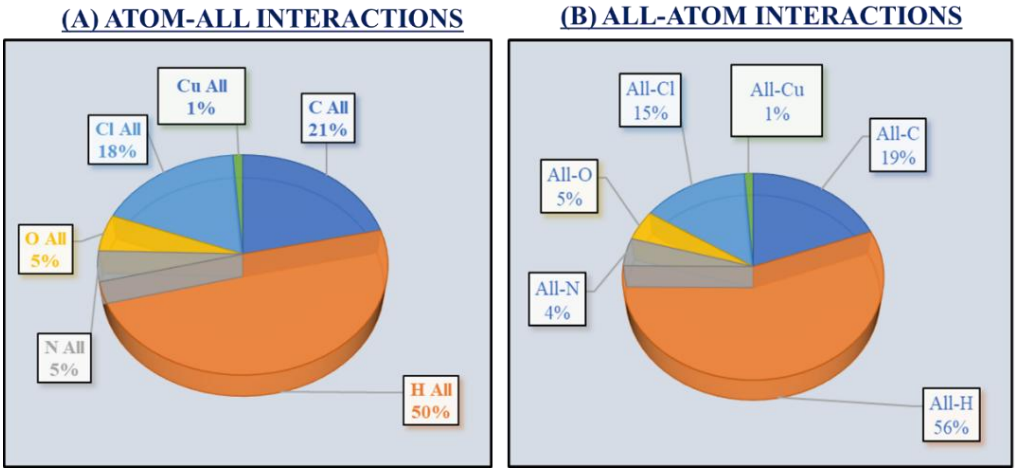

Fig.4a.26. Graphical presentation of percentage interactions between each inside and outside atom of complex-6

4a.3.9 ESR analysis (magnetic behaviour)

The ESR spectral analysis of two copper complexes was carried out using ESR JEOL analysis in powder state at room temperature (RT) and in solution state at liquid nitrogen temperature (LNT), with tetracyanoethylene (TCNE) as a marker (g = 2.00277) to determine the geometry of the copper complexes. Cu(II) exhibits four lines, as seen in the graph. The $|g|^a$ and $|A|^a$ represent the average values of g and A, respectively and can be calculated using the formulas $|g|^a=1/3\ (g_{||}+2g_{\perp})$ and $|A|^a=1/3\ (A_{||}+2A_{\perp})$, respectively [38][39]. All the ESR data are summarized in the tables below. The X-band ESR spectra of complex-**5** and complex-**6** are provided in **Figs.4a.27-28,** respectively. Similarly, the spectral data for both complexes are shown in **Table 4a.13.**

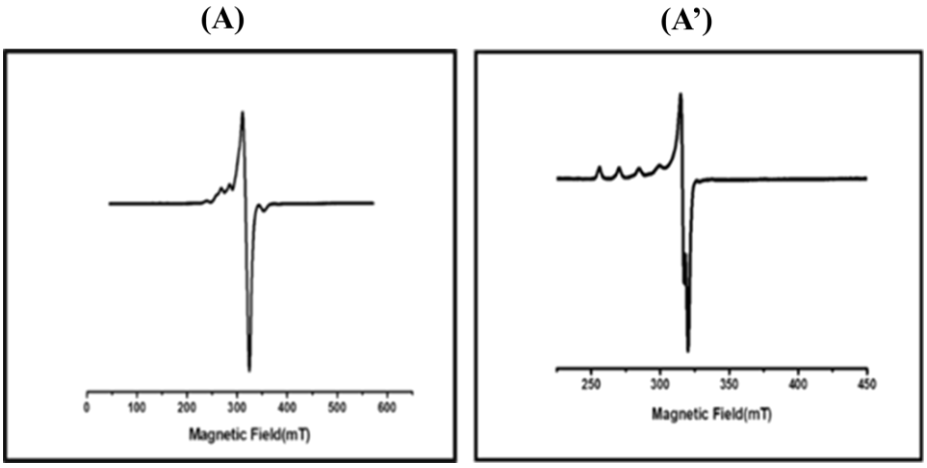

Fig.4a.27. X-band ESR spectra of complex-5 in (A) solid state at RT (A') solution state at LNT

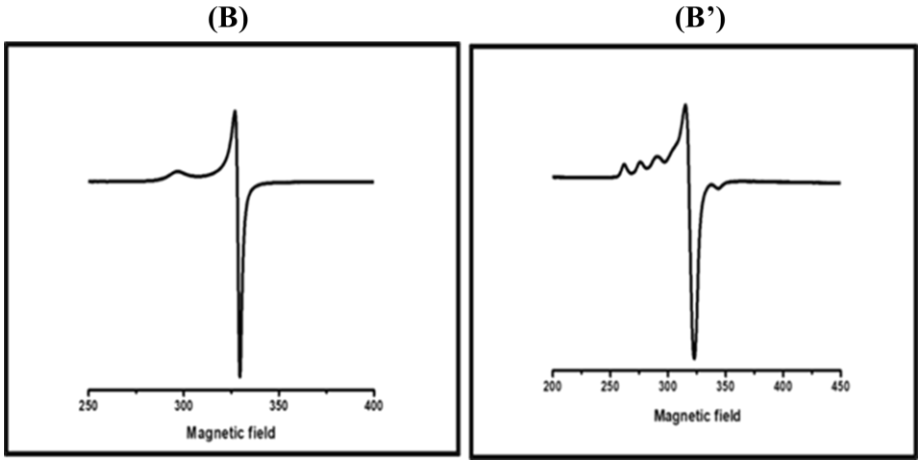

Fig.4a.28. X-band ESR spectra of complex-6 in (A) solid state at RT (A') solution state at LNT

Table 4a.13. ESR spectral data of complex-5 and complex-6

Complex-5			Complex-6		
	RT	LNT		RT	LNT
$g_{\|\|}$	2.370	2.370	$g_{\|\|}$	2.204	2.313
$g_{\perp}$	2.065	2.063	$g_{\perp}$	2.000	2.052
$\|g\|^{a}$	2.116	2.165	$\|g\|^{a}$	2.068	2.139
$A_{\|\|}$ (10^{-4} cm^{-1})	-	166	$A_{\|\|}$ (10^{-4} cm^{-1})	-	151
$A_{\perp}$ (10^{-4} cm^{-1})	-	29	$A_{\perp}$ (10^{-4} cm^{-1})	-	76

4a.3.10 Electro-chemical analysis (CV)

CV is an electrochemical technique used to study redox processes by measuring current response to a cyclically varying applied voltage. The redox behaviour of complex-**5** and complex-**6** was studied through cyclic voltammetry (CV) technique. The diagram shows

two oxidation and reduction peaks. An anodic oxidation peak Epa(I) = -0.6441 V ($Cu^{0+} \rightarrow Cu^{+1}$) and Epa(II) = 1.3991 V($Cu^{1+} \rightarrow Cu^{+2}$) observed and reduction peak Epc(I) = -1.0977 V ($Cu^{2+} \rightarrow Cu^{+1}$) and Epc(II) = -0.3303 V ($Cu^{1+} \rightarrow Cu^{+0}$) observed for complex-**5**. While for complex-**6,** Epa(I) = -0.6597 V ($Cu^{0+} \rightarrow Cu^{+1}$), Epa(II) = 1.4266 V($Cu^{1+} \rightarrow Cu^{+2}$) and reduction peak Epc(I) = -1.2044 V ($Cu^{2+} \rightarrow Cu^{+1}$), Epc(II) = -0.2768 V ($Cu^{1+} \rightarrow Cu^{+0}$) observed. The values of ΔEp_1 are 0.4536 V and 1.8641 V for complexes-**5** and **6**, respectively, while ΔEp_2 for complex-**5** is 1.7294 V and for complex-**6** is 0.2768 V for each redox couple. It increases as the scan rate does, which demonstrates the quasi-reversible character of the graphs [40][41]. The ratio of the first anodic to cathodic peak current (Ipa_1/Ipc_1) for complex-**5** is -0.0046 amp, and for the second peak (Ipa_2/Ipc_2) is -2.4671 amp. For complex-**6,** the (Ipa_1/Ipc_1) ratio is -0.0047 amp and (Ipa_2/Ipc_2) ratio is -2.1788 amp. All data for both complexes are shown in the diagram below. The CV curves for complex-**5** and complex-**6** are displayed in **Fig.4a.29.**

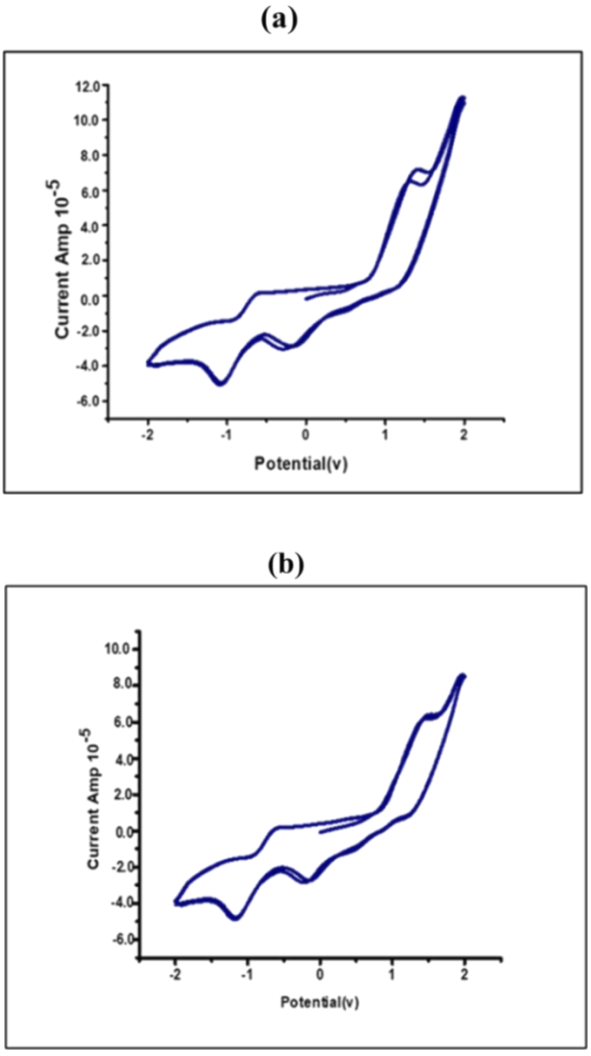

Fig.4a.29. Cyclic voltammogram of (a) complex-5 and (b) complex-6 in DMSO solution using 0.1 M TBAP at Scan rate 100 mV

4a.3.11 *In vitro* Anticancer activity

The anticancer efficacy of the complexes was evaluated using a cytotoxicity assay, which demonstrated a significant amount of cytotoxic activity [42]. Both copper complexes were tested against three different cancer cell lines: NCI-H23 (lung cancer), HePG2 (liver cancer), and SH-SY5Y (neuroblastoma), and the inhibition concentration (IC_{50}) value was determined for each. Cisplatin was also evaluated against the SH-SY5Y (neuroblastoma) cell line. The IC_{50} value represents the concentration at which 50% inhibition of cell growth occurs. After 24 hr of exposure, it was found that the compounds used in this study exhibited profound cytotoxic effects.

4a.3.11.1 Cytotoxicity assay

Cell viability was assessed using the MTT assay. The copper complexes effectively inhibited the cell viability of NCI-H23, SH-SY5Y, and HepG2 cancer cells. The IC_{50} value for complex-**6** was reported as 8.4 µM for both NCI-H23 and SH-SY5Y cells and 10.7 µM for HepG2 cells. In contrast, the IC_{50} values for complex-**5** were 7.2 µM, 12.3 µM, and 9.0 µM for NCI-H23, SH-SY5Y, and HepG2 cells, respectively. This study primarily focused on SH-SY5Y (neuroblastoma) cancer cells, which are among the most frequently observed solid tumours in children. Neuroblastoma has distinctive features, including a tendency for spontaneous regression in newborns and a high frequency of metastatic disease at diagnosis in individuals older than one year [43][4]. Cisplatin, a commonly used chemotherapeutic drug for treating various cancers, was also tested against the SH-SY5Y neuroblastoma cell line. The IC_{50} value for cisplatin was 44.94 µM, significantly higher than that of complex-**6**. In the comparison between complex-**5** and complex-**6** on the SH-SY5Y cell line, complex-**6** was found to be more effective due to its lower IC_{50} value (8.4 µM). These results suggest that the copper complex-**6** is more effective than cisplatin. Due to the greater effectivity of complex-**6,** it has been further studied. Live-dead assay and gene expression study have been performed using complex-**6**. The explanations are given in the following sections. **Fig.4a.30** and **Fig.4a.31** show the percent viability of three different cancer cells exposed to complex-**5** and complex-**6,** respectively. **Fig.4a.32** compares the percent cell viability of SH-SY5Y cells exposed to complex-**6** and cisplatin. **Table 4a.14** shows the percent inhibition value of complex-**5** and complex-**6** against all three cancer cell lines. **Table 4a.15** shows a comparison of Ic_{50} values of complex-**6** and cisplatin on SH-SY5Y cancer cells.

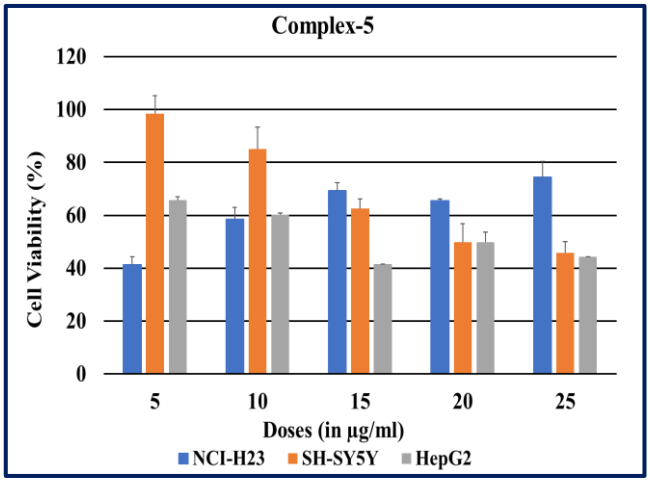

Fig.4a.30. Percent cell viability of NCI-H23, SH-SY5Y and HepG2 Cells exposed to indicated doses of complex-5

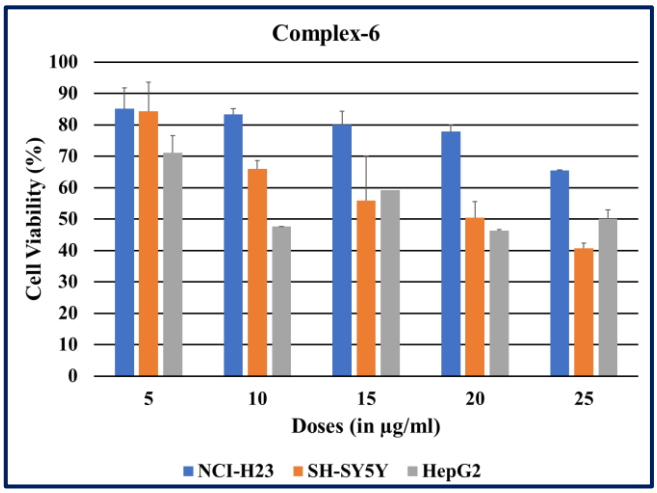

Fig.4a.31. Percent cell viability of NCI-H23, SH-SY5Y and HepG2 Cells exposed to indicated doses of complex-6

Table 4a.14. Percent inhibition (IC_{50} values) of complex-5 and complex-6 against NCI-H23, SH-SY5Y and HepG2 Cells

Percent inhibition (IC_{50} values)		
Compounds	**Complex-5**	**Complex-6**
SH-SY5Y	12.3 µM	8.4 µM
NCI-H23	7.2 µM	8.4 µM
HepG2	9.0 µM	10.7 µM

Table 4a.15. A comparison of Ic_{50} values of complex-6 and cisplatin on SH-SY5Y cancer cells

Percent inhibition (IC_{50} values)		
	Complex-6	**Cisplatin**
SH-SY5Y	8.4 µM	44.9 µM

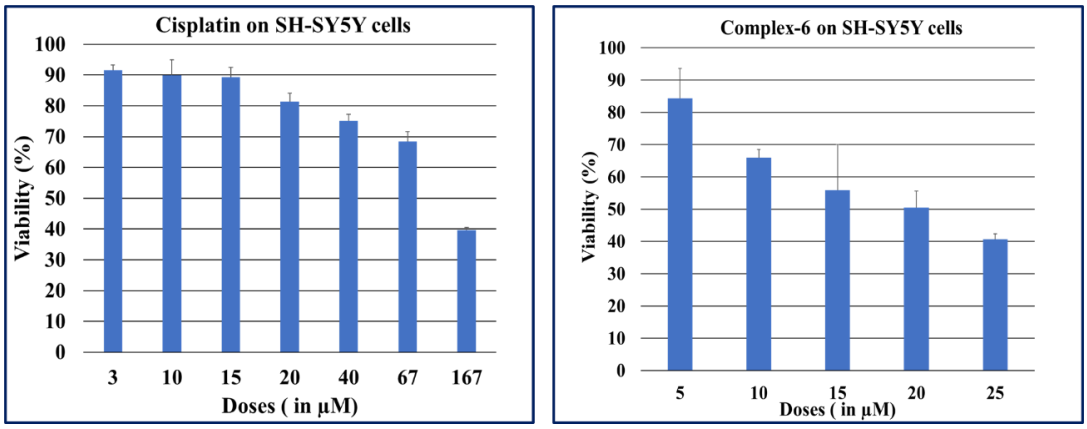

Fig.4a.32. A comparison of % cell viability on SH-SY5Y exposed to complex-6 and cisplatin

4a.3.11.2 Cell death analysis

The Live/Dead assay provides insight into the number of apoptotic dead cells and live cells. In this assay, calcein dye generates green fluorescence, indicating live cells, while Ethidium homodimer-1 (EthD-1) produces red fluorescence, marking dead cells. A significant increase in cell death is evident through the predominant red fluorescence. In contrast, negligible cell death is observed in the control medium (untreated condition), demonstrating the enhanced effectiveness of complex-**6** in inducing cell mortality in SH-SY5Y cells [44]**. Fig.4a.33** shows the dual staining of SH-SY5Y cells after 24 hours of exposure to complex-**6**, while **Fig.4a.34** illustrates the percentage of apoptotic dead cells.

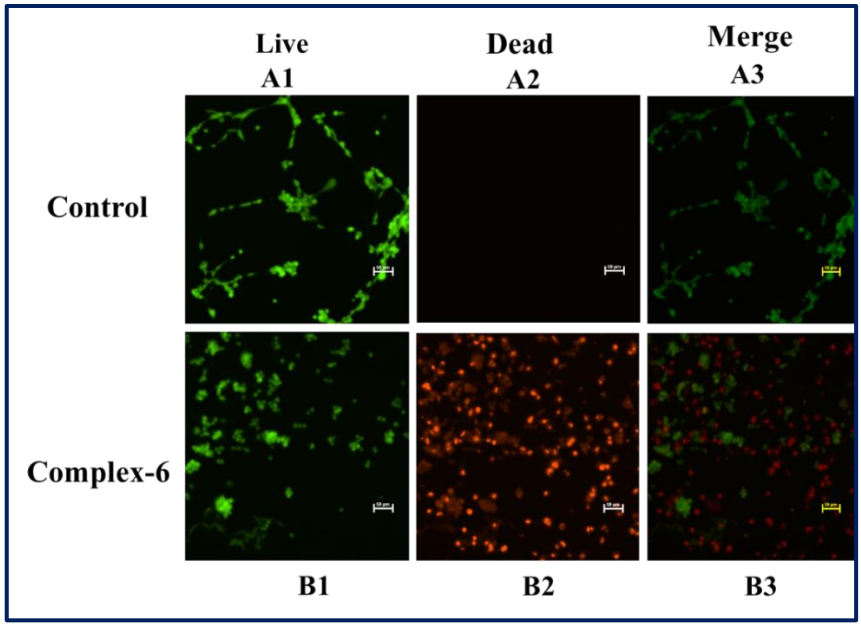

Fig.4a.33. Dual staining of SH-SY5Y cells exposed to complex-6 for 24h
(A1&A2) = Untreated cells stained by Calcein and EthD-1 dyes, respectively
(B1&B2) = Treated cells stained by Calcein and EthD-1 dyes, respectively

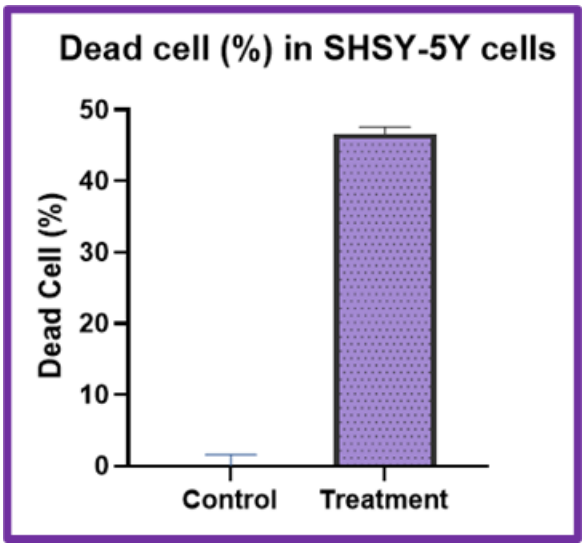

Fig.4a.34. Percentage of dead cells in SH-SY5Y cells exposed to complex-6, calculated by ImageJ Analysis

4a.3.11.3 Gene expression study by qRT-PCR

Gene expression refers to the process by which the information encoded in a gene is utilized to produce a functional product, such as a protein. A common and trusted method for studying gene expression is real-time polymerase chain reaction (PCR), which allows for precise measurement of gene expression levels. In these studies, researchers often assess how the expression of specific genes changes, whether it increases or decreases, by quantifying the amount of the gene's transcript. This approach is particularly useful when observing how a gene reacts to a particular treatment, drug, or environmental condition. Gene expression analysis can also involve examining patterns across multiple genes to understand their collective behaviour. Whether the goal is to quantify individual gene expression changes or to analyze broader expression profiles, real-time PCR remains a widely used technique among scientists for this purpose [45].

In this method, SH-SY5Y neuroblastoma cancer cells were cultured in a 6-well sterile culture plate. After 24hr, cells were treated with synthesized complex-**6** for 24hr. Cells were collected in TRIzol reagent and RNA was isolated. The quality and quantity of RNA was assessed by nanodrop. RNA was converted into cDNA using a **High-Capacity cDNA Reverse Transcription kit**. SYBR green dye was used to detect the fluorescence by using a 12k flex Real-time PCR machine. GAPDH was used as an internal control. In this study, we have selected the BCL2L1 gene and BAD gene. Both these genes belong to the Bcl-2 family. The Bcl-2 family consists of both pro-apoptotic and anti-apoptotic members, all of which share Bcl-2 homology (BH) domains [46]. The BCL2L1 gene and BAD gene are considered antiapoptotic and pro-apoptotic genes, respectively. These two genes have

opposing functions in controlling cell death and survival. The BCL2L1 gene promotes survival, while BAD induces apoptosis. Maintaining the balance between these proteins is essential for normal tissue homeostasis and preventing diseases such as cancer.

The antiapoptotic gene, BCL2L1, is significantly downregulated (60%), and the pro-apoptotic gene BAD is significantly upregulated (2.7-fold). BAD and BCL2L1 gene expression was checked using the $2^{-\Delta\Delta CT}$ method. In this study, a complex-**6** targets the anti-apoptotic BCL2L1 gene and induces apoptosis using bioinformatics tools. The objective was to reduce the expression of BCL2L1. The BCL2L1 anti-apoptotic gene was identified as a target based on information from the KEGG database [47]. This indicates that complex-**6** could significantly induce apoptosis against SH-SY5Y cancer cells. **Fig.4a.35** represents the gene expression of two different genes in control and treated conditions. In conclusion, the findings of this study demonstrate that complex-**6** significantly reduces BCL2L1 expression in SH-SY5Y cell lines, leading to apoptosis. Therefore, the overexpression of complex-**6** may serve as a potential therapeutic approach when combined with radio and chemotherapy for the treatment of neuroblastoma. Gene therapy holds significant promise, particularly when used alongside other therapeutic strategies. However, further research and development are essential to establish it as a dependable treatment option [46]. The set of primers used for the gene expression study are listed in **Table 4a.16.**

Table 4a.16. List of the primers used for gene expression study

Gene	Forward Primer	Reverse Primer
BCL2L1	CATGGCAGCAGTAAAGCAAG	TAGAGTTCCACAAAAGTATC
BAD	CGGAGGATGAGTGACGAGTT	GATGTGGAGCGAAGGTCACT

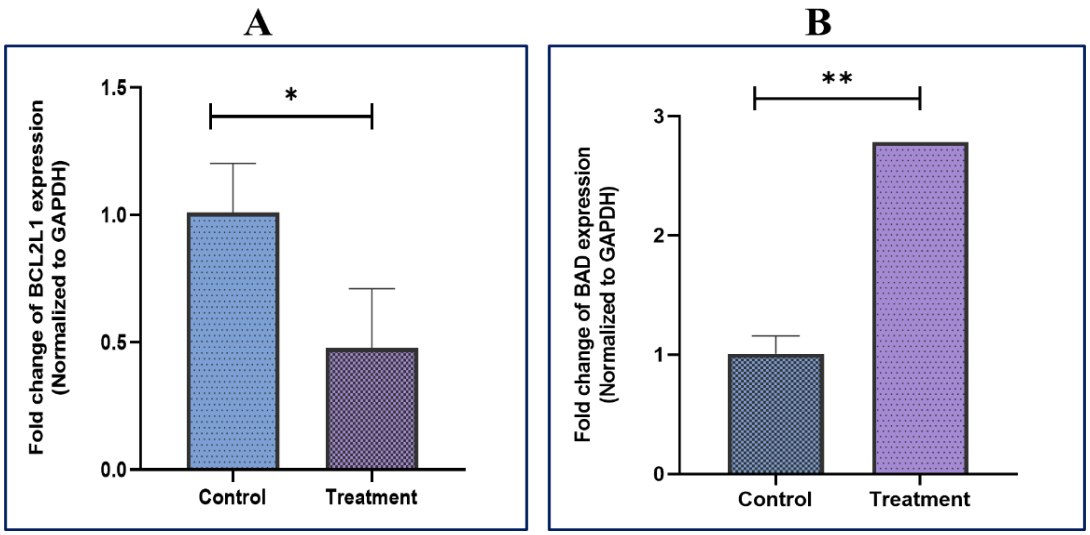

Fig.4a.35. Gene expression of the (A) BCL2L1 gene, (B) BAD gene in control and treated condition

4a.4 Conclusion

Two Cu(II) complexes, derived from heterocyclic acyl pyrazolone ligands, have been synthesized and characterized. X-ray crystallography analysis confirmed a square planar geometry around the copper centre in both complexes. The crystallographic data also revealed that four oxygen atoms from the ligands coordinate with the central copper metal at equatorial positions. Various analytical techniques were employed to further characterize the complexes, both of which were found to be stable at room temperature. The complexes were optimized using the DFT/B3LYP/6-31G approach. The HOMO-LUMO energy, NBO analysis, and ESP analysis were conducted using the same basis set. The bond lengths and bond angles between the ligands and complexes aligned well with experimental results. HOMO-LUMO analysis helped assess the complexes' kinetic stability and charge transfer characteristics. ESR study indicated the paramagnetic nature of the complexes, while cyclic voltammetry (CV) provided insights into their redox behaviour and showed the quasi-reversible nature of the graphs. *In vitro* anticancer studies showed promising results, as both copper complexes exhibited the ability to inhibit cell viability. The gene expression study indicates that complex-**6** could significantly induce apoptosis in SH-SY5Y cells. In conclusion, the findings of this study demonstrate the significance of complex-**6.** A compound significantly reduces BCL2L1 expression in SH-SY5Y cell lines, leading to apoptosis. Therefore, the overexpression of complex-**6** may serve as a potential therapeutic approach. Given these findings, further *in vivo* studies should focus on evaluating their potential use in chemotherapy to improve survival outcomes for cancer patients.

References

[1] D. Karaka, K. Sayin, DFT and TD-DFT studies on copper (II) complexes with tripodal tetramine ligands, 52 (2013) 480–485.

[2] R.K. Sodhi, Metal Complexes in Medicine: An Overview and Update from Drug Design Perspective, Cancer Ther. Oncol. Int. J. 14 (2019). https://doi.org/10.19080/ctoij.2019.14.555883.

[3] C. Molinaro, A. Martoriati, L. Pelinski, K. Cailliau, Copper Complexes as Anticancer Agents Targeting Topoisomerases I and II, Cancers. 12, (2020) 2863. https://doi.org/10.3390/cancers12102863.

[4] A. Nakagawara, Y. Li, H. Izumi, K. Muramori, H. Inada, M. Nishi, Review Article, 48 (2018) 214–241. https://doi.org/10.1093/jjco/hyx176.

[5] A. Climova, E. Pivovarova, K. Gobis, D. Ziembicka, A. Korga-plewko, J. Kubik, M. Iwan, Anticancer and antimicrobial activity of new copper (II) complexes, J. Inorg. Biochem. 240 (2023) 112108. https://doi.org/10.1016/j.jinorgbio.2022.112108.

[6] F. Marchetti, C. Pettinari, R. Pettinari, Acylpyrazolone ligands: Synthesis, structures, metal coordination chemistry and applications, Coord. Chem. Rev. 249 (2005) 2909–2945. https://doi.org/10.1016/j.ccr.2005.03.013.

[7] F. Marchetti, C. Pettinari, C. Di Nicola, A. Tombesi, R. Pettinari, Coordination chemistry of pyrazolone-based ligands and applications of their metal complexes, Coord. Chem. Rev. 401 (2019) 213069. https://doi.org/10.1016/j.ccr.2019.213069.

[8] M. Hasanzadeh Esfahani, F. Boorboor Ajdari, E.B. Poormohammadi, A. Abbasi, M. Behzad, Synthesis, crystal structure and battery-like studies on a new acylpyrazolone-based mixed-ligand Cu(II) complex, Res. Chem. Intermed. 48 (2022) 575–591. https://doi.org/10.1007/s11164-021-04605-5.

[9] F. Marchetti, R. Pettinari, C. Pettinari, Recent advances in acylpyrazolone metal complexes and their potential applications, Coord. Chem. Rev. 303 (2015) 1–31. https://doi.org/10.1016/j.ccr.2015.05.003.

[10] R.N. Jadeja, K.M. Vyas, K.K. Upadhyay, R. V. Devkar, In vitro apoptosis-inducing effect and gene expression profiles of mixed ligand Cu(II) complexes derived from 4-acyl pyrazolones on human lung cancer cells, RSC Adv. 7 (2017) 17107–17116. https://doi.org/10.1039/c7ra01025g.

[11] J.M.M. and R.C.M. PRADEEP KUMAR VISHWAKARMA, Pyrone-based Cu (II) complexes , their characterization , DFT based conformational drift from square planar to square pyramidal geometry, 128 (2016) 511–522. https://doi.org/10.1007/s12039-016-1048-6.

[12] R.C.D. G.H.Jeffery, J.Baddett, J.Mendham, Vogel's textbook of quantitative chemical analysis, n.d. https://doi.org/10.1085/jgp.25.4.523.

[13] I. Shaikh, R.N. Jadeja, R. Patel, Three mixed ligand mononuclear Zn(II) complexes of 4-acyl pyrazolones: Synthesis, characterization, crystal study and anti-malarial activity, Polyhedron. 183 (2020) 114528. https://doi.org/10.1016/j.poly.2020.114528.

[14] G.M. Sheldrick, SHELXT - Integrated space-group and crystal-structure determination, Acta Crystallogr. Sect. A Found. Crystallogr. 71 (2015) 3–8. https://doi.org/10.1107/S2053273314026370.

[15] G.M. Sheldrick, Crystal structure refinement with SHELXL, Acta Crystallogr. Sect. C Struct. Chem. 71 (2015) 3–8. https://doi.org/10.1107/S2053229614024218.

[16] D. Shoba, S. Periandy, M. Karabacak, S. Ramalingam, Vibrational spectroscopy (FT-IR and FT-Raman) investigation, and hybrid computational (HF and DFT) analysis on the structure of 2,3-naphthalenediol, Spectrochim. Acta - Part A Mol. Biomol. Spectrosc. 83 (2011) 540–552. https://doi.org/10.1016/j.saa.2011.09.002.

[17] E. Aljuhani, M.M. Aljohani, A. Alsoliemy, R. Shah, H.M. Abumelha, F.A. Saad, A. Hossan, Z.A. Al-Ahmed, A. Alharbi, N.M. El-Metwaly, Synthesis and characterization of Cu(II)-pyrazole complexes for possible anticancer agents; conformational studies as well as compatible in-silico and in-vitro assays, Heliyon. 7 (2021) e08485. https://doi.org/10.1016/j.heliyon.2021.e08485.

[18] S.P. Langdon, Cancer Cell Culture, Cancer Cell Cult. 731 (2003) 237–245. https://doi.org/10.1385/1592594069.

[19] T. Mosmann, Rapid Colorimetric Assay for Cellular Growth and Survival: Application to Proliferation and Cytotoxicity Assays, RSC Adv. 65 (1983) 55–63. https://doi.org/10.1039/c6ra17788c.

[20] F. Ponchel, C. Toomes, K. Bransfield, F.T. Leong, S.H. Douglas, S.L. Field, S.M. Bell, V. Combaret, A. Puisieux, A.J. Mighell, P.A. Robinson, C.F. Inglehearn, J.D.

Isaacs, A.F. Markham, for a Real-time PCR based SYBR-Green Iflourescence: An alternative to the TaqMan assay for a relative quantificationof gene rearrangements, gene amplifications and Micro gene deletions,{BMC} Biotechnol. 3 (2003) 18. http://www.biomedcentral.com/1472-6750/3/18.

[21] S. Parihar, S. Pathan, R.N. Jadeja, A. Patel, V.K. Gupta, Synthesis and Crystal Structure of an Oxovanadium(IV) Complex with a Pyrazolone Ligand and Its Use as a Heterogeneous Catalyst for the Oxidation of Styrene under Mild Conditions, Inorg. Chem. 51 (2012) 1152–1161. https://doi.org/10.1021/ic202396q.

[22] W.J. Geary, The use of conductivity measurements in organic solvents for the characterisation of coordination compounds, Coord. Chem. Rev. 7 (1971) 81–122. https://doi.org/10.1016/S0010-8545(00)80009-0.

[23] V. Baliram T, P. Sanjay K, P. Arvind M, Synthesis, Spectral Characterization and Antitubercular Study of Novel Quinoline Schiff Base and Its Metal Complexes, Anal. Chem. Lett. 11 (2021) 523–538. https://doi.org/10.1080/22297928.2021.1921616.

[24] S. Landron, M.B. Lepetit, Importance of t2g - Eg hybridization in transition metal oxides, Phys. Rev. B - Condens. Matter Mater. Phys. 77 (2008). https://doi.org/10.1103/PhysRevB.77.125106.

[25] Y. Nishida, K. Hayashida, A. Sumita, S. Kida, Electronic structures of square planar cobalt(II), nickel(II) and copper(II) complexes with some N4-macrocyclic ligands [1], Inorganica Chim. Acta. 31 (1978) 19–23. https://doi.org/10.1016/S0020-1693(00)94974-0.

[26] J.G. Jaiswal, S.A. Gandhi, T.J. Padariya, V.M. Barot, U.H. Patel, Synthesis and x-ray powder diffraction studies: metal complexes (co(ii), ni(ii) and cu(ii)) of schiff base ligand 4-bromo-2-chloro-6-[(1z)-n-(phenyl) ethanimidoyl] phenol, J. Pure Appl. Sci. 24 (2017) 101–105.

[27] C. Ravi, S. Kumar, Approach of Density Functional Theory to Molecules Using Gaussian, Int. J. Pure Appl. Phys. 15 (2019) 1–13. http://www.ripublication.com.

[28] M. Travadi, R.N. Jadeja, R.J. Butcher, Synthesis, covalency parameters, energy calculations and crystal features of acylpyrazolone derived pentavalent Uranyl complex along with DFT and Hirshfeld analysis, Polyhedron. 223 (2022) 1–15. https://doi.org/10.1016/j.poly.2022.115956.

[29] S.A. Alramadhan, H.H. Hammud, B.F. Ali, H.A. Ghabbour, S. Sarfaraz, K. Ayub, Structures, Characterization and DFT Studies of Four Novel Nickel Phenanthroline Complexes, Crystals. 13 (2023). https://doi.org/10.3390/cryst13050738.

[30] Y.P. Singh, R.N. Patel, Y. Singh, Crystal structure, configurational and DFT study of nickel(II) complexes with N2O-donor type Schiff base ligand, Indian J. Chem. - Sect. A Inorganic, Phys. Theor. Anal. Chem. 57A (2018) 44–51.

[31] E.B. Elkaeed, E.U. Mughal, S. Kausar, H.A. Al-ghulikah, N. Naeem, A.A. Altaf, A. Sadiq, Theoretical vibrational spectroscopy (FT-IR), PED and DFT calculations of chromones and thiochromones, J. Mol. Struct. 1270 (2022) 133972. https://doi.org/10.1016/j.molstruc.2022.133972.

[32] M.A.S. Sakr, F.F. Sherbiny, A. Allah, S. El, Hydrazone - based Materials ; DFT , TD - DFT , NBO Analysis , Fukui Function , MESP Analysis , and Solar Cell Applications, J. Fluoresc. (2022) 1857–1871. https://doi.org/10.1007/s10895-022-03000-6.

[33] M. Savarese, É. Brémond, I. Ciofini, C. Adamo, Electron Spin Densities and Density Functional Approximations: Open-Shell Polycyclic Aromatic Hydrocarbons as Case Study, J. Chem. Theory Comput. 16 (2020) 3567–3577. https://doi.org/10.1021/acs.jctc.0c00059.

[34] A.K. Patel, R.N. Jadeja, H. Roy, R.N. Patel, S.K. Patel, R.J. Butcher, M. Cortijo, S. Herrero, Copper(II) hydrazone complexes with different nuclearities and geometries: Synthesis, structural characterization, antioxidant SOD activity and antiproliferative properties, Polyhedron. 186 (2020) 114624. https://doi.org/10.1016/j.poly.2020.114624.

[35] P.R. Spackman, M.J. Turner, J.J. McKinnon, S.K. Wolff, D.J. Grimwood, D. Jayatilaka, M.A. Spackman, CrystalExplorer: A program for Hirshfeld surface analysis, visualization and quantitative analysis of molecular crystals, J. Appl. Crystallogr. 54 (2021) 1006–1011. https://doi.org/10.1107/S1600576721002910.

[36] M.A. Spackman, D. Jayatilaka, Hirshfeld surface analysis, CrystEngComm. 11 (2009) 19–32. https://doi.org/10.1039/b818330a.

[37] W. Nbili, K. Kaabi, F. Lefebvre, W. Fujita, C. Jelsch, C. ben Nasr, A Hirshfeld surface analysis, crystal structure, and physicochemical studies of a new Cu(II) complex with the 1,10-phenanthroline ligand, J. Coord. Chem. 71 (2018) 2526–2539.

https://doi.org/10.1080/00958972.2018.1489125.

[38] M. Valko, P. Pelikan, S. Biskupic, M. Mazur, ESR spectra of copper(II) complexes in the solids, Chem. Pap. 44 (1990) 805–813. https://www.chemicalpapers.com/file_access.php?file=446a805.pdf.

[39] M. Kohno, Applications of electron spin resonance spectrometry for reactive oxygen species and reactive nitrogen species research, J. Clin. Biochem. Nutr. 47 (2010) 1–11. https://doi.org/10.3164/jcbn.10-13R.

[40] A. Abayneh, T. Gebretsadik, S. Tadesse, M. Thomas, Synthesis, Spectroscopic, Structural Characterization, Conductivity and Electrochemical Studies of a Schiff Base Ligand and Its Copper Complexes, Adv. Chem. Eng. Sci. 08 (2018) 241–254. https://doi.org/10.4236/aces.2018.84017.

[41] P. Chooto, Cyclic Voltammetry and Its Applications, Voltammetry. (2019). https://doi.org/10.5772/intechopen.83451.

[42] A.K. Patel, R.N. Jadeja, H. Roy, R.N. Patel, S.K. Patel, R.J. Butcher, Pseudo-tetrahedral copper(II) complex derived from N'-[(2E,3Z)-4-hydroxy-4-phenylbut-3-en-2-ylidene]acetohydrazide: Synthesis, molecular structure, quantum chemical investigations, antioxidant and antiproliferative properties, J. Mol. Struct. 1185 (2019) 341–350. https://doi.org/10.1016/j.molstruc.2019.03.004.

[43] D.A. Cogoa, G. Liu, K. Kim, B.J. Backes, J.A. Ellman, No Title, J. Am. Chem. Soc. 120 (1998) 8011.

[44] C. Hu, S. He, Y.J. Lee, Y. He, E.M. Kong, H. Li, M.A. Anastasio, G. Popescu, Live-dead assay on unlabeled cells using phase imaging with computational specificity, Nat. Commun. 13 (2022). https://doi.org/10.1038/s41467-022-28214-x.

[45] Introduction to Gene Expression Getting Started Guide, (2010).

[46] A.H. Sillars-Hardebol, B. Carvalho, J.A.M. Beliën, M. De Wit, P.M. Delis-Van Diemen, M. Tijssen, M.A. Van De Wiel, F. Pontén, R.J.A. Fijneman, G.A. Meijer, BCL2L1 has a functional role in colorectal cancer and its protein expression is associated with chromosome 20q gain, J. Pathol. 226 (2012) 442–450. https://doi.org/10.1002/path.2983.

[47] S. Ghaemi, E. Arefian, R. Rezazadeh Valojerdi, M. Soleimani, A. Moradimotlagh, F. Jamshidi Adegani, Inhibiting the expression of anti-apoptotic genes BCL2L1 and MCL1, and apoptosis induction in glioblastoma cells by microRNA-342, Biomed. Pharmacother. 121 (2020). https://doi.org/10.1016/j.biopha.2019.109641.

Published Paper

JOURNAL OF COORDINATION CHEMISTRY
2023, VOL. 76, NOS. 16–24, 1955–1983
https://doi.org/10.1080/00958972.2023.2289004

Cytotoxicity assay and gene expression studies of acylpyrazolone-based square planar Cu(II) complexes: synthesis, characterization and computations

Sapna Barad[a], Kaushalkumar Chaudhari[b], R.N. Jadeja[a], H. Roy[b] and Ray J. Butcher[c]

[a]Department of Chemistry, Faculty of Science, The Maharaja Sayajirao University of Baroda, Vadodara, India; [b]Department of Zoology, Faculty of Science, The Maharaja Sayajirao University of Baroda, Vadodara, India; [c]Department of Inorganic & Structural Chemistry, Howard University, Washington, DC, USA

ABSTRACT

We employed a dual strategy that combines experimental and computational analyses of two copper(II) coordination complexes with σ-donating acylpyrazolone ligands. $HL^{III}B$, $[Cu(HL^{III}B)_2]$ and $[Cu(HL^{I})_2]$ have been characterized using a variety of physico-chemical methods and density functional theory (DFT) calculations using the B3LYP level of theory and 6-31 G basis set. Single crystal X-ray diffraction studies revealed monoclinic and triclinic crystal systems for $[Cu(HL^{I})_2]$ and $[Cu(HL^{III}B)_2]$, respectively, with square planar geometries for both complexes. Both complexes exhibit quasi-reversible behavior in their cyclic voltammograms in DMSO. ESR spectroscopy was performed to determine the magnetic behaviorof the two complexes. The intermolecular interactions of the complexes were further investigated using Hirshfeld surface analysis. The compounds showed promising cytotoxicities when tested against cancer cell lines of lung carcinoma, hepatocellular carcinoma, and neuroblastoma. Notable apoptotic cell death was observed with $[Cu(HL^{I})_2]$, supported by gene expression changes, indicating induction of apoptosis. The findings suggest the potential of copper complexes as effective agents against neuroblastoma and highlight their superiority to cisplatin.

ARTICLE HISTORY
Received 27 June 2023
Accepted 26 September 2023

KEYWORDS
Acylpyrazolone ligand; Hirshfeld analysis; DFT (density functional theory); gene expression; MTT assay

CONTACT R. N. Jadeja rjadeja-chem@msubaroda.ac.in
Supplemental data for this article can be accessed online at https://doi.org/10.1080/00958972.2023.2289004.

Chapter 4: Part (b)

Two new square planar Cu(II) complexes derived from a heterocyclic pyrazolone ligand: Synthesis, *in vitro* anticancer activity, DFT and Hirshfeld analysis

4b.1 Introduction

Within the biosphere, a few metals exist in their elemental form. Among these are silver, gold and copper, the first to be used in antiquity; gold and copper have been documented in historical accounts dating back at least 9000 BCE [1]. Of all the trace metals in the body, Copper (Cu) is more common than zinc and iron and is necessary for survival [2]. Copper exists in nature as Cu^{2+}, which is involved in metalloproteins such as superoxide dismutase and cytochrome oxidase, both essential to human health [3]. The coordination numbers of the copper-containing coordination complexes, which range from **four** to **six,** make them very relevant owing to the flexibility of their synthesis. Copper-based coordination complexes represent a promising group of molecules with potential applications in developing functional materials that exhibit catalytic, optical, conductive, and magnetic properties [4]. Transition metal complexes are crucial in many fields, including photochemistry, materials production, biological systems, and catalysis [5]. A huge quantity of Cu causes oxidative DNA, protein alteration, redox-sensitive gene activation, body-inhibited zinc intake, and anaemia through the inhibition of iron transport. Excessive amounts of metal ions are linked to many harmful side effects, including cancer [2].

Because of these factors, the Coordination metal complexes of copper have developed as one of the most fascinating and appealing subfields of medicinal chemistry [3]. When it comes to biological and pharmacological uses, copper metal complexes containing specific bioactive ligands may work better than those containing such ligands in their free form [6]. In this regard, the scaffolding of pyrazole derivatives is a rich reservoir of physiologically significant substances with a broad spectrum of pharmacological and biological actions because of their capacity to take electrons from nitrogen and protons from other molecules [7]. Ligand selection is becoming a crucial technique in synthesising and designing medicinal molecules [8].

Since Knorr synthesized antipyrine in 1883, the pyrazolone analogue's analgesic and antipyretic properties have sparked a lot of curiosity. The discovery of these characteristics prompted researchers to create a derivative of pyrazolone compounds that behaved similarly but had superior medicinal effects [9]**.** The pyrazolone derivative, 4-acyl-pyrazolone, with its numerous electron-rich donor centres and keto-enol tautomerism, may form a range of coordination compounds [10][11]. Analysis of many metal complexes has been done during the past thirty years, and these ligands have been employed to coordinate the majority of the metal ions as possible cancer-fighting agents [12]**.**

A breakthrough in the medical use of anticancer drugs occurred with the discovery of platinum's ability to inhibit tumour cell proliferation. However, the use of platinum compounds is restricted due to major adverse effects [13]. Because cis-platin has so many drawbacks, scientists have searched extensively for superior metal-based cancer chemotherapy drug with enhanced pharmacological characteristics [14]. Hence, copper-based drugs have recently attracted significant interest in medical research. Extensive studies have been conducted on the structure activity relationships of copper complexes with various ligands. These investigations have revealed that copper-based drugs offer a wider range of therapeutic activity and reduced toxicity compared to platinum-based medicines [15].

In this article, we are focusing on neuroblastoma cancer. A primary cause of cancer-related mortality in children is neuroblastoma, a tumour originating from the neural crest that affects the peripheral nervous system. Neuroblastoma is an embryonal tumour. The survival rate for children with neuroblastoma at high risk remains inadequate even with the establishment of risk-based, intensive, multimodal treatment. So, it is essential to find new therapeutic alternatives to provide an effective treatment for children with neuroblastoma that will increase survival, reduce side effects, and, ultimately, enhance their quality of life.

For this purpose, we have synthesized two new square planar Cu(II) complexes based on heterocyclic acylpyrazolone ligand. In this study, we have described the experimental characterization of the synthesized compounds and examined their pharmacological activity. The pharmacological action was investigated using three different cancerous cell lines: NCI-H23 (lung carcinoma-Lung cancer), SH-SY5Y (neuroblastoma cancer) and HepG2 (hepatocellular carcinoma cell line-Liver cancer). Additionally, a comprehensive theoretical analysis is also conducted. Density Functional Theory (DFT) is a valuable modelling technique and an effective method for exploring various properties, including those relevant to biological studies [16]**.** A molecular Hirshfeld surface analysis has been developed to gain deeper insights into how molecular components interact with their surrounding environment. This technique allows for the visualization and quantification of nonbonded interactions that are not easily discernible through conventional structural analysis. It also enables the comparison of intermolecular interactions and provides quantitative information on the relative strengths of these interactions in crystal packing [17].

4b.2 Experimental Section

4b.2.1 Materials and Methods

All copper salts, AR-grade solvents, acyl chloride, pyrazolone material, all the required chemicals and cancer cell lines were procured from the same sources described in Chapters **2, 3** and **4** (part **a**). The synthesis and characterization of the ligands HL^{VII} and HL^{VIII} were performed following the procedures outlined in Chapter **2**. Both these ligands were synthesized, characterized and published in our laboratory's recent publication [18][19].

4b.2.2 Synthetic route of complex-7 and complex-8

Both complex-**7** and complex-**8** were synthesized using a general method, as explained in Chapters **3** and **4a.** The synthetic routes for complexes-7 and complex-**8** are shown in **Fig.4b.1.** The physical characteristics of both copper complexes are depicted in **Fig.4b.2.**

HL^{VII} ligand (0.681g, 0.002 mol), HL^{VIII} ligand (0.640 g, 0.002 mol), $CuSO_4.5H_2O$ (0.001 mol,0.249 g).

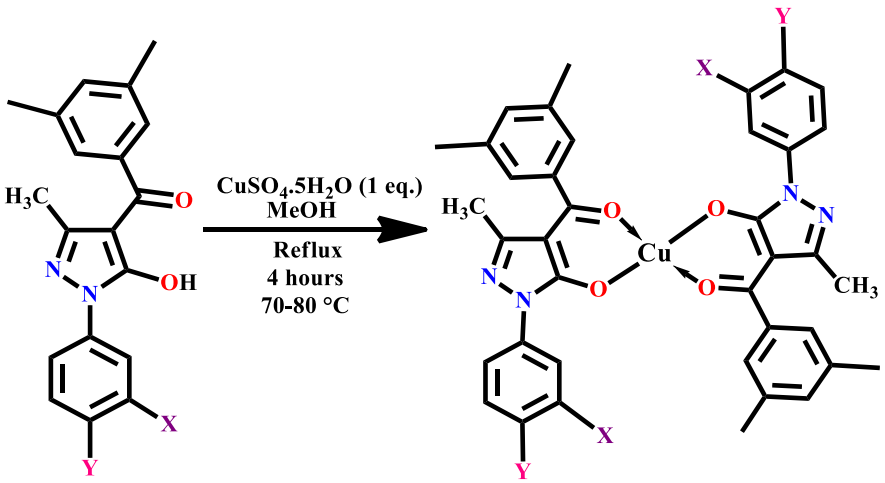

Complex-7: X= Cl, Y= H

Complex-8: X = H, Y= CH_3

Fig.4b.1. Synthetic route of complex-7 and complex-8

Complex-7: **Colour**: Green, yield: 82%, M.P:> 200°C, Molecular formula: $C_{38}H_{32}CuCl_2N_4O_4$, **Crystal:** Pale green-yellow thick needle, M.W: 743.14, **Elemental analysis**: C (Exp. 60.97%, Calc.: 61.42%); H (Exp. 4.86%, Calc. 4.34%); N (Exp. 8.23%, Calc. 7.54%); Cu (Exp. 8.30%, Calc. 8.55%), **Molar conductance (10^{-3} M DMF):** 4.0 ohm^{-}

$^{1}cm^{2}mol^{-1}$. **FTIR (KBr, cm^{-1}):** ν(C=O) of pyrazolone (1603), ν(C=O) of 3,5-dimethyl benzoyl (1585), ν(C=N) 1529.

Complex-8: **Colour**: Yellowish green, yield: 80 %, M.P: >200°C, Molecular formula: $C_{40}H_{38}CuN_4O_4$, **Crystal:** thick plates, M.W: 702.30, **Elemental analysis**: C (Exp. 67.95%, Calc.: 68.41%); H (Exp. 4.98%, Calc. 5.45%); N (Exp. 6.90%, Calc. 7.98%); Cu (Exp. 8.80%, Calc. 9.05%), **Molar conductance (10^{-3} M DMF):** 4.5 $ohm^{-1}cm^{2}mol^{-1}$. **FTIR (KBr, cm^{-1}):** ν(C=O) of pyrazolone (1593), ν(C=O) of 3,5-dimethyl benzoyl (1526),ν(C=N) 1492.

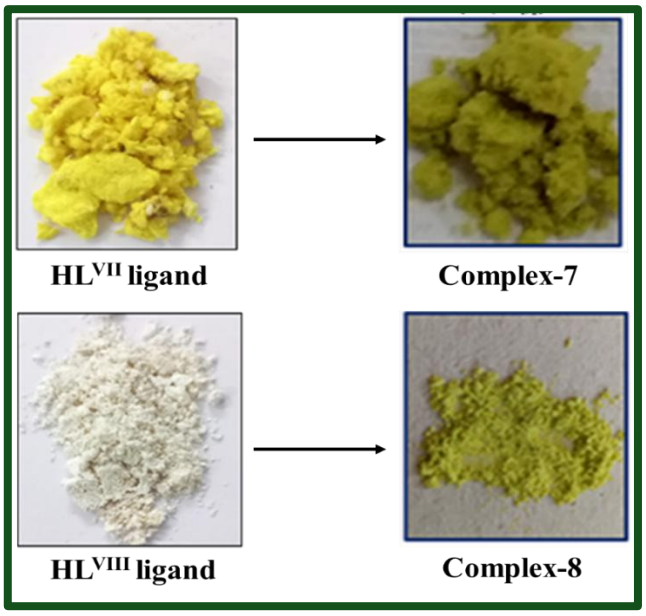

Fig.4b.2. Physical appearance of respective ligands, complex-7 and complex-8

4b.2.3 Study of X-ray crystallography

Both complexes were synthesized in hot MeOH, and X-ray quality single crystals of complexes **7** and **8** were obtained using a DMF solvent. X-ray diffraction data were recorded at 298(2) K using a Bruker APEX-II CCD diffractometer with Cu—Kα radiation (λ = 1.54178 Å) and a graphite monochromator. The diffraction data were analyzed using the SHELXT programme for structure solution [20]. Refinement was performed through full-matrix least squares methods based on F^2 with the SHELXL-2018/3 program [21]. A micro-focus sealed X-ray tube served as the diffraction source. All non-hydrogen atoms were found in their anticipated positions within the structures. The ORTEP representations of the complexes were generated using Mercury software [22].

4b.2.4 Physical measurements and Characterization

Various analytical and spectroscopic techniques were employed to characterize the synthesized complexes, such as FTIR, UV-Vis, ESR, TGA, Molar conductance, and Elemental analysis. The magnetic property was examined through ESR JEOL analysis at liquid nitrogen temperature with tetracyanoethylene (TCNE) as a marker (g = 2.00277) at SAIF IIT Mumbai**.** Elemental analysis of both complexes was performed on Elementar Excellence in Elements model Unicube superuser V1.3.2(065bdfa). The electronic spectra of both copper complexes were recorded in DMSO solvent at 250–900 nm range using a V-730 UV-vis spectrophotometer.

4b.2.5 Computational measurements (DFT)

Density functional theory was employed for full geometry optimization of both complexes. A basis set B3LYP/LANL2DZ was used to optimize the complexes [23][24]. The HOMO–LUMO energies were determined and visualized using the Gauss View 6.0, a molecular visualisation software. LANL2DZ is a double zeta basis set, i.e. it doesn't include any polarization functions, but it does have relativistic effects through pseudopotentials [25]. The basis set incorporates effective core potentials (ECPs) to simplify the treatment of core electrons, particularly for heavier elements like copper. This basis set is especially useful for transition metals and other heavier elements. Natural Bond Orbital (NBO) analysis was employed to evaluate the relationship between occupied and vacant Lewis orbitals of the NBO type. Additionally, a spin density plot was generated to examine the distribution of electrons in the α and β spin states.

4b.2.6 *In vitro* Anti-cancer activity

Anticancer activity of complex-**8** was examined via MTT assay using Lung adenocarcinoma (NCI-H23), Hepatocellular carcinoma (HepG2) and Neuroblastoma (SH-SY5Y) cell lines. Cisplatin was taken as a reference to compare the activity.

4b.2.6.1 Cell culture conditions

At 37 °C with 5% CO_2, HepG2 and SH-SY5Y cells were grown in MEM medium (Himedia), while in RPMI-1640 medium (Himedia), the NCI-H23 cells were cultured and supplemented with 10% fetal bovine serum and 1% penicillin-streptomycin solution (Gibco). National Centre for Cell Science (NCCS), Pune, was a source of the cell lines.

4b.2.6.2 MTT- Cell viability assay

For 24 hr, cancer cells were grown in 96-well plates (Thermofisher Scientific) at a density of 7000 cells per well using a cell culture medium to check the cell viability. Cancer cells were exposed to various concentrations of complex-**8** for 24 hr at 37°C and 5% CO_2 in an incubator. Media was removed after incubation, and MTT (0.5 mg/ml) was added to each well plate. The plates were then incubated for four hr at 37°C with 5% CO_2. The obtained formazan crystals were dissolved in 100 µl DMSO. Using a Synergy H1 multi-mode microplate reader, absorbance was measured at 570 nm to calculate optical density. GraphPad Prism Software was used to calculate the IC_{50} value [26][11]. Cis platin was taken as a reference compound to compare the antiproliferative properties. The following formula (1) was used to calculate the cell viability.

(OD of treatment/OD of control) x100 (1)

4b.3 Results and Discussion

Two Square planar Cu(II) acyl pyrazolone complexes were synthesized. Both complexes are stable at room temperature and characterized via FT-IR, UV–Vis, ESR, TGA and X-ray crystallography. Density functional theory (DFT) was employed for geometry optimization. Hirshfeld surface analysis was conducted to explore intermolecular interactions and crystal packing in the solid-state structures. The cytotoxicity (MTT) assay was done against three cancer cell lines, NCI-H23, HePG2 and SH-SY5Y cancer cells. The IC_{50} values of complex-**8** were determined. Due to the superior effectiveness of **complex-8**, this complex was further studied and compared with a well-known drug, cisplatin.

4b.3.1 FTIR spectral analysis

The free ligands and their metal complexes have had their FTIR spectra measured at 4000–400 cm^{-1}. The IR frequencies of the ν(C=O) group in 3,5-dimethyl benzoyl chloride and pyrazolone appear at 1585 cm^{-1} and 1603 cm^{-1}, respectively, for **complex-7.** For **complex-8**, the ν(C=O) frequencies of 3,5-dimethyl benzoyl and pyrazolone are observed at 1526 cm^{-1} and 1593 cm^{-1}, respectively. The FTIR spectra, similar to those of the ligand, show noticeable shifts in the stretching frequencies of the C-O functionalities, indicating coordination between the ligand and metal ions during complexation. During complexation, the M-O bond forms due to charge transfer from the oxygen atom in the C=O group to the metal ion. This charge migration strengthens the M-O bond while weakening the C-O bond, leading to a noticeable decrease in IR frequencies in the complex compared to the ligand.

Specifically, the charge transfer from the oxygen atom of the C=O group in pyrazolone to the metal ion strengthens the M-O bond. It weakens the C=O bond, increasing the bond length of the pyrazolone's C=O bond. **Table 4b.1** summarises the distinctive FTIR bands of the respective ligands and their complexes. The FTIR spectra of complex-**7** and complex-**8** are shown in **Figs.4b.3-4b.4.**

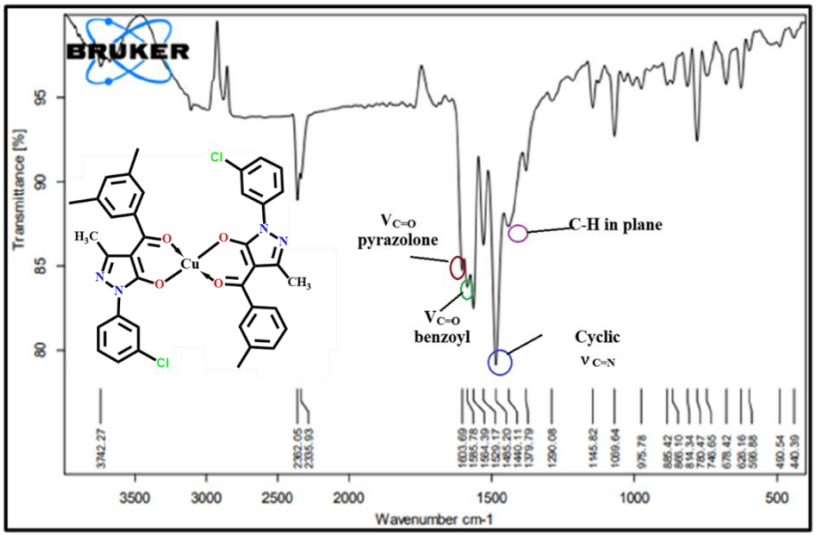

Fig.4b.3. FTIR spectrum of complex-7

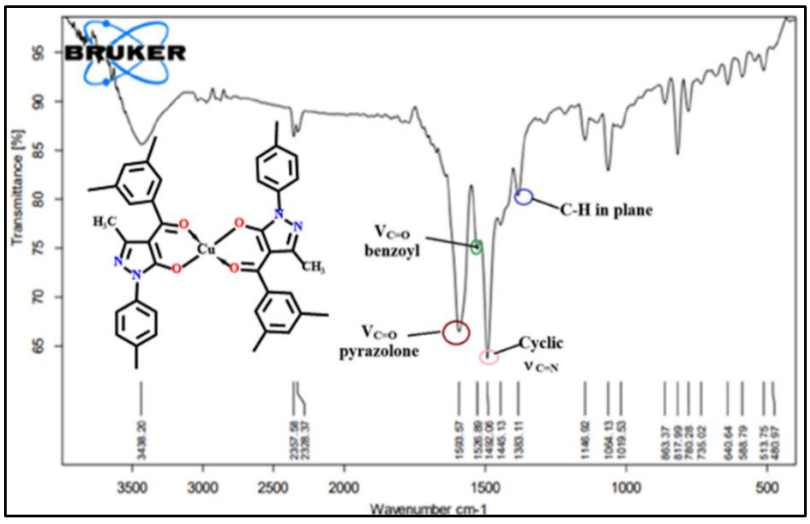

Fig.4b.4. FTIR spectrum of complex-8

Table 4b.1. FTIR spectral data of ligands, complexes 7 and 8

Code	HL^{VII}	Complex-7	HL^{VIII}	Complex-8
ν(C=O) of benzoyl chloride	1621	1585	1622	1526
ν(C=O) of Pyrazolone	1554	1603	1422	1593
Cyclic ν(C=N)	1589	1529	1606	1492
C–H in-plane deformation	1080	1379	1066	1383

4b.3.2 Thermogravimetric analysis

Thermogravimetric analysis (TGA) describes how the mass of a substance changes as a function of temperature. The two-step decomposition of two square-planar copper complexes can be examined using this technique. Both complexes exhibit thermal decomposition between 100°C and 550°C, demonstrating remarkable thermal stability. The spectra include three graphs of different colours: blue (TGA), green (DTA) and red (DTG). In complex-**7,** no solvent degradation is observed up to 300°C, indicating the absence of a solvent molecule in the fifth coordination position. In contrast, some degradation is observed in the complex-**8** up to 250°C, attributed to the presence of a coordinated water molecule. In the complex-**7**, pyrolysis of the HL^{VII} ligand occurs between 300°C and 400°C, while in the complex-**8**, pyrolysis of the HL^{VIII} ligand starts at 300°C. TG-DTA analysis of complex-**7** shows a total weight loss of 61.8% on the TG graph (blue spectrum), which can be characterized by two phases: (i) a 47.8% weight loss and (ii) a 14.0% weight loss. In complex-**8,** a total weight loss of 49.64% is observed. The green and red spectra represent the DTA and DTG graphs, respectively. The resulting CuO residue remains stable up to 550°C. The TG-DTA plots of both complexes are pictured in **Figs.4b.5-4b.6.**

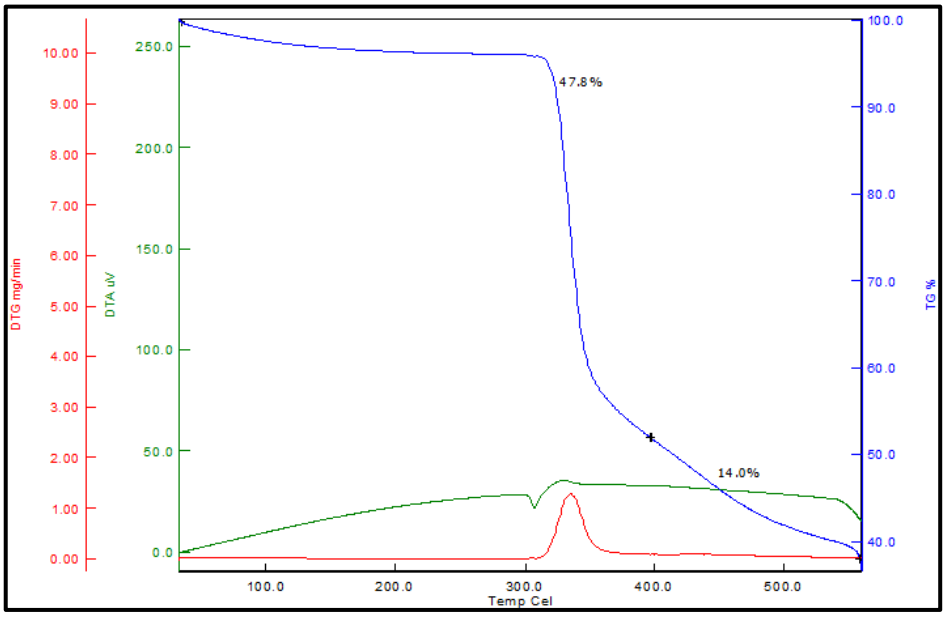

Fig.4b.5. TG-DTA plot of complex-7

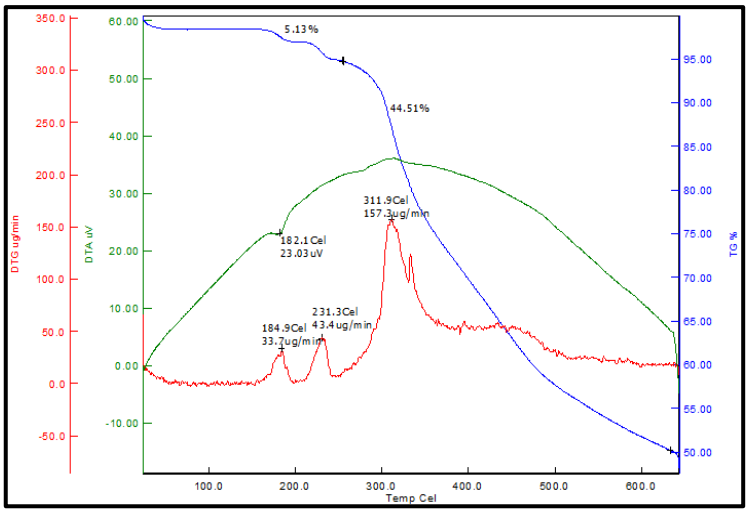

Fig.4b.6. TG-DTA plot of complex-8

4b.3.3 Electronic spectral analysis

To ascertain the energy gap, the crystal samples of both compounds were subjected to UV-visible absorption measurements up to 950 nm. The electronic spectra of complex-**7** and complex-**8** were recorded in DMSO at a concentration of 1×10^{-3} M. For complex-**7**, sharp absorption bands appear at **282 nm** and **358 nm**, while complex-**8** shows them at **278 nm** and **375 nm**. The transitions at 282 nm and 278 nm correspond to ligand-to-metal charge transfer (**LMCT**), involving electron transfer from the oxygen donor atoms of the pyrazolone ligand to the Cu(II) centre. Absorptions at **358 nm** and **375 nm** could be interpreted as **intra-ligand charge transfer (ILCT);** however, they are more likely to arise from **ligand-based transitions**, $\pi \rightarrow \pi^*$ or $n \rightarrow \pi^*$ excitations. Additionally, both complexes exhibit a broad d-d transition at **705–706 nm**, assigned to the $\mathbf{d_{xy} \rightarrow d_{x^2-y^2}}$, characteristic of square planar Cu(II) complexes [27][28]. **Figs.4b.7-4b.8** represent the electronic transition of both complexes.

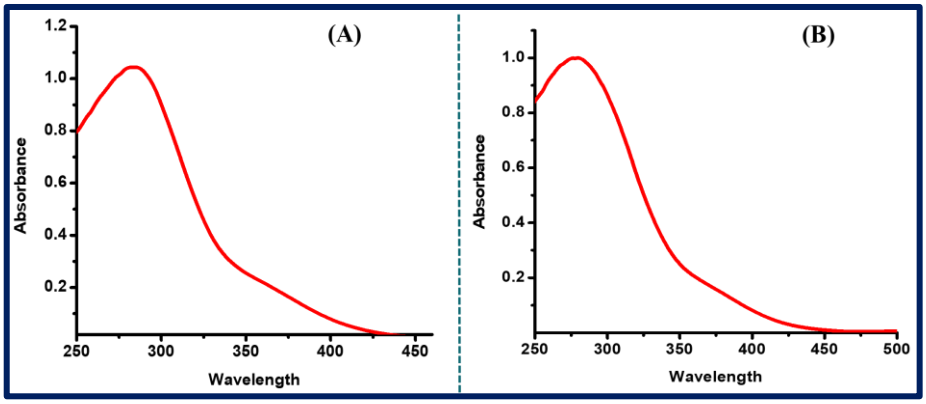

Fig.4b.7. LMCT & ligand-based transitions in (A) complex-7 and (B) complex-8 in a diluted solution of DMSO

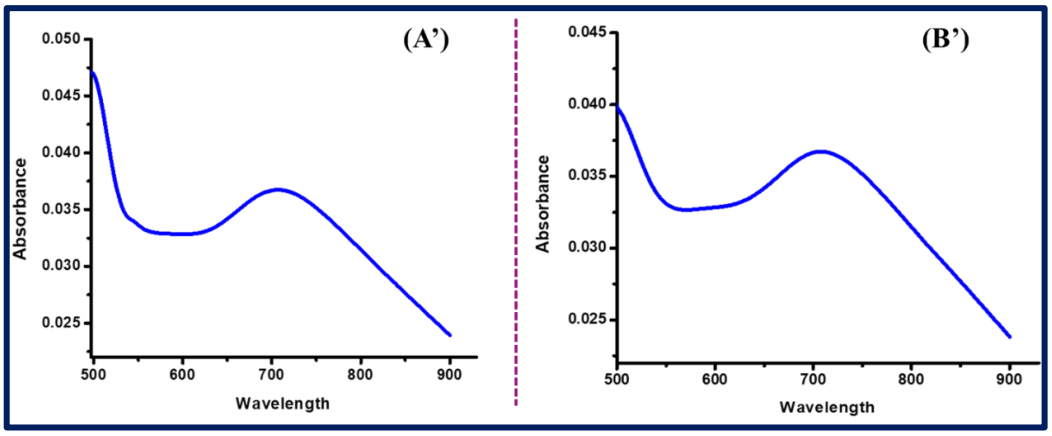

Fig.4b.8. d-d spectra of (A') complex-7 and (B') complex-8 in 1x10^{-3} M solution of DMSO

4b.3.4 Single crystal X-ray diffraction analysis

The structural analysis evidenced that the Cu metal centre is coordinated by four oxygen atoms of ligands in two complexes. The geometry of both complexes appears in the form of a square planar. The complex-**7** and complex-**8** crystallize in the '**Monoclinic crystal system'** with space groups ***P*2$_1$/c** and ***P*2$_1$/n**, respectively. The bond distance between Cu-O(1) is 1.917(12) Å. Bond length 1.941(11) Å is found for Cu-O(2) in complex-**7**. Furthermore, The Bond length of Cu-O(1) and Cu-O(2) in complex-**8** is 1.9106(19) Å and 1.9369(17) Å respectively. The Cu-O bond lengths at 180° are the same due to the inversion centre. Hence, all this information implies that the geometry around copper is square planar in both complexes. An ORTEP view of both copper complexes is demonstrated in **Fig.4b.9.** A perspective view of the packing configuration of both complexes is depicted in **Fig.4b.10.** The crystal packing with miller indices of both complexes is depicted in **Fig.4b.11.** The symmetry elements of complex-**7** and complex-**8** are pictured in **Fig.4b.12.** The graphical illustration of intermolecular H-bonding, off-set π···π stacking interactions and centroid-centroid (Cg-Cg) distance for two crystal structures are shown in **Figs. 4b.13** and **4b.14.** A 2D representation of the single crystal structures of complex-**7** and complex-**8** is pictured in **Fig.4b.15.** Analysis of short ring interactions with Cg-Cg Distances (Pi-Pi) of complex-**7 & 8** is listed in **Tables 4b.2-4b.3.** These interactions were calculated using Mercury software, with additional analysis performed using PLATON software. The details of short ring interactions, including Cg–Cg distances (π···π), and the associated interactions are evident from the inter-centroid separations, which range from 3.4892(1) Å to 5.1443(1) Å for complex-**7** and from 3.4615(2) Å to 5.8673(3) Å for complex-**8**, as calculated using PLATON software. **Table 4b.4** contains the bond parameters of complex-**7**. The hydrogen bond parameters and symmetry transformations of complex-**7** are mentioned in **Tables 4b.5-**

4b.6. Similarly, **Tables 4b.7-4b.9** contains the bond parameters, hydrogen bond parameters and symmetry transformations of complex-**8**. The refinement parameters of complex-**7** and complex-**8** are mentioned in **Table 4b.10.**

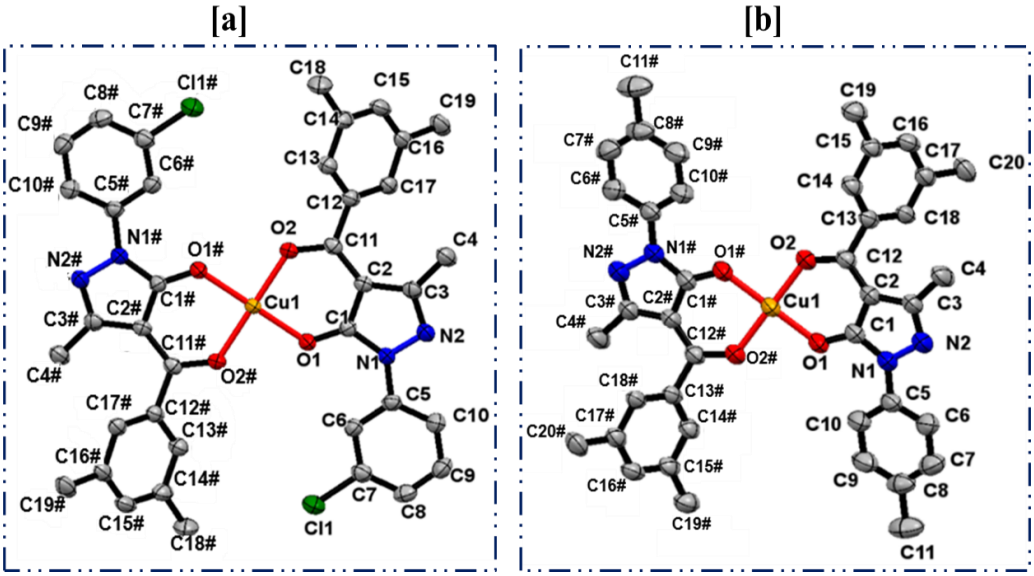

Fig.4b.9. [a] is an ORTEP view of complex-7 and [b] is an ORTEP view of complex-8 with displacement ellipsoids drawn at 55% (Hydrogen atoms omitted for clarity)

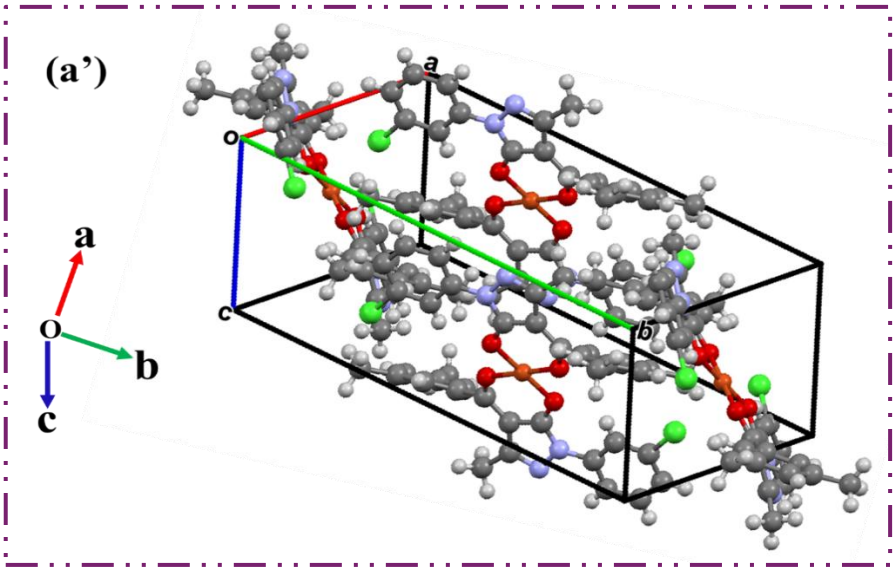

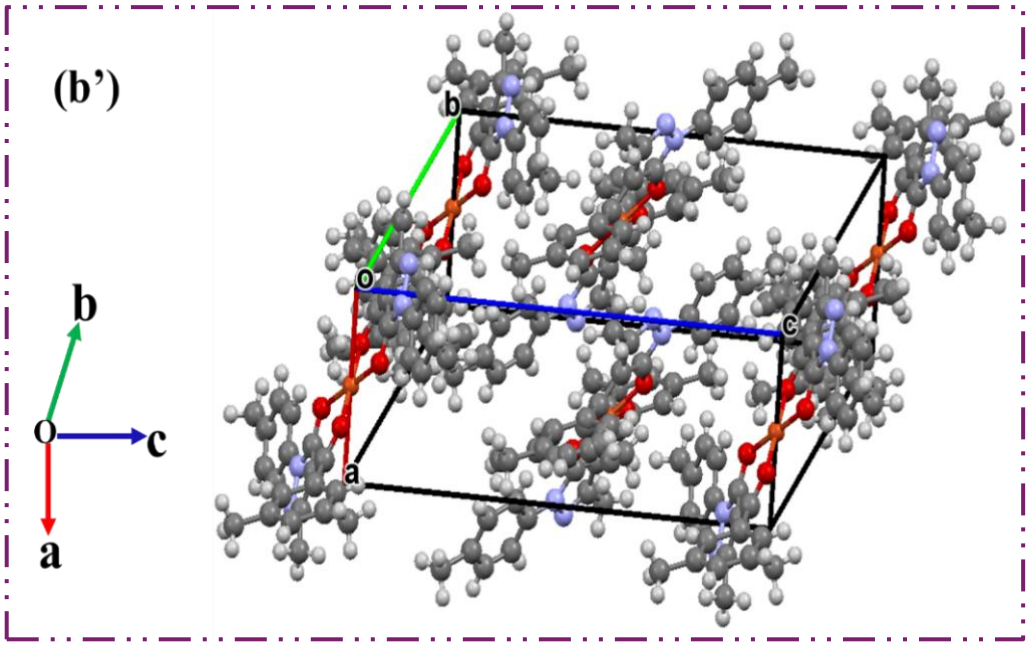

Fig.4b.10. The perspective view of a packing configuration of (a') complex-7 and (b') complex-8 along with a-axis and b-axis, respectively

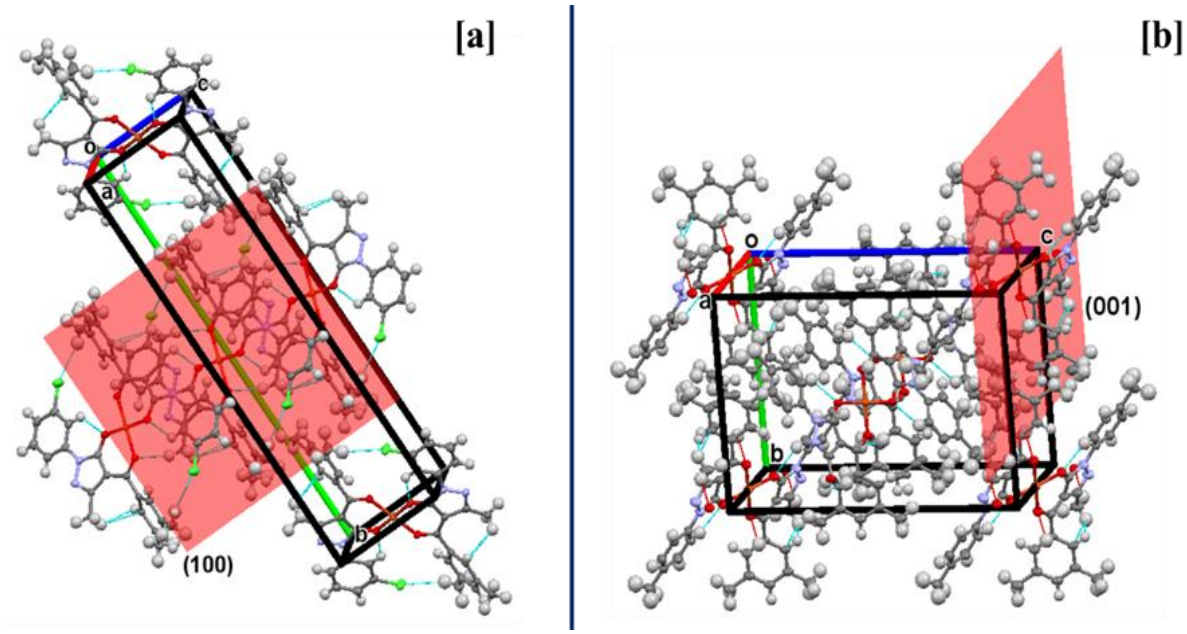

Fig.4b.11. The crystal packing of complex-7 along the c-crystallographic axis & the (100) Miller plane is presented, and the crystal packing of complex-7 along the a-crystallographic axis crystallographic axis & the (100) Miller plane is presented

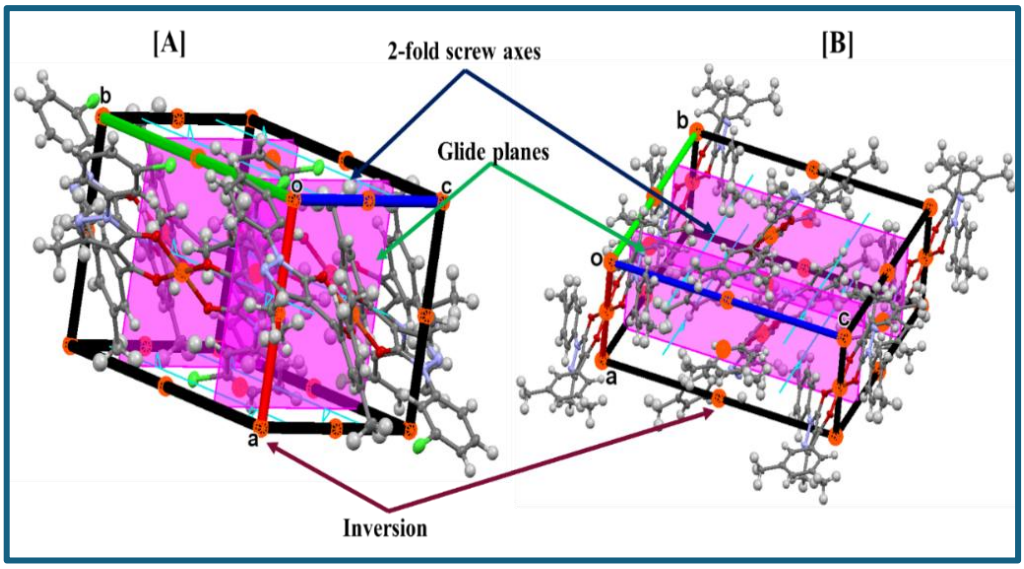

Fig.4b.12. Symmetry elements of complex-7 and complex-8

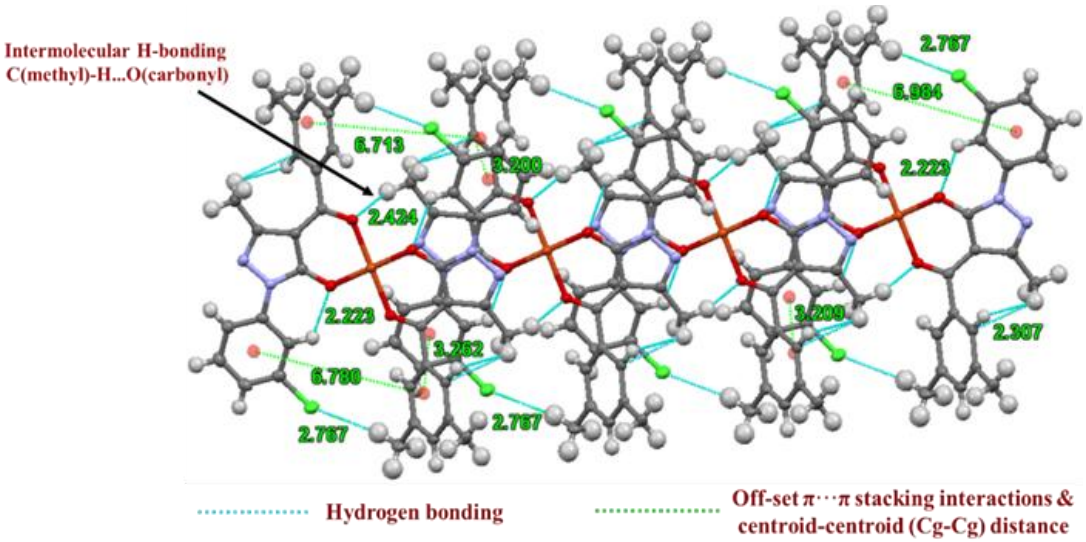

Fig.4b.13. Graphical illustration of intermolecular H-bonding, off-set π···π stacking interaction and centroid-centroid (Cg-Cg) distance in the crystal structure of complex-7

Table 4b.2. Analysis of short ring-interactions with Cg-Cg Distances (Pi-Pi) of complex-7

Cg(I)-Cg(J)	[ARU(J)]	Cg-Cg	Alpha	Beta	Gamma	CgI Perp	CgJ Perp
Cg(1)-Cg(1)	[3657.01]	3.4892(1)	0	18.0	18.0	3.3190	3.3190
Cg(1)-Cg(4)	[3657.01]	5.1443(1)	5	46.4	51.6	3.1975	3.5448
Cg(1)-Cg(4)	[3757.01]	3.7977(1)	5	20.1	22.9	3.4991	3.5658
Cg(4)-Cg(1)	[3657.01]	5.1443(1)	5	51.6	46.4	3.5448	3.1975
Cg(4)-Cg(1)	[3757.01]	3.7977(1)	5	22.9	38.1	3.5658	3.4990
Cg(4)-Cg(4)	[3757.01]	4.5839(1)	0	38.1	20.1	3.6073	3.6073
Cg(4)-Cg(5)	[3657.01]	4.6193(1)	52	12.6	60.1	2.3034	4.5089
Cg(5)-Cg(5)	[4554.01]	4.9418(1)	8	43.9	51.9	3.0480	3.5637
Cg(5)-Cg(5)	[4555.01]	4.9418(1)	8	51.9	43.9	3.5637	3.0480

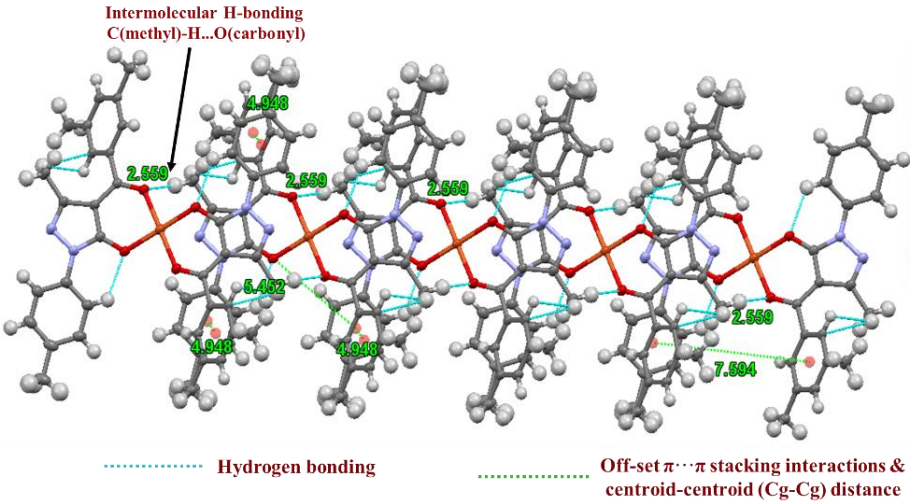

Fig.4b.14. Graphical illustration of intermolecular H-bonding, off-set π···π stacking interaction and centroid-centroid (Cg-Cg) distance in the crystal structure of complex-8

Table 4b.3. Analysis of short ring-interactions with Cg-Cg Distances (Pi-Pi) of complex-8

Cg(I)-Cg(J)	[ARU(J)]	Cg-Cg	Alpha	Beta	Gamma	CgI Perp	CgJ Perp
Cg(1)-Cg(1)	[3555.01]	3.4615(2)	0	13.5	13.5	3.3190	3.3190
Cg(1)-Cg(4)	[2555.01]	5.8673(3)	56	16.6	69.5	2.0510	5.6226
Cg(1)-Cg(4)	[3555.01]	5.2588(2)	8	45.6	51.7	3.2562	3.6811
Cg(4)-Cg(1)	[3555.01]	5.2588(2)	8	51.7	45.6	3.6811	3.2562
Cg(4)-Cg(5)	[2545.01]	5.3913(2)	62	23.7	63.0	2.4481	4.9358
Cg(4)-Cg(5)	[3555.01]	4.9477(2)	61	3.8	61.1	2.3919	4.9358
Cg(4)-Cg(6)	[2545.01]	5.5919(2)	63	24.8	65.9	2.2816	5.0776
Cg(4)-Cg(6)	[3555.01]	4.8324(2)	59	6.6	56.1	2.6959	4.7999
Cg(5)-Cg(5)	[3565.01]	4.6669(2)	0	41.3	41.3	3.5087	3.5087
Cg(5)-Cg(6)	[3565.01]	4.8136(2)	3	40.8	44.0	3.4638	3.6430
Cg(5)-Cg(6)	[3665.01]	4.5930(2)	3	43.7	40.7	3.4795	3.3229
Cg(6)-Cg(4)	[3555.01]	4.8324(2)	59	56.1	6.6	4.7999	2.6959
Cg(6)-Cg(5)	[3565.01]	4.8136(2)	3	44.0	40.8	3.6430	3.4638
Cg(6)-Cg(5)	[3665.01]	4.5930(2)	3	40.7	43.7	3.3229	3.4795
Cg(6)-Cg(6)	[3565.01]	4.9766(2)	0	43.7	43.7	3.5969	3.5969

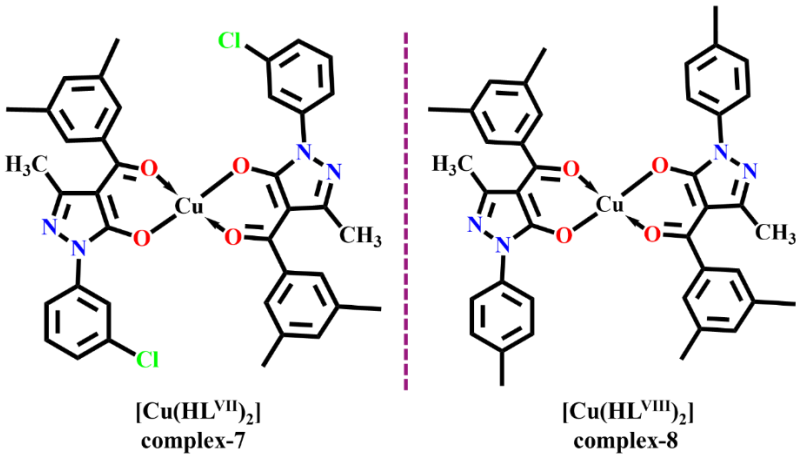

Fig.4b.15. 2D representation of the single crystal structures of complex-7 and complex-8

Table 4b.4 Bond Lengths and Bond Angles Parameters of complex-7

Atoms	Bond lengths (Å)	Atoms	Bond angles (°)
Cu(1)-O(1)	1.9174(12)	O(1)-Cu(1)-O(1)	180.0
Cu(1)-O(1)	1.9174(12)	O(1)-Cu(1)-O(2)	93.52(5)
Cu(1)-O(2)	1.9410(11)	O(1)-Cu(1)-O(2)	86.47(5)
Cu(1)-O(2)	1.9410(11)	O(1)-Cu(1)-O(2)	86.48(5)
Cl(1)-C(7)	1.7480(19)	O(1)-Cu(1)-O(2)	93.53(5)
C(1)-O(1)	1.278(2)	O(2)-Cu(1)-O(2)	180.00(3)
C(11)-O(2)	1.270(2)	C(1)-O(1)-Cu(1)	120.10(11)
N(1)-N(2)	1.402(2)	C(11)-O(2)-Cu(1)	128.29(11)
N(1)-C(1)	1.366(2)	C(1)-N(1)-N(2)	111.59(14)
N(1)-C(5)	1.416(2)	C(1)-N(1)-C(5)	130.04(15)
N(2)-C(3)	1.313(2)	N(2)-N(1)-C(5)	118.34(14)
C(1)-C(2)	1.422(2)	C(3)-N(2)-N(1)	106.10(14)
C(2)-C(11)	1.411(2)	O(1)-C(1)-N(1)	123.86(15)
C(2)-C(3)	1.438(2)	O(1)-C(1)-C(2)	130.26(15)
C(3)-C(4)	1.492(2)	N(1)-C(1)-C(2)	105.86(14)
C(16)-C(17)	1.394(2)	C(11)-C(2)-C(1)	121.59(15)
C(16)-C(19)	1.507(3)	N(2)-C(3)-C(2)	111.32(15)

Table 4b.5. Hydrogen bonds of complex-7

D-H...A	d(D-H)	d(H...A)	d(D...A)	<(DHA)
C(4)-H(4A)...O(2)#2	0.98	2.42	3.235(2)	139.8
C(6)-H(6A)...O(1)	0.95	2.22	2.866(2)	124.1

Table 4b.6. Complex-7: Symmetry transformations used to generate equivalent atoms

	x, y, z coordinates
1	x, y, z
2	-x, y+1/2, -z+1/2
3	-x, -y, -z
4	x, -y-1/2, z-1/2

Table 4b.7. Bond lengths & Bond angles parameters of complex-8

Atoms	Bond lengths (Å)	Atoms	Bond angles (°)
Cu(1)-O(1)	1.9106(19)	O(1)-Cu(1)-O(1)	180.0
Cu(1)-O(1)	1.9107(19)	O(1)-Cu(1)-O(2)	86.19(8)
Cu(1)-O(2)	1.9369(17)	O(1)-Cu(1)-O(2)	93.81(8)
Cu(1)-O(2)	1.9369(17)	O(1)-Cu(1)-O(2)	93.81(8)
O(1)-C(1)	1.283(3)	O(1)-Cu(1)-O(2)	86.19(8)
O(2)-C(12)	1.272(3)	O(2)-Cu(1)-O(2)	180.00(3)
N(2)-C(3)	1.301(4)	C(1)-O(1)-Cu(1)	119.79(18)
N(1)-C(1)	1.354(4)	C(12)-O(2)-Cu(1)	127.56(17)
N(1)-N(2)	1.398(3)	C(1)-N(1)-N(2)	111.0(2)
N(1)-C(5)	1.422(4)	C(1)-N(1)-C(5)	130.0(3)
C(8)-C(11)	1.521(5)	N(2)-N(1)-C(5)	118.8(2)
C(1)-C(2)	1.416(4)	C(3)-N(2)-N(1)	106.7(2)
C(2)-C(12)	1.398(4)	O(1)-C(1)-N(1)	123.9(2)
C(2)-C(3)	1.4367(4)	O(1)-C(1)-C(2)	129.6(3)
		N(2)-C(3)-C(2)	111.1(2)
		N(2)-C(3)-C(4)	119.8(3)

Table 4b.8. Hydrogen bonds of complex-8

D-H…A	d(D-H)	D(H...A)	d(D...A)	<(DHA)
C(4)-H(4A)...O(2)#2	0.96	2.56	3.400(4)	146.3
C(10)-H(10A)...O(1)	0.93	2.25	2.882(4)	124.9

Table 4b.9. Complex-8: Symmetry transformations used to generate equivalent atoms

	x, y, z coordinates
1	x, y, z
2	-x+1/2, y+1/2, -z+1/2
3	-x, -y, -z
4	x-1/2, -y-1/2, z-1/2

Table 4b.10. Refinement parameters of complex-7 and complex-8

CODE	$[Cu(HL^{VII})_2]$ Complex-7	$[Cu(HL^{VIII})_2]$ Complex-8
CCDC number	2342479	2342480
Chemical formula	$C_{38}H_{32}Cl_2CuN_4O_4$	$C_{40}H_{38}CuN_4O_4$
Formula weight	743.11	702.28
Crystal system	Monoclinic	Monoclinic
Space group	$P2_1/c$	$P2_1/n$
Volume	1626.21(5) $Å^3$	1761.00(12) $Å^3$
Temperature	100(2) K	295(2) K
Wavelength	1.54184 Å	1.54184 Å
Z	2	2
Density	1.518 Mg/m^3	1.324 Mg/m^3
Unit cell dimension	a= 8.4243(2) Å b= 27.7723(4) Å c= 7.01630(10) Å	a = 7.2657(3) Å b = 13.4359(4) Å c = 18.2180(8) Å
	α, γ = 90°, β= 97.8400(10)°	α, γ = 90°, β= 98.035(4)°
F (0 0 0)	766	734
Theta range	3.183 to 78.704°	4.103 to 78.982°
Absorption Correction	Semi-empirical from equivalents	Semi-empirical from equivalents
Absorption coefficient	2.865 mm^{-1}	1.249 mm^{-1}
Index ranges	-10<=h<=10 -34<=k<=33 -6<=l<=8	-8<=h<=5 -17<=k<=17 -22<=l<=22
Reflections collected	19254	18246
Independent reflections	3418 [R(int) = 0.0430]	3667 [R(int) = 0.0592]
Goodness-of-fit on F^2	1.054	1.034
Final R indices [I>2sigma(I)]	R1 = 0.0412, wR2 = 0.0911	R1 = 0.0533, wR2 = 0.1460
Data/restraints/parameters	3418/0/226	3667/294/ 278
Largest diff. Peak and hole	0.345 and -0.412 $e.Å^{-3}$	0.413 and -0.533 $e.Å^{-3}$

4b.3.5 Computational analysis employing DFT

The isolated molecules were used for the theoretical calculations, while an experimental result was determined in a solid state [29]. The current study compared the impact of the various functions on the estimated molecular characteristics of the systems under investigation using DFT in combination with B3LYP. The B3LYP/LANL2DZ level basis set was used for the geometry optimization of both complexes. A Gaussview 6.0 software was used to process the input files [23][30]. The optimization energies -123.7430 keV and -100.8708 keV, respectively, were observed for complex**-7** and complex**-8.** The optimized geometries of both complexes were utilized as input for vibrational frequency analysis. Once convergence was reached, harmonic vibrational frequencies were calculated at the same theoretical level to ensure that the stationary points did not exhibit any imaginary frequencies. When there is a close match between the theoretical values and the experimental spectra, the considerations discussed in the section on FTIR spectroscopic analysis become highly significant. Theoretical IR frequencies were determined using a DFT approach [31]**.** The HOMO-LUMO energies are crucial for various chemical interactions [32]. Excitation energies can be determined using various methods in theory. The first, and easiest, is the difference between a system's lowest unoccupied molecular orbital (LUMO) and its highest occupied molecular orbital (HOMO). The conclusive charge transfer interaction inside the molecule is explained by the electron-accepting capacity of the electron-acceptor group, as indicated by the reduction in the HOMO and LUMO energy gap. The energy difference between the HOMO and LUMO of a molecule determines its kinetic stability, chemical reactivity, optical polarizability and chemical hardness or softness. Based on the information on the composition of the molecular orbitals (HOMO and LUMO) above, we can compute the molecular properties that influence the selectivity and reactivity of a compound. These properties were approximated using Koopmans's theorem, which connects the HOMO and LUMO energies. Koopmans theorem provides an alternative method for estimating the ionization energy and electron affinity of chemical species. According to this theorem, the ionization energy can be approximated by the negative of the HOMO energy, while the electron affinity corresponds to the negative of the LUMO energy [33]. **Fig.4b.16** depicts the optimized geometry of both copper complexes. **Tables 4b.11-4b.12** display the energy values and global parameters of both complexes, respectively.

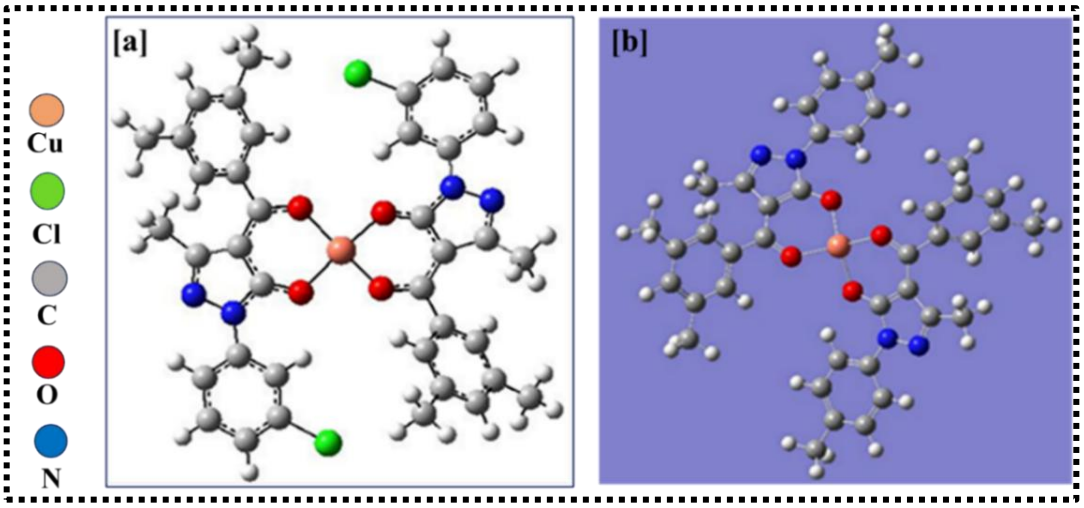

Fig.4b.16. DFT optimized geometry of [a] complex-7 and [b] complex-8

4b.3.5.1 A correlation of biological study with HOMO-LUMO energy analysis

Both synthesized complexes were computed and optimized using the B3LYP/LANL2DZ basis set. The same basis set was employed to calculate the HOMO-LUMO energy gap values, which help identify the molecule's ability to donate and accept electrons. According to the analysis, the band gap energy (ΔE) for complex-**7** is 4.038 eV, while for complex-**8** it is 3.795 eV. Since electron acceptor groups have a significant capacity to receive electrons, the HOMO-LUMO energy gap defines the charge transfer interaction within the molecule. This interaction facilitates the molecule's ability to accept electrons, linked to its bioactivity [38]. In this study, complex-**8** exhibits a lower energy gap compared to complex-**7**. Therefore, a biological study of complex-**8** was conducted using three cancerous cell lines. The HOMO-LUMO molecular orbitals and the energy level diagram of complex-**7** and complex-**8** are illustrated in **Figs.4b.17-4b.18**, respectively.

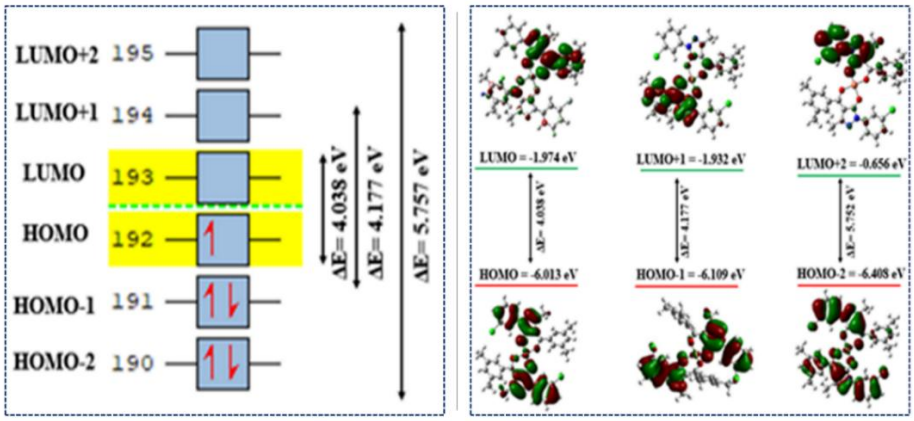

Fig.4b.17. HOMO-LUMO molecular orbital diagram of complex-7

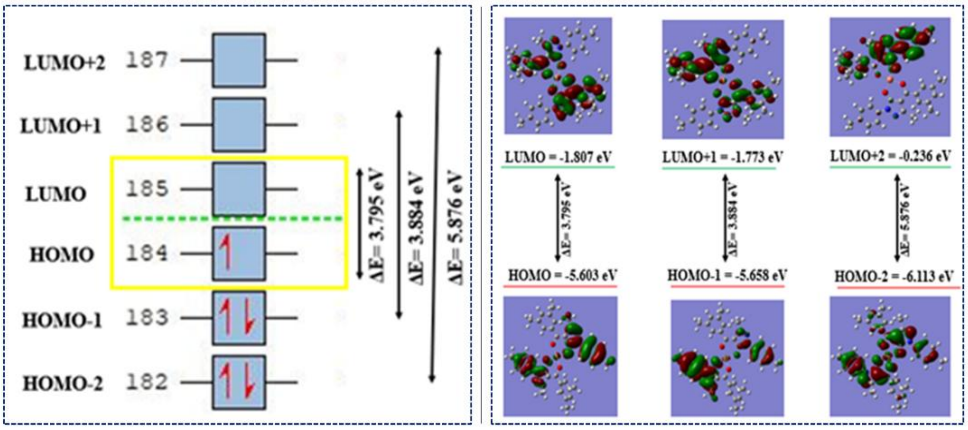

Fig.4b.18. HOMO-LUMO molecular orbital diagram of complex-8

Table 4b.11. HOMO-LUMO energy values

Levels	Complex-7	Complex-8
HOMO	-6.013 eV	-5.603 eV
LUMO	-1.974 eV	-1.807 eV
HOMO-1	-6.109 eV	-5.658 eV
LUMO+1	-1.974 eV	-1.773 eV
HOMO-2	-6.408 eV	-6.113 eV
LUMO+2	-0.656 eV	-0.236 eV

Table 4b.12. Global parameters of complex-7 and complex-8

Properties	Mathematical formula	Complex-7	Comple-8
E_{HOMO}	E_{HOMO}	-6.013	-5.603
E_{LUMO}	E_{LUMO}	-1.974	-1.807
ΔE	$\Delta E = E_{LUMO} - E_{HOMO}$	4.039	3.795
Ionization potential (IP)	$IP = -E_{HOMO}$	6.013	5.603
Chemical Potential (μ)	$\mu = 1/2 (E_{HOMO} + E_{LUMO})$	-3.993	-3.705
Electron affinity (EA)	$EA = -E_{LUMO}$	1.974	1.807
Electronegativity (EN)	$EN = -1/2 (E_{HOMO}+E_{LUMO})$	3.993	3.705
Global Hardness (Η)	$\eta = -1/2 (E_{HOMO}-E_{LUMO})$	2.019	1.898
Softness (S)	$S = 1/2\eta$	0.247	0.263
Electrophilicity index (ω)	$\omega = \mu^2/2\eta$	3.948	3.616

Theoretical IR frequencies were obtained using DFT calculations after the complete optimization. Theoretical vibrations can be used to investigate the changes which occur during complexation. A comparison of theoretical IR frequencies and practical IR frequencies is listed in **Table 4b.13.** The theoretical FTIR spectrum of complex-**7** is depicted in **Fig.4b.19.** Theoretical and practical bonding parameters of complex-**7** and complex-**8** are listed in **Table 4b.14.**

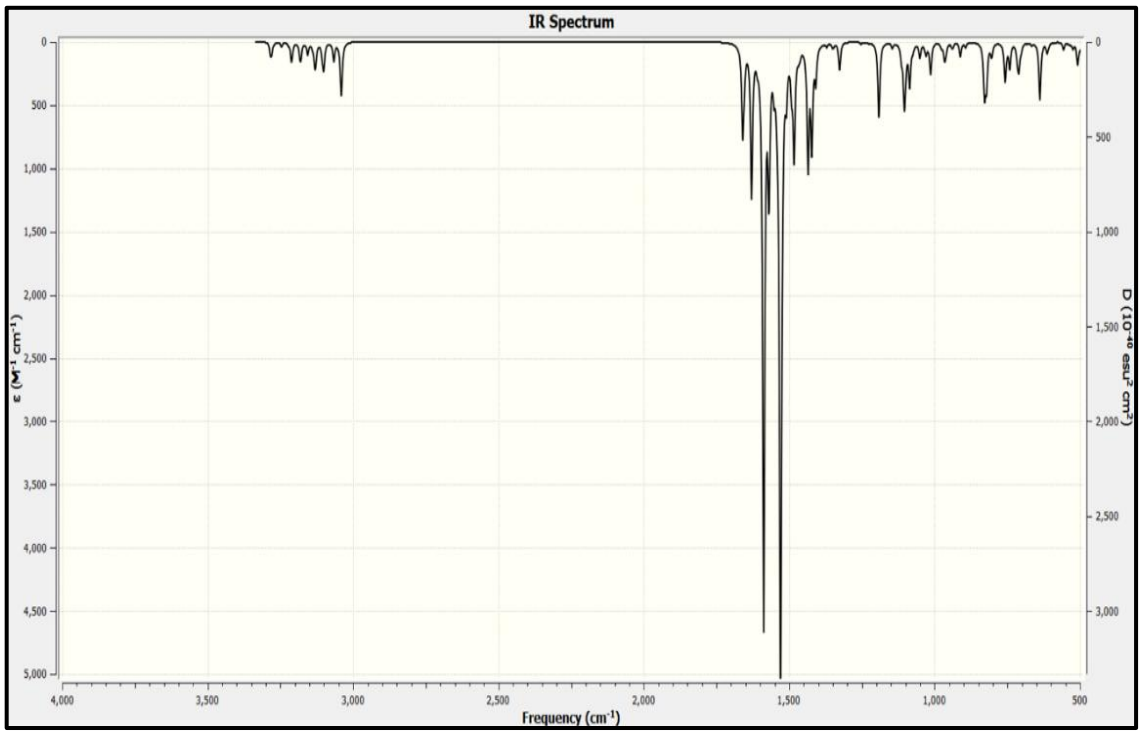

Fig.4b.19. FTIR spectrum of complex-7 through DFT computational analysis

Table 4b.13. A comparison of the practical and theoretical bond parameters

IR Frequencies (cm^{-1})	Complex-7		Complex-8	
	Theoretical	**Practical**	**Theoretical**	**Practical**
ν(C=O) of benzoyl chloride	1587	1585	1589	1526
ν(C=O) of Pyrazolone	1609	1603	1611	1593
Cyclic ν(C=N)	1535	1529	1567	1492
C–H in-plane deformation	1370	1379	1379	1383

Table 4b.14. Comparison of theoretical and practical bonding parameters of complex-7 and complex-8

Atoms	Practical bond length (Å)	Theoretical bond length (Å)	Atoms	Practical bond angles (°)	Theoretical bond angles (°)
Complex-7					
Cu(1)-O(1)	1.9174(12)	1.918	O(1)-Cu(1)-O(1)	180.0	181.22
Cu(1)-O(1)	1.9174(12)	1.918	O(1)-Cu(1)-O(2)	93.52(5)	93.27
Cu(1)-O(2)	1.9410(11)	1.954	O(1)-Cu(1)-O(2)	86.47(5)	92.83
Cu(1)-O(2)	1.9410(11)	1.955	O(1)-Cu(1)-O(2)	86.48(5)	92.20
Cl(1)-C(7)	1.7480(19)	1.831	O(1)-Cu(1)-O(2)	93.53(5)	92.83
C(1)-O(1)	1.278(2)	1.300	O(2)-Cu(1)-O(2)	180.00(3)	181.32
C(11)-O(2)	1.270(2)	1.300	C(1)-O(1)-Cu(1)	120.10(11)	122.31
N(1)-N(2)	1.402(2)	1.423	C(11)-O(2)-Cu(1)	128.29(11)	130.43
N(1)-C(1)	1.366(2)	1.375	C(1)-N(1)-N(2)	111.59(14)	110.91
N(1)-C(5)	1.416(2)	1.414	C(1)-N(1)-C(5)	130.04(15)	130.12
N(2)-C(3)	1.313(2)	1.326	N(2)-N(1)-C(5)	118.34(14)	118.93
C(1)-C(2)	1.422(2)	1.437	C(3)-N(2)-N(1)	106.10(14)	106.49
C(2)-C(11)	1.411(2)	1.482	O(1)-C(1)-N(1)	123.86(15)	123.75
C(2)-C(3)	1.438(2)	1.489	O(1)-C(1)-C(2)	130.26(15)	129.76
C(3)-C(4)	1.492(2)	1.515	N(1)-C(1)-C(2)	105.86(14)	106.48
C(16)-C(17)	1.394(2)	1.413	C(11)-C(2)-C(1)	121.59(15)	121.54
C(16)-C(19)	1.507(3)	1.554	N(2)-C(3)-C(2)	111.32(15)	111.07
Complex-8					
Cu(1)-O(1)	1.9106(19)	1.913	O(1)-Cu(1)-O(1)	180.0	180.56
Cu(1)-O(1)	1.9107(19)	1.913	O(1)-Cu(1)-O(2)	86.19(8)	94.05
Cu(1)-O(2)	1.9369(17)	1.941	O(1)-Cu(1)-O(2)	93.81(8)	93.47
Cu(1)-O(2)	1.9369(17)	1.941	O(1)-Cu(1)-O(2)	93.81(8)	93.20
O(1)-C(1)	1.283(3)	1.301	O(1)-Cu(1)-O(2)	86.19(8)	93.22
O(2)-C(12)	1.272(3)	1.301	O(2)-Cu(1)-O(2)	180.00(3)	181.28
N(2)-C(3)	1.301(4)	1.322	C(1)-O(1)-Cu(1)	119.79(18)	122.30
N(1)-C(1)	1.354(4)	1.375	C(12)-O(2)-Cu(1)	127.56(17)	130.06
N(1)-N(2)	1.398(3)	1.412	C(1)-N(1)-N(2)	111.0(2)	110.89
N(1)-C(5)	1.422(4)	1.425	C(1)-N(1)-C(5)	130.0(3)	130.13
C(8)-C(11)	1.521(5)	1.525	N(2)-N(1)-C(5)	118.8(2)	118.93
C(1)-C(2)	1.416(4)	1.421	C(3)-N(2)-N(1)	106.7(2)	106.66
C(2)-C(12)	1.398(4)	1.400	O(1)-C(1)-N(1)	123.9(2)	123.97
C(2)-C(3)	1.4367(4)	1.434	O(1)-C(1)-C(2)	129.6(3)	129.49
C(3)-C(4)	1.493(4)	1.501	N(2)-C(3)-C(2)	111.1(2)	110.98
			N(2)-C(3)-C(4)	119.8(3)	118.06
			C(9)-C(8)-C(11)	120.4(4)	121.30

4b.3.5.2 Spin density plot

spin density is equivalent to electron density. It may be expressed as the total electron density of one spin less the total electron density of the other spin. When an unpaired electron is present in the system, spin densities may be computed more informatively. It is a difference between the α and the β electron densities. Electronic spin density is positive in areas where electrons are more likely to be found in the α spin state and scattered over the metal centre. In contrast, it is negative in regions where electrons are more likely to be located in the β spin state. Electron paramagnetic resonance (EPR) is an experimental technique that helps

determine electronic spin density. The spin density plots of both complexes are displayed in **Fig.4b.20**. Like the overall electron density, it is computationally visualised using an isosurface. A three-dimensional depiction of all places where a certain function (here, ρ(r)) equals a given value (called the isovalue) is called an isosurface [34].

$$\rho_s(r)=\rho_\alpha(r)-\rho_\beta(r)$$

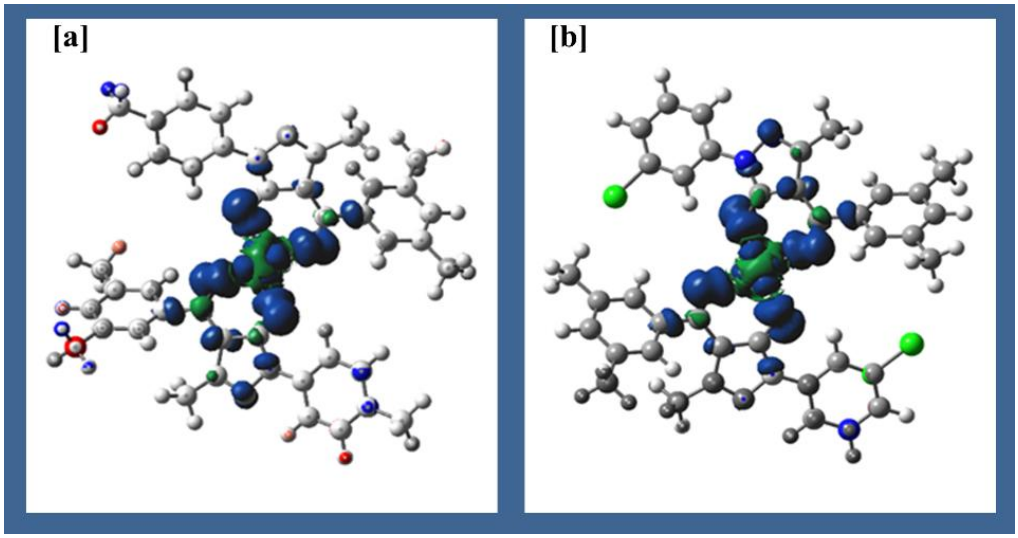

Fig.4b.20. Spin density plot of [a] complex-7 and [b] complex-8

4b.3.5.3 Natural bond orbitals (NBOs) analysis

For the chemical interpretation of hyper-conjugative interaction and electron density transfer from the filled lone pair electron, previous research has demonstrated using the Natural Bond Orbital (NBO) analytical approach [35]. An investigation of the natural bond orbitals (NBOs) of the associated complexes was conducted using the LANL2DZ basis set with the B3LYP approach. All interactions that take place between a Cu(II) ion and a donor atom are considered coordination bonds involving oxygen atoms. Through NBO analysis, it is possible to assess an electron density delocalization, which is linked to a donor-acceptor interaction that stabilises the relationship between unoccupied non-Lewis-type NBOs (acceptor/Reydber) and occupied Lewis-type NBOs (donor). Cu^{+2} has 1.1676 natural atomic charges in the complex-**7** and 1.1638 in complex-**8**. Copper has a [core] 3d (9.13) 4s (0.35) 4p (0.35) natural electrical arrangement. Electrons in the Core (17.9970), Valence (9.8241), Rydberg (0.0117) and Total electrons are 27.8324 in complex-**7**. Electrons in the Core (17.9970), Valence (9.8276), Rydberg (0.0114) and Total electrons are 27.8361 in the complex-**8** having [core] 3d (9.13) 4s (0.34) 4p (0.36) natural electrical arrangement. The results of the DFT computational analysis consistently support the square planar geometry of both synthesized copper acylpyrazolone complexes.

4b.3.6 Hirshfeld surface analysis combined with a 2D fingerprint

One method employed to create and quantify the crystal packing of compounds is a Hirshfeld surface area analysis. After F.L. Hirshfeld, whose "stockholder partitioning" approach for designating atoms in molecules suggested an extension to characterising a molecule in a crystal, Hirshfeld surfaces were named in his honour. The Hirshfeld surface was created to specify the area of a molecule taken up in a crystal to divide the electron density of crystals into snippets of molecules [17]. The CrystalExplorer software was originally created to support Hirshfeld surface (HS) analysis, and this remains one of its main functions [17]. CrystalExplorer17.5 has been used to create the molecules' 2D fingerprint plots and Hirshfeld surface analysis in this study, which also helped to show the structural links between the structural configurations of these closely related molecules. Utilising the descriptor dnorm, directions and intensities of the molecular crystal's intermolecular interactions are projected onto Hirshfeld surfaces. The closest atoms located within (di) and outside (de) the surface, respectively, are the source of the normalised contact distance (dnorm) [40]. Using a variety of properties, including normalised distances (dnorm), de, di, form index, curvedness, fragment patch, etc., to plot the Hirshfeld surface (HS) illustrates the hydrogen bonding and interaction. Through the definition of different shades for brief and extended interactions [41]. In copper complexes, coordination with the Cu(II) ion is primarily facilitated by interactions with four oxygen atoms from two acylpyrazolone ligands. The molecular regions around which these surfaces are computed can be visualized using transparent surfaces. The short and extended interactions are shown in red and blue areas. Intense red spots on the dnorm Hirshfeld surface signify close-contact interactions, highlighting areas of strong hydrogen bonding [42]. The red and blue patches on the surface indicate π–π stacking interactions. Analysis of the shape index suggests that intramolecular and stacking interactions play a significant role in stabilizing the crystal packing [43]. The concept of curvedness is related to the root mean square (RMS) curvature of a surface. This means that surfaces with flat regions exhibit low curvedness, while surfaces with sharp features show high curvedness [19]. Plotting the HS over the curvedness π···π and shape index allows for the observation of stacking interactions, which enhance the stability of the crystal [44]. The fragment patches provide the proper methodology for determining the closest nearby molecular coordination framework. The absence of red spots suggests that the compound lacks significant long-range hydrogen bonds. The concave regions of the yellow-orange triangles on the shape index correspond to the atoms involved in π···π stacking interactions within the molecule [42]. With the help of 2D fingerprint plots,

non-covalent interactions contributing to the stabilization of crystal packing may be quantitatively investigated. The packing efficiency of the compound can be evaluated by calculating the interaction percentages between both all atoms and specific atom types using percentage statistics. Cu-All atoms interaction is 1% in both complexes **7** and **8**. While 1% and 0.9% interaction exists between all-Cu atoms in complex-**7** and complex-**8,** respectively. **Fig.4b.21** displays the molecular Hirschfeld diagram for both complexes. Other interactions of atoms and 2D fingerprint plots of both complexes are shown in **Figs.4b.22-4b.23**.

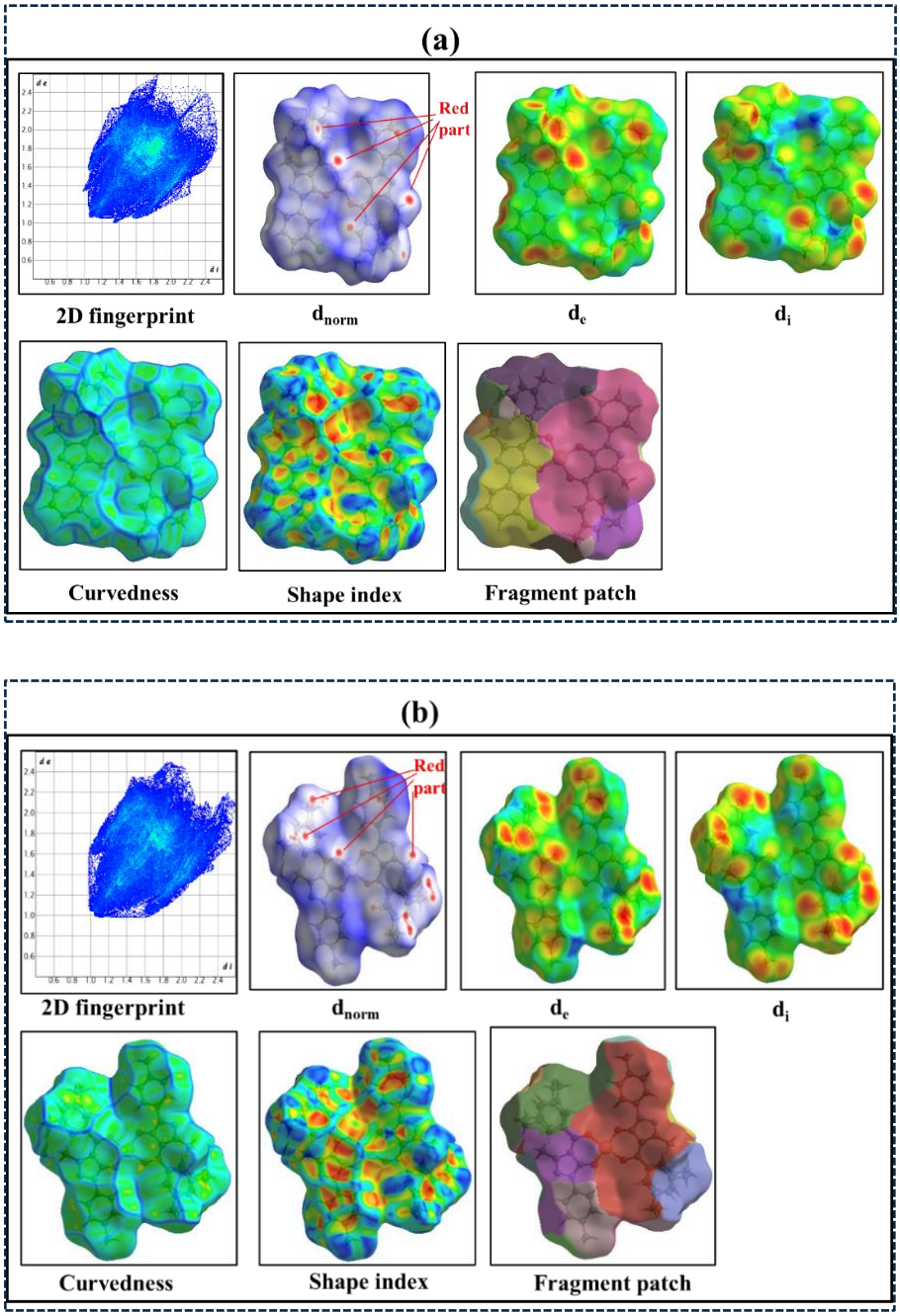

Fig.4b.21. The molecular Hirshfeld (fragment patch, dnorm, di, de, curvedness, shape index and FP plots) of (a) complex-7 and (b) complex-8

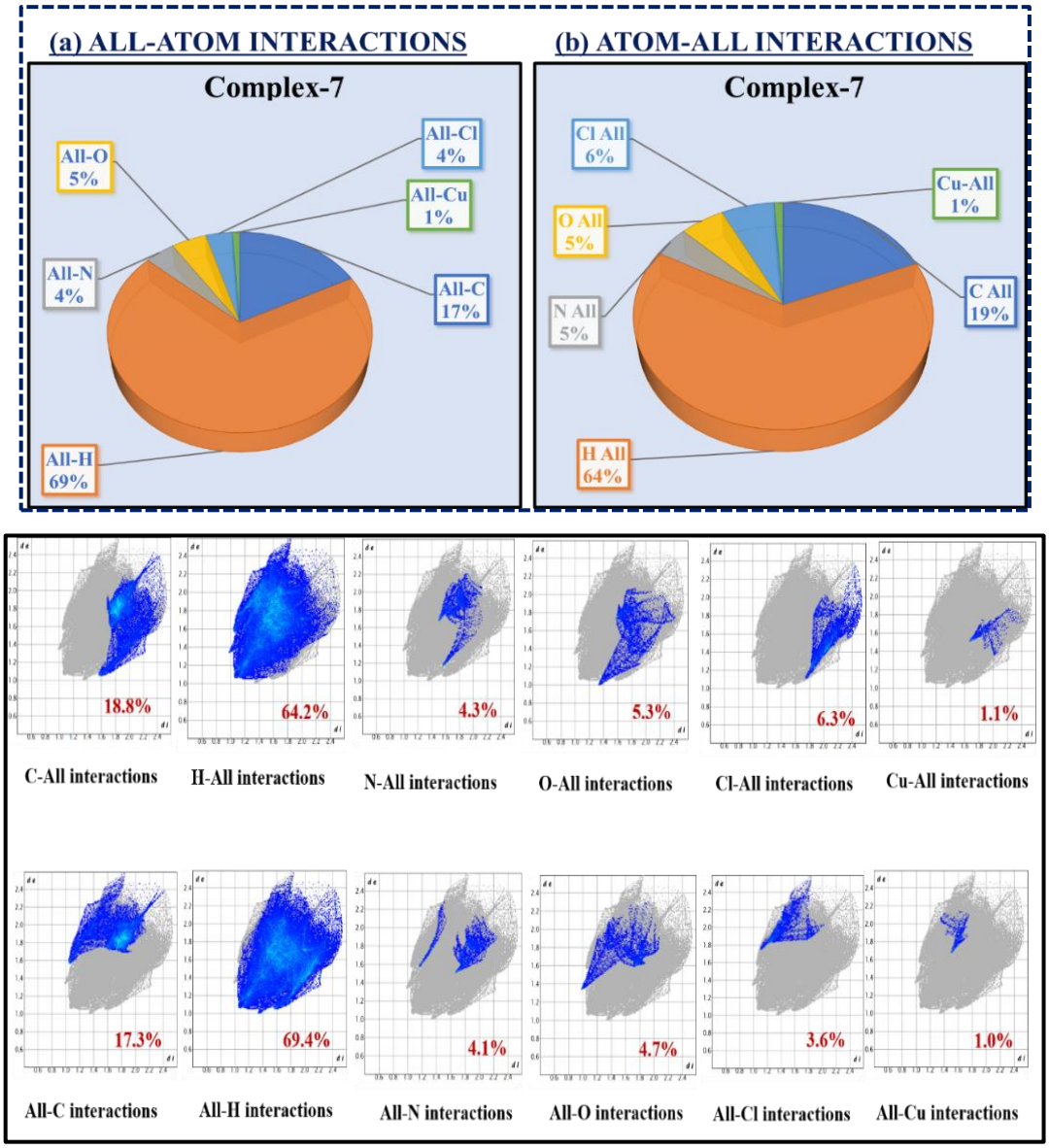

Fig.4b.22. Complex-7: Graphical presentation of percentage interactions between each inside and outside atoms and 2D fingerprint plots

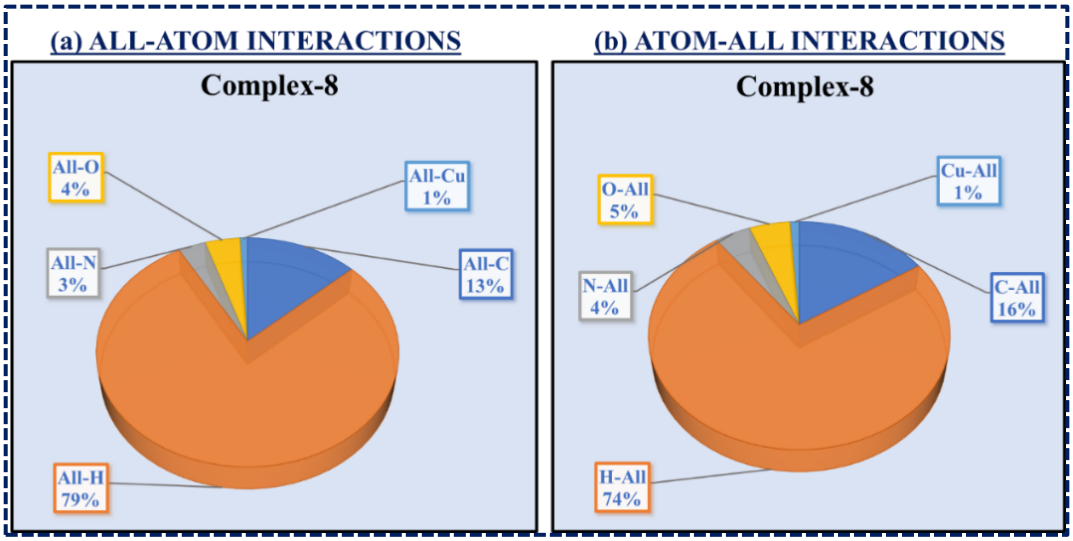

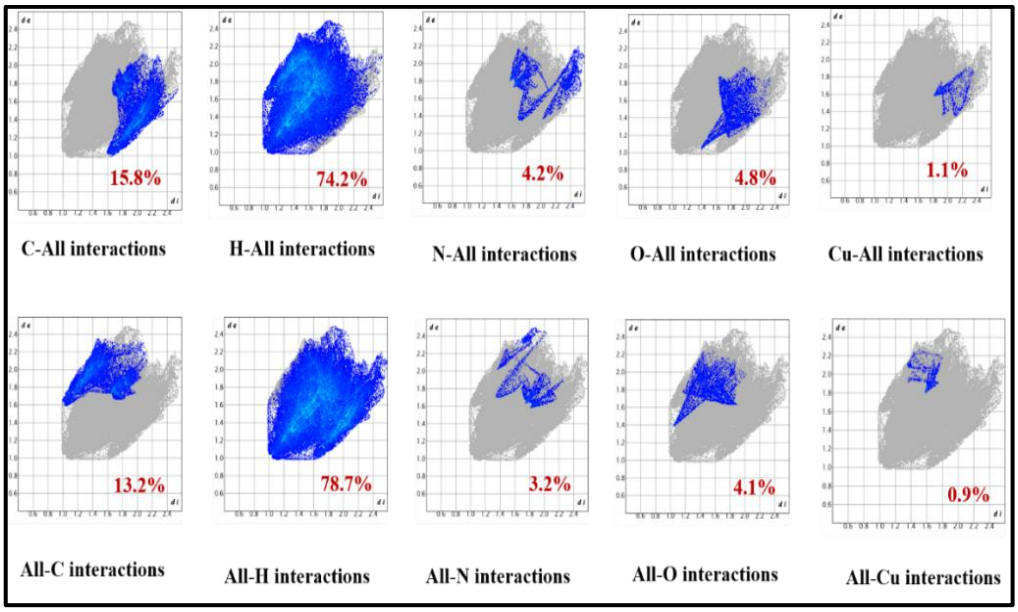

Fig.4b.23. Complex-8: Graphical presentation of percentage interactions between each inside and outside atoms and 2D fingerprint plots

we calculated the voids within the crystal structure by assuming spherically symmetric atoms and summing the electron densities of all atoms in the structure. The results indicate that the percentage of space occupied by voids is **9.00%** in complex-**7** and **8.92%** in complex-**8**, indicating a packing efficiency of **91.0%** in both crystals. This high packing efficiency suggests that the molecules in these compounds are tightly packed with minimal cavities. suggesting that the molecules in these compounds are tightly packed with minimal cavities [36][37]. The graphical representation of voids in the crystal packing of both complexes is in **Fig.4b.24.**

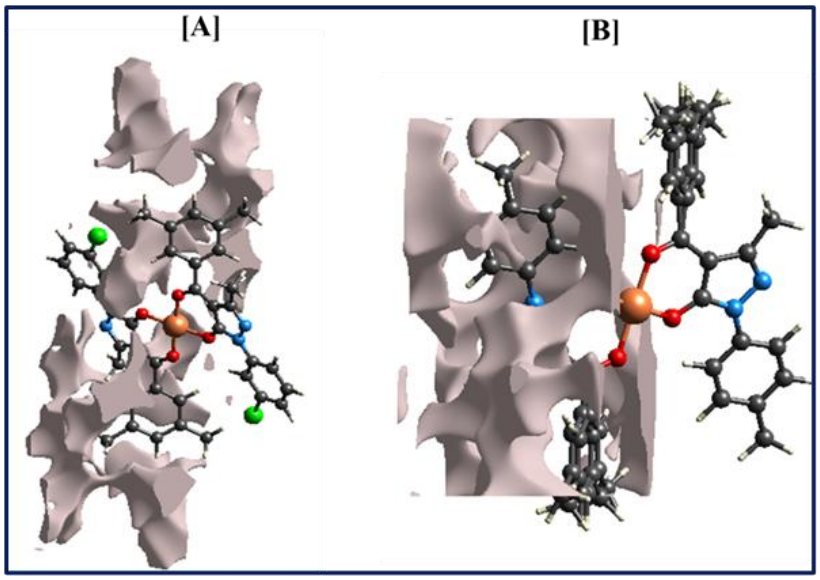

Fig.4b.24. Graphical representation of voids in the crystal packing of [A] complex-7 & [B] complex-8

4b.3.7 ESR analysis (Magnetic behaviour)

ESR analysis was performed at the JEOL ESR apparatus in solution state at 77K (LNT) using the X band to clarify the magnetic behaviour of the copper complexes. Tetracyanoethylene (TCNE) was used as a marker (g = 2.00277). Four hyperfine line splitting patterns in the graph suggest that Cu(II) is present in the complex. The value of $g_{\|}$ at LNT is 2.3562, and $g_{\perp}$ is 2.0690. The value of the g tensor is $g_{\|} > g_{\perp} > 2.0023$, which supports the square planner geometry. An average value calculated through $|g|^{a} = 1/3 (g_{\|}+2g_{\perp})$ and $|A|^{a} = 1/3 (A_{\|}+2A_{\perp})$ [38]. A geometric parameter G value is found to be 5.1623 by this formula: $G = (g_{\|} - 2.0023)/(g_{\perp} - 2.0023)$. The geometric parameter G falls between 6.49 and 12.02, demonstrating that the exchange interaction between the Cu(II) centre is absent in the complex [39][40][41]**.** The covalent nature is suggested by the computed value $\alpha^2 = 0.85$. Since both the synthesized complexes have the same square planar geometry, having copper in a +2 state, the result also supports the existence of complex-**8**. **Table 4b.15** represents the different parameters from the ESR spectral analysis of **complex-8.** The ESR spectrum of complex-**8** at LNT is shown in **Fig.4b.25.**

$$\alpha^2 = A_{II}/0.036 + (g_{II} - 2.0023) + 3/7\,(g_{\perp} - 2.0023) + 0.04 \qquad (2)$$

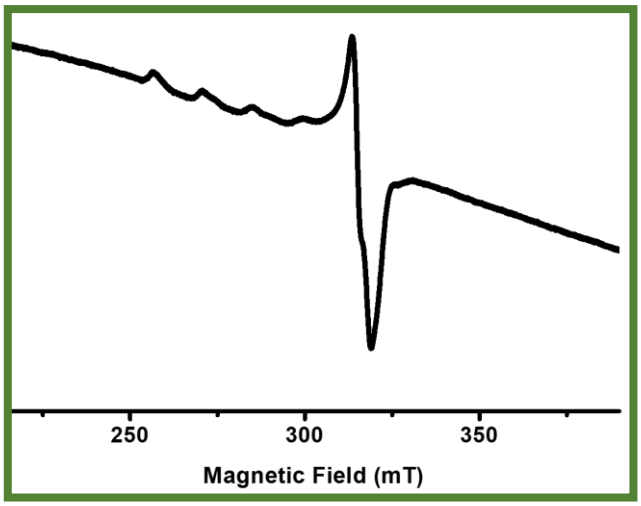

Fig.4b.25. The solution state X-band ESR spectra of complex-8 at LNT

Table 4b.15. Different parameters from ESR spectral analysis of complex-8

Parameters	LNT
$g_{\|}$	2.3562
$g_{\perp}$	2.0690
$\|g\|^{a}$	2.1647
$A_{\|}$ (10^{-4} cm^{-1})	154.0
$A_{\perp}$ (10^{-4} cm^{-1})	48.2
$\|A\|^{a}$ (10^{-4} cm^{-1})	83.5
G	5.1623

4b.3.8 Cytotoxicity assay

Cell viability was assessed using the MTT assay. As mentioned in **section 4b.3.6.1**, the HOMO-LUMO energy gap for complex-**8** is lower than that of complex-**7**. Consequently, the cytotoxicity of complex-**8** was evaluated. Three different cancer cell lines—NCI-H23 (lung cancer), HepG2 (liver cancer), and SH-SY5Y (neuroblastoma) were used to assess the antiproliferative activity of complex-**8.** The IC_{50} values of complex-**8** against these cell lines are summarized in **Table 4b.16.** According to the analysis, complex-**8** showed the best result against SH-SY5Y neuroblastoma cells, with a lower IC_{50} value (3.9 µM). Due to its higher effectiveness, the complex was further studied and compared with cisplatin, a well-known drug frequently used to treat a range of cancers [49]. When cisplatin was administered to the SH-SY5Y cell line, the IC_{50} value of 44.9 µM was recorded, which is significantly higher than the IC_{50} value of complex-**8**. These findings suggest that the synthesized copper complex is more effective than cisplatin, exhibiting notable cytotoxic activity. This analysis supports the conclusion that lower HOMO-LUMO energy gaps indicate higher chemical reactivity and biological activity [50]. The percentage of cell viability for NCI-H23 and HepG2 cells exposed to different doses of complex-**8** is shown in **Fig.4b.26.** A comparison of the percentage of cell viability for SH-SY5Y cells exposed to complex-**8** and cisplatin is illustrated in **Fig.4b.27.**

Table 4b.16. IC_{50} values of complex-8 and cisplatin against three cancer cell lines.

Percent inhibition (IC_{50} values)		
Compounds	**Cisplatin**	**$[Cu(HL^{VIII})_2]$**
SH-SY5Y	44.9 µM	3.9 µM
NCI-H23	-	4.6 µM
HepG2	-	5.8 µM

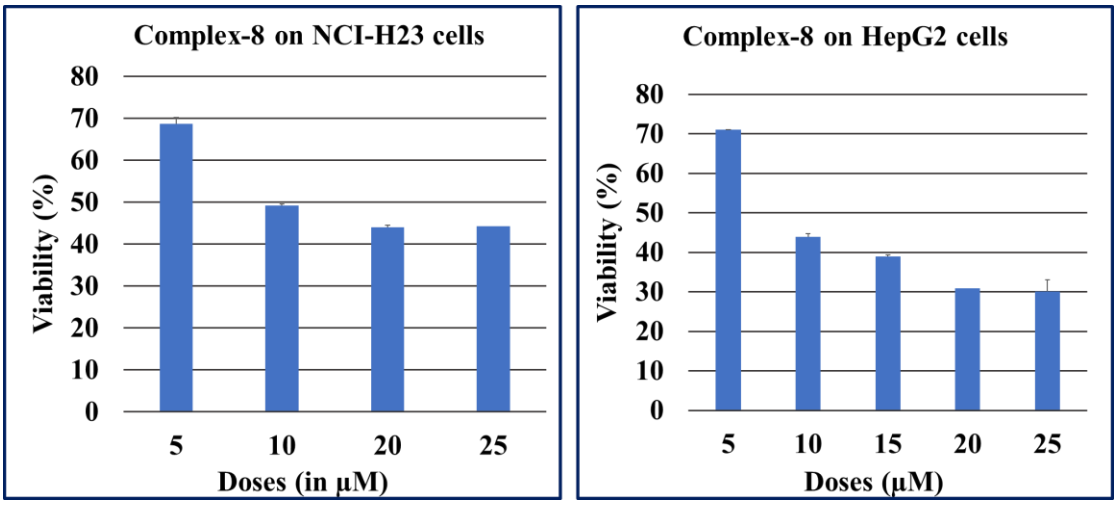

Fig.4b.26. Percent cell viability of NCI-H23 and SH-SY5Y cells exposed to indicated doses of complex-8

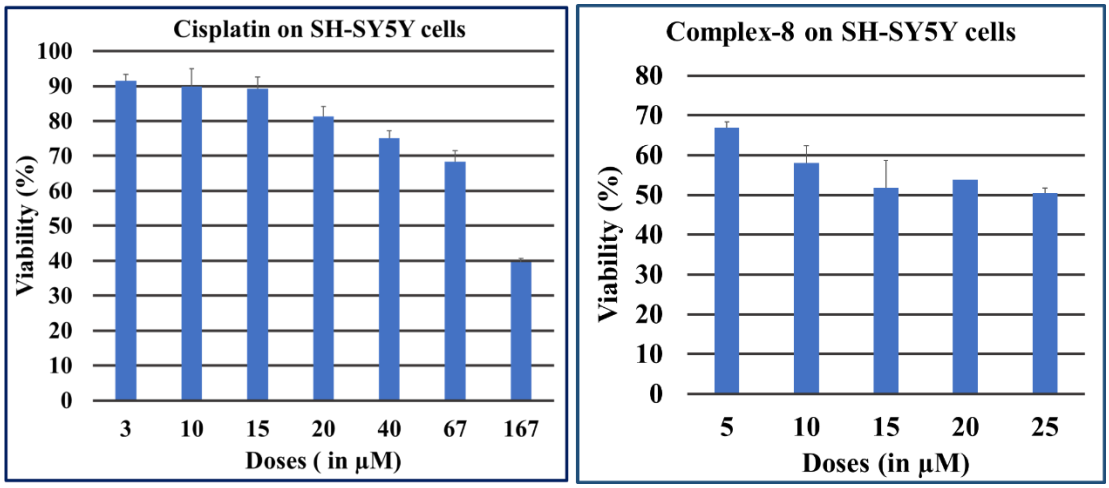

Fig.4b.27. A comparison of % cell viability of SH-SY5Y cells exposed to an indicated dose of complex-8 and cisplatin

4b.4 conclusion

The present study highlights the pharmacological potential of acylpyrazolone-based Cu(II) complexes, showcasing their promising synthesis and design. We successfully synthesized two new Cu(II) complexes using acylpyrazolone ligands, characterizing them with various analytical and spectroscopic techniques. A single crystal X-ray diffraction study confirmed a square planar geometry around the copper centre in both complexes. In each case, the copper ion is bis-chelated by two pyrazolone molecules via carbonyl and benzoyl carbonyl oxygen donors. Magnetic property was investigated using X-band ESR measurements at liquid nitrogen temperature (LNT). Additionally, Hirshfeld surface analysis identified key intermolecular interactions. The geometry of both complexes was optimized using density functional theory (DFT) with the B3LYP/LANL2DZ basis set, providing

insight into their frontier molecular orbitals in the gas phase. Spin density analysis further clarified the total electron distribution. Notably, the HOMO-LUMO energy gap revealed that complex-**8** is highly effective, with a small gap of 3.795 eV, facilitating electron transport and enhancing charge transfer interactions. Given these properties, complex-**8** was selected for biological evaluation against three cancer cell lines: NCI-H23, HepG2 and SH-SY5Y. Its lower IC_{50} value, particularly against SH-SY5Y cells, prompted further comparisons with cisplatin, a well-known chemotherapeutic agent. The copper complex inhibited cell viability, suggesting its potential as an anticancer agent. Future research should explore its efficacy through ***in vivo*** studies.

References

[1] E.C. Constable, Evolution and understanding of the d-block elements in the periodic table, Dalt. Trans. 48 (2019) 9408–9421. https://doi.org/10.1039/c9dt00765b.

[2] S.K. Mustafa, M.A. AlSharif, Copper (Cu) an Essential Redox-Active Transition Metal in Living System—A Review Article, Am. J. Anal. Chem. 09 (2018) 15–26. https://doi.org/10.4236/ajac.2018.91002.

[3] S. Ravichandran, R. M. Madhumitha Sri, M. Mehraj, C. Sowmya, The importance of transition metals as drug, Int. J. Clin. Biochem. Res. 9 (2022) 1–3. https://doi.org/10.18231/j.ijcbr.2022.001.

[4] H. Inac, M. Ashfaq, N. Dege, M. Feizi-Dehnayebi, K.S. Munawar, N.K. Yağcı, E. POYRAZ Çınar, M.N. Tahir, Synthesis, spectroscopic characterizations, single crystal XRD, supramolecular assembly inspection via hirshfeld surface analysis, and DFT study of a hydroxy functionalized schiff base Cu(II) complex, J. Mol. Struct. 1295 (2024) 136751. https://doi.org/10.1016/j.molstruc.2023.136751.

[5] J.K. Nath, Synthesis, supramolecular insight, Hirshfeld surface analyses and optical properties of Fe(II) and Cu(II) complexes of flexible imidazole tethered 1,8-naphthalimide, Transit. Met. Chem. (2024). https://doi.org/10.1007/s11243-024-00572-z.

[6] I.P. Ejidik, Cu(II) Complexes of 4-[(1E)-N-{2-[(Z)-Benzylidene-amino]ethyl} ethanimidoyl]benzene-1,3-diol Schiff Base: Synthesis, Spectroscopic, In-Vitro Antioxidant, Antifungal and Antibacterial Studies (2018) 1–18. https://doi.org/10.3390/molecules23071581.

[7] M.H. Abdellattif, E.O. Hamed, N.K.R. Elhoseni, M.G. Assy, A.H.M. Emwas, M. Jaremko, I. Celik, A. Titi, K. Kumar Yadav, M.S. Elgendy, W.S. Shehab, Synthesis of novel pyrazolone candidates with studying some biological activities and in-silico studies, Sci. Rep. 13 (2023) 1–25. https://doi.org/10.1038/s41598-023-43575-z.

[8] J.M.M. and R.C.M. PRADEEP KUMAR VISHWAKARMA, Pyrone-based Cu (II) complexes, their characterization, DFT based conformational drift from square planar to square pyramidal geometry, 128 (2016) 511–522. https://doi.org/10.1007/s12039-016-1048-6.

[9] Z. Zhao, X. Dai, C. Li, X. Wang, J. Tian, Y. Feng, J. Xie, Pyrazolone structural motif in medicinal chemistry: Retrospect and prospect, Eur. J. Med. Chem. 186 (2020)

111893. https://doi.org/10.1016/j.ejmech.2019.111893.

[10] K. Karrouchi, S. Radi, Y.R. Id, J. Taoufik, Synthesis and Pharmacological Activities of Pyrazole Derivatives : A Review, n.d. https://doi.org/10.3390/molecules23010134.

[11] S. Barad, K. Chaudhari, R.N. Jadeja, H. Roy, D. Choquesillo-Lazarte, Square pyramidal Cu(II) acylpyrazolone complex: Synthesis, characterization, crystal structure, DFT and Hirshfeld analysis, in-vitro anti-cancer evaluation, J. Mol. Struct. 1294 (2023) 136345. https://doi.org/10.1016/j.molstruc.2023.136345.

[12] F. Marchetti, R. Pettinari, C. Di Nicola, C. Pettinari, J. Palmucci, R. Scopelliti, T. Riedel, B. Therrien, A. Galindo, P.J. Dyson, Synthesis, characterization and cytotoxicity of arene-ruthenium(II) complexes with acylpyrazolones functionalized with aromatic groups in the acyl moiety, Dalt. Trans. 47 (2018) 868–878. https://doi.org/10.1039/c7dt04249c.

[13] C. Molinaro, A. Martoriati, L. Pelinski, K. Cailliau, Copper Complexes as Anticancer Agents Targeting Topoisomerases I and II, Cancers. 12, (2020) 2863. https://doi.org/10.3390/cancers12102863.

[14] S.A. Shaikh, S.S. Bhat, P.L. Hegde, V.K. Revankar, A. Kate, D. Kirtani, A.A. Kumbhar, V. Kumbar, K. Bhat, Synthesis, structural characterization, protein binding, DNA cleavage and anticancer activity of fluorophore labelled copper(ii) complexes based on 1,8-naphthalimide conjugates, New J. Chem. 45 (2021) 16319–16332. https://doi.org/10.1039/d1nj02696h.

[15] S. Hamamci Alisir, N. Dege, R. Tapramaz, Synthesis, crystal structures and characterizations of three new copper(II) complexes including anti-inflammatory diclofenac, Acta Crystallogr. Sect. C Struct. Chem. 75 (2019) 388–397. https://doi.org/10.1107/S2053229619001827.

[16] M.A. Raza, U. Farwa, M. Danish, S. Ozturk, A.A. Aagar, N. Dege, S.U. Rehman, A.G. Al-Sehemi, Computational modelling of imines based anti-oxidant and anti-esterases compounds: Synthesis, single crystal and In-vitro assessment, Comput. Biol. Chem. 104 (2023) 107880. https://doi.org/10.1016/j.compbiolchem.2023.107880.

[17] N. Meundaeng, T.J. Prior, A. Rujiwatra, Crystal structures and Hirshfeld surface analysis of transition-metal complexes of 1,3-azolecarboxylic acids, Acta Crystallogr. Sect. C Struct. Chem. 75 (2019) 1319–1326. https://doi.org/10.1107/S2053229619011525.

[18] M. Travadi, R.N. Jadeja, R.J. Butcher, M.S. Shekhawat, Neodymium based acylpyrazolone complexes: Synthesis and physicochemical characterizations, Inorganica Chim. Acta. 559 (2024) 121766. https://doi.org/10.1016/j.ica.2023.121766.

[19] M. Travadi, R.N. Jadeja, R.J. Butcher, Uranyl (VI) Mixed-ligand complex synthesis and characterization using 4-acylhydrazone-5-pyrazolone and 4-acylpyrazolone : Covalency , crystal assay , DFT study and Hirshfeld analysis,J. Mol. Struct.1281 (2023)135137. https://doi.org/10.1016/j.molstruc.2023.135137.

[20] G.M. Sheldrick, SHELXT - Integrated space-group and crystal-structure determination, Acta Crystallogr. Sect. A Found. Crystallogr. 71 (2015) 3–8. https://doi.org/10.1107/S2053273314026370.

[21] G.M. Sheldrick, Crystal structure refinement with SHELXL, Acta Crystallogr. Sect. C Struct. Chem. 71 (2015) 3–8. https://doi.org/10.1107/S2053229614024218.

[22] C.F. Macrae, P.R. Edgington, P. McCabe, E. Pidcock, G.P. Shields, R. Taylor, M. Towler, J. Van De Streek, Mercury: Visualization and analysis of crystal structures, J. Appl. Crystallogr. 39 (2006) 453–457. https://doi.org/10.1107/S002188980600731X.

[23] P.J. Hay, W.R. Wadt, Ab initio effective core potentials for molecular calculations. Potentials for the transition metal atoms Sc to Hg, J. Chem. Phys. 82 (1985) 270–283. https://doi.org/10.1063/1.448799.

[24] L. Chen, T. Liu, J.-Z. Chen, A density functional theory study on the electronic structures and properties of methylenediaminetetraacetate complexes (M=Co, Ni, Cu, Zn, Cd), Acta Chim. Sin. 66 (2008) 1187–1195.

[25] S. Lehtola, I observed researchers are using different basis set to optimize and calculate HOMO-LUMO of organometallics. Which one is appropiate?, (2018).

[26] A.K. Patel, R.N. Jadeja, H. Roy, R.N. Patel, S.K. Patel, R.J. Butcher, Pseudo-tetrahedral copper(II) complex derived from N'-[(2E,3Z)-4-hydroxy-4-phenylbut-3-en-2-ylidene]acetohydrazide: Synthesis, molecular structure, quantum chemical investigations, antioxidant and antiproliferative properties, J. Mol. Struct. 1185 (2019) 341–350. https://doi.org/10.1016/j.molstruc.2019.03.004.

[27] L. Tong, L.-L. Gan, H.-W. Zhang, Y.-X. Sun, H.-Y. Niu, W.-K. Dong, Synthesis,

structure, theoretical studies, and properties of dinuclear Cu(II) and novel trinuclear Co(II) complexes with a more flexible 3-MeOsalamo-like ligand, J. Mol. Struct. 1294 (2023) 136465. https://doi.org/10.1016/j.molstruc.2023.136465.

[28] V. Baliram T, P. Sanjay K, P. Arvind M, Synthesis, Spectral Characterization and Antitubercular Study of Novel Quinoline Schiff Base and Its Metal Complexes, Anal. Chem. Lett. 11 (2021) 523–538. https://doi.org/10.1080/22297928.2021.1921616.

[29] Y.P. Singh, R.N. Patel, Y. Singh, Crystal structure, configurational and DFT study of nickel(II) complexes with N2O-donor type Schiff base ligand, Indian J. Chem. - Sect. A Inorganic, Phys. Theor. Anal. Chem. 57A (2018) 44–51.

[30] H. Ezzat, A.A. Menazea, W. Omara, O.H. Basyouni, S.A. Helmy, A.A. Mohamed, W. Tawfik, M. Ibrahim, Dft: B3lyp/ lanl2dz study for the removal of fe, ni, cu, as, cd and pb with chitosan, Biointerface Res. Appl. Chem. 10 (2020) 7002–7010. https://doi.org/10.33263/BRIAC106.70027010.

[31] V. Krishnakumar, V. Balachandran, T. Chithambarathanu, Density functional theory study of the FT-IR spectra of phthalimide and N-bromophthalimide, Spectrochim. Acta Part A Mol. Biomol. Spectrosc. 62 (2005) 918–925. /https://doi.org/10.1016/j.saa.2005.02.051.

[32] D. Karaka, K. Sayin, DFT and TD-DFT studies on copper (II) complexes with tripodal tetramine ligands, 52 (2013) 480–485.

[33] O. V Gritsenko, Koopmans’ theorem and its density-functional-theory analog assessed in evaluation of the red shift of vertical ionization potential upon complexation, Chem. Phys. Lett. (2017). https://doi.org/10.1016/j.cplett.2017.11.019.

[34] M. Savarese, É. Brémond, I. Ciofini, C. Adamo, Electron Spin Densities and Density Functional Approximations: Open-Shell Polycyclic Aromatic Hydrocarbons as Case Study, J. Chem. Theory Comput. 16 (2020) 3567–3577. https://doi.org/10.1021/acs.jctc.0c00059.

[35] D. Suresh, M. Amalanathan, S. Sebastian, D. sajan, I.Joe, V. Nemec, Vibrational spectral investigation and natural bond orbital analysis of pharmaceutical compound 7-Amino-2,4-dimethylquinolinium formate – DFT approach. Spectrochim Acta A Mol Biomol Spectrosc. 115(2013)595-602. https://doi.org/10.1016/j.saa.2013.06.077.

[36] M.N. Tahir, M. Ashfaq, M. Feizi-Dehnayebi, K.S. Munawar, Ş. Atalay, N. Dege, N. Guliyeva, A. Sultan, Crystal structure, Hirshfeld surface analysis, computational study and molecular docking simulation of 4-aminoantipyrine derivative, J. Mol. Struct. 1320 (2025) 139747. https://doi.org/https://doi.org/10.1016/j.molstruc.2024.139747.

[37] S.S. Hasanova, E.A. Yolchueva, A.Q. Mashadi, S. Muhammad, M. Ashfaq, M.E. Muhammed, K.S. Munawar, M.N. Tahir, A.G. Al-sehemi, S.S. Alarfaji, Synthesis , Characterization , Crystal Structures , and Supramolecular Assembly of Copper Complexes Derived from Nitroterephthalic Acid along with Hirshfeld Surface Analysis and Quantum Chemical Studies, (2023). https://doi.org/10.1021/acsomega.2c07686.

[36] M. Valko, P. Pelikan, S. Biskupic, M. Mazur, ESR spectra of copper(II) complexes in the solids, Chem. Pap. 44 (1990) 805–813. https://www.chemicalpapers.com/file_access.php?file=446a805.pdf.

[37] B.J. Hathaway, D.E. Billing, The electronic properties and stereochemistry of mono-nuclear complexes of the copper(II) ion, Coord. Chem. Rev. 5 (1970) 143–207. https://doi.org/10.1016/S0010-8545(00)80135-6.

[38] S.M. Emam, S.A. Abouel-Enein, F.A. El-Saied, S.Y. Alshater, Synthesis and characterization of some bi, tri and tetravalent transition metal complexes of N′-(furan-2-yl-methylene)-2-(p-tolylamino) acetohydrazide HL 1 and N′-(thiophen-2-yl-methylene)-2-(p- tolylamino)acetohydrazide HL 2, Spectrochim. Acta - Part A Mol. Biomol. Spectrosc. 92 (2012) 96–104. https://doi.org/10.1016/j.saa.2012.02.045.

[39] Y.K. Abdel-Monem, S.M. Emam, H.M.Y. Okda, Solid state thermal decomposition synthesis of CuO nanoparticles from coordinated pyrazolopyridine as novel precursors, J. Mater. Sci. Mater. Electron. 28 (2017) 2923–2934. https://doi.org/10.1007/s10854-016-5877-3.